DEVELOPMENT OF LEAD-FREE PIEZOELECTRIC THIN FILMS BY PULSED

LASER DEPOSITION

by

MARYAM ABAZARI TORGHABEH

A Dissertation submitted to the

Graduate School-New Brunswick

Rutgers, The State University of New Jersey

in partial fulfillment of the requirements

for the degree of

Doctor of Philosophy

Graduate Program in Materials Science and Engineering

written under the direction of

Prof. Ahmad Safari

and approved by

_____

_____

_____

_____

_____

New Brunswick, New Jersey

May, 2010

ABSTRACT OF THE DISSERTATION

Development of Lead-Free Piezoelectric Thin Films by Pulsed Laser Deposition

By MARYAM ABAZARI TORGHABEH

Dissertation Director:

Prof. Ahmad Safari

As a high performance piezoelectric material widely used in sensors, actuators and other electronic devices, lead zirconate titanate (PZT) ceramics have been the center of attention for many years. However, the toxicity of these materials and their exposure to the environment during processing steps, such as calcination, sintering, machining as well as problems in recycling and disposal have been major concerns regarding their usage all around the globe for the past couple of decades. Consequently, utilizing lead-based materials for many commercial applications have been recently restricted in Europe and Asia and measures are being taken in United States as well. Therefore, there is an urgent need for lead-free piezoelectrics whose properties are comparable to those of well-known PZT materials. Recently, the discovery of ultra-high piezoelectric activity in the ternary lead-free $KNaNbO_3$-$LiTaO_3$-$LiSbO_3$ (KNN-LT-LS) and $(Bi,Na)TiO_3$-$(Bi,K)TiO_3$-$BaTiO_3$ (BNT-BKT-BT) systems have given hope for alternatives to PZT. Furthermore, the demand for new generation of environment-friendly functional devices, utilizing piezoelectric materials, inspired a new surge in lead-free piezoelectric thin film research.

In this study, an attempt has been made to explore the development of lead-free piezoelectric thin films by Pulsed Laser Deposition (PLD) on $SrTiO_3$ substrate. While the

growth and development process of KNN-LT-LS thin films was the primary goal of this thesis, a preliminary effort was also made to fabricate and characterize BNT-BKT-BT thin films. In a comprehensive and systematic process optimization study in conjunction with X-ray diffractometry, the phase evolution, stoichiometry, and growth orientation of the films are monitored as a function of deposition conditions including temperature and ambient oxygen partial pressure. Processing parameters such as substrate temperature and pressure are shown to be highly dominant in determining the phase and composition of the films. Oxygen partial pressure has shown to control the chemical composition of the films through solid-gaseous phase equilibrium and substrate temperature has mostly influenced the growth mode and microstructure. Findings of this study has shown that 300-500 nm single-phase epitaxial KNN-LT-LS and BNT-BKT-BT thin films could indeed be obtained at a temperature of 700-750 ^{o}C and 300-400 mTorr of oxygen partial pressure. Following a series of studies on effect of doping, it was revealed that addition of 1 mol% Mn to KNN-LT-LS composition resulted in a significant suppression of leakage current and enhancement of polarization saturation. A remanent polarization of 16 $\mu C/cm^2$ and coercive field of 20 kV/cm were measured for such thin film, which are comparable to those of hard PZT counterparts. Also, a high remanent polarization and coercive field of 30 $\mu C/cm^2$ and 95 kV/cm were achieved in 350 nm BNT-BKT-BT thin films. Longitudinal (d_{33}) and transverse ($e_{31,f}$) piezoelectric coefficients of KNN-LT-LS thin films were found to be 55 pm/V and -4.5 C/m^2 respectively, prepared at the optimized conditions, whereas 350 nm BNT-BKT-BT thin films exhibited an $e_{31,f}$ of -2.25 C/m^2. The results of this study present the great potential of KNN-LT-LS and BNT-BKT-BT thin films for piezoelectric MEMS devices and provide a baseline for future investigations on lead-free piezoelectric thin films.

Acknowledgments

First, I want to thank God for giving me the strength and resolve to finish this task. I would like to thank my advisor, Prof. Safari, for his steady support, trust and confidence he gave me through the years I was working in his group. He gave me the freedom to pursue my curiosity and encouragement to carry on. I want to express my thanks to the members of my committee, Prof. Klein, Prof. Chhowalla, Prof. Cheong, and Prof. Khachaturyan for their help and guidance. Many thanks to Dr. Taekjib choi for all the useful discussion and his generous help in the lab for PFM measurements. Also, Prof. Trolier-McKinstry and Dr. Bharadwaja, who offered me their lab equipment as well as their time for piezoelectric measurements, are sincerely acknowledged. I have also learnt a lot of my knowledge from endless discussions with Dr. Koray Akdogan who was initially very much involved with the project. Also, I have to thank Prof. W. Mayo, who helped me on XRD work and Dr. Wielunski for his help in RBS measurements and data analysis.

Many months passed during my years at Rutgers, when I had no encouraging results. It has been very tough at times and hard to stay sane. I am very much obliged to all the people who helped me getting through and made it possible: present and previous members of our group, especially Piyalak "Note", Jingjing, Nader, Kian, David, and Bill and friends and colleagues from other groups, Goki, JD, Jen, and Sarika. I also have to thank John Yaniero, our laboratory manager, who was always there to help me with anything in the labs.

I also thank all of my Iranian friends in Rutgers and Princeton: Zahra, Sanaz, Roya, Farnaz, Noori, Vida, Nassim, Fatemeh and Arefeh. You guys made me feel at home.

Most importantly, I like to dedicate this thesis to my dear parents, Farideh and Mehdi and my brother, Alireza. I am always inspired by your faith and strength and will always be indebted to you.

And to Javad, my husband, best friend and soul-mate, for his true unconditional love, through my good and bad times. There are no words to convey how much I am grateful for having you by my side.

Table of Contents

List of Figures

List of Tables

1 Introduction and Background

1.1 Basic concepts of ferroelectricity

Ferroelectricity is defined as the ability of a material to retain a switchable spontaneous polarization, P_s, by an electric field and was discovered in 1921 in Rochelle salt. Also, ferroelectric crystals exhibit unique properties such as a spontaneous polarization below the Curie temperature, ferroelectric domains and Curie-Weiss type behavior of dielectric constant above Curie temperature. Since then, ferroelectricity has been discovered in several other structurally different categories of materials, the most common of which is the perovskite structure. The general formula for a perovskite is ABO_3, in which A is a large cation with valence of 1^+, 2^+ and 3^+ and B is a small cation with valences of 3^+, 4^+ and 5^+. The structure at higher temperatures, above the Curie point, is cubic and composed of an oxygen octahedron, occupying the faces of the unit cell with small B cation in the center and large A cations in the corner of the unit cell, as shown in Figure 1.1. The displacement of a B cation with respect to the oxygen octahedron and A-site cations causes a dipole moment in the unit cell with center of positive and negative charges taken apart from each other. **[1-9]**

All the existing crystal structures in the nature can be recognized based on their macroscopic symmetry elements and are categorized into thirty two so called *point groups*. The thirty-two point groups can be further classified into (a) 11 point groups having a center of symmetry, i.e. centrosymmetric and (b) 21 point groups, which do not possess a center of symmetry, non-centrosymmetric. A crystal having no center of symmetry possesses one or more crystallographically unique directional axes. All non-

centrosymmetric point groups, except the 432 point group, show piezoelectric effect along unique directional axes. Piezoelectricity is by definition the ability of a material to develop an electrical charge proportional to an applied mechanical stress. Piezoelectric materials also show a converse effect, where a geometric strain is produced upon the application of a voltage. The direct and converse piezoelectric effects can be expressed in tensor notation as,

$$P_i = d_{ijk}\sigma_{jk} \tag{1}$$

$$\varepsilon_{ij} = d_{kij}E_k \tag{2}$$

where P_i is the polarization generated along the i- axis in response to the applied stress σ_{jk}, and d_{ijk} is the piezoelectric coefficient. For the converse effect, ε_{ij} is the strain generated in a particular orientation of the crystal on the application of electric field E_i along the i-axis. Out of the twenty point groups which show the piezoelectric effect, ten point groups (including 1, 2, m, mm2, 4, 4mm, 3, 3m, 6, and 6mm) have only one unique direction axis. Such crystals are called pyroelectric (polar) crystals, including a large subgroup of "ferroelectrics" which show reversible spontaneous polarization. [8]
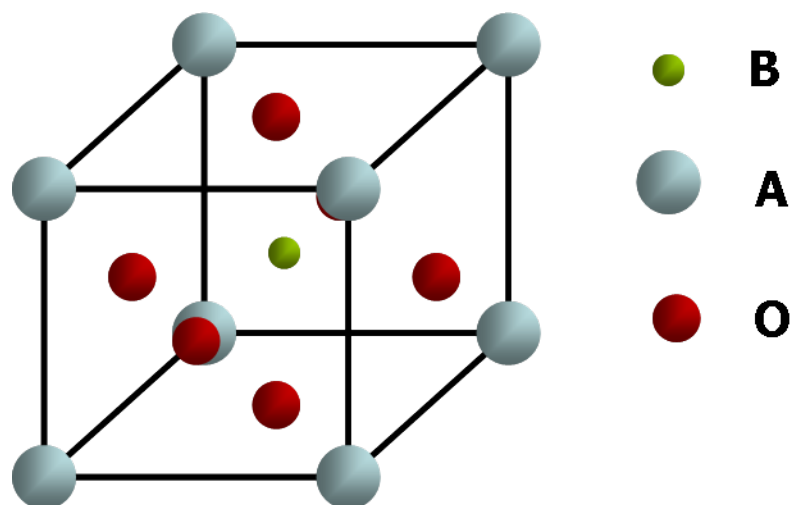
Figure 1.1 Structure of a perovskite ABO_3

Since the discovery of ferroelectricity in $BaTiO_3$ in 1950's, use of such ceramics has become widespread in capacitor applications and piezoelectric transducer devices. With the development of many other ferroelectric ceramics including lead titanate ($PbTiO_3$) and lead zirconate titanate (PZT) ceramics as well as new processing techniques and thin film fabrication technology, many new applications have emerged. The biggest use of ferroelectric ceramics have been in the areas such as ferroelectric ceramics for capacitor applications, ferroelectric thin films for non volatile memories, piezoelectric materials for medical ultrasound imaging and actuators, and electro-optic materials for data storage and displays. **[9]**

1.2 Characteristics of ferroelectric materials

As mentioned earlier, some of the most important unique characteristics of ferroelectric crystals are spontaneous polarization below Curie temoperature, polarization hysteresis and ferroelectric domains, which will be briefly discussed in the following.

1.2.1   Phase transitions

One of the main characteristics of most ferroelectric materials is the existence of a phase transition from a ferroelectric (polar) to a paraelectric (non-polar) phase, at a so called Curie point, T_0. Above this transition temperature, the dielectric constant of the ferroelectric material follows Curie-Weiss law:

$$K \cong \frac{C}{T - T_C} \qquad (3)$$

where K is dielectric constant, C is Curie constant, T is the temperature, and T_C the Curie-Weiss temperature. The dielectric constant shows a maximum at the transition temperature, and as explained earlier, above the transition temperature, the material is non-polar with zero spontaneous polarization and higher symmetry point group. In addition to the said transition, some of the most common ferroelectric materials, such as $BaTiO_3$ and $KNbO_3$ exhibit several other transitions below the Curie temperature. At each of these phase transition temperatures, the material undergoes a structural change with a peak in dielectric constant value at the transition point. The material however stays polar through all the transition below Curie temperature.**[7,10, 11]** This behavior of dielectric constant is depicted for $BaTiO_3$ in Figure 1.2.
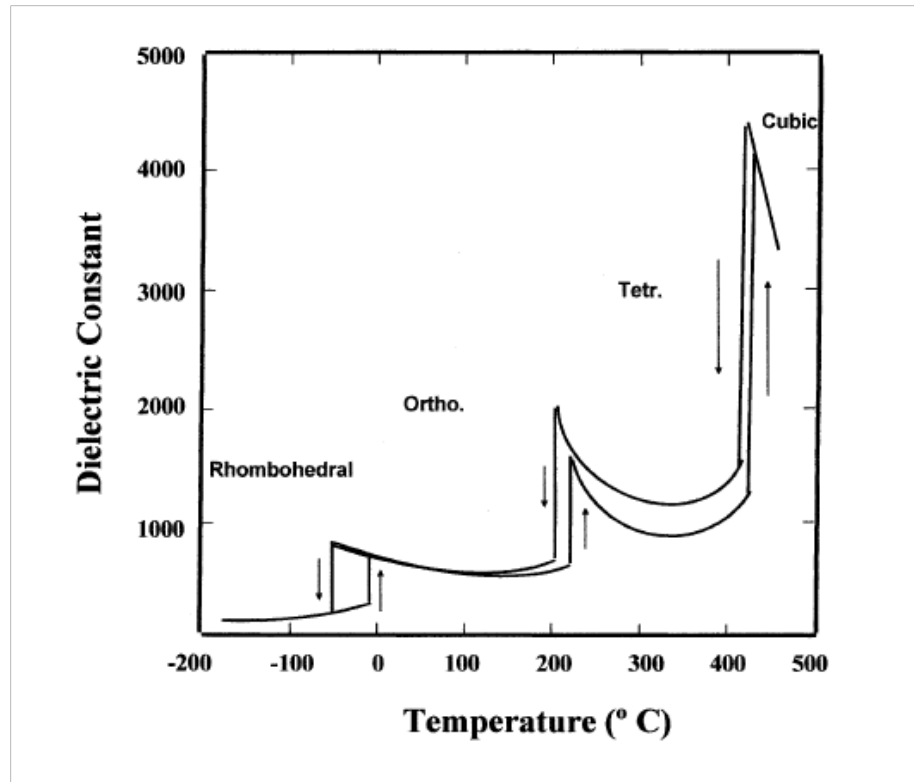
Figure 1.2 Dielectric constant as a function of temperature for $BaTiO_3$

The transition into a ferroelectric phase usually leads to strong anomalies in the dielectric, elastic, thermal and other properties of the material **[12]** and is accompanied with changes in the dimensions of the crystal unit cell. The associated strain is called the spontaneous strain, x_S. It represents the relative difference in the dimensions of the ferroelectric and paraelectric unit cells **[10,13]**.

1.2.2 Polarization hysteresis

One of the easiest ways to inspect ferroelectricity in a material is the observation of polarization hysteresis. Application of an electric field and cycling through negative and positive directions in a ferroelectric, results in a hysteretic behavior as shown

schematically in Figure 1.3. The polarization initially increases from zero to a *saturation polarization*, P_{sat} and upon decreasing the electric field, reduces to a *remanent polarization*, P_r. The electric field required to reduce the polarization back to a zero value, is called *coercive field*, E_C. **[10]**
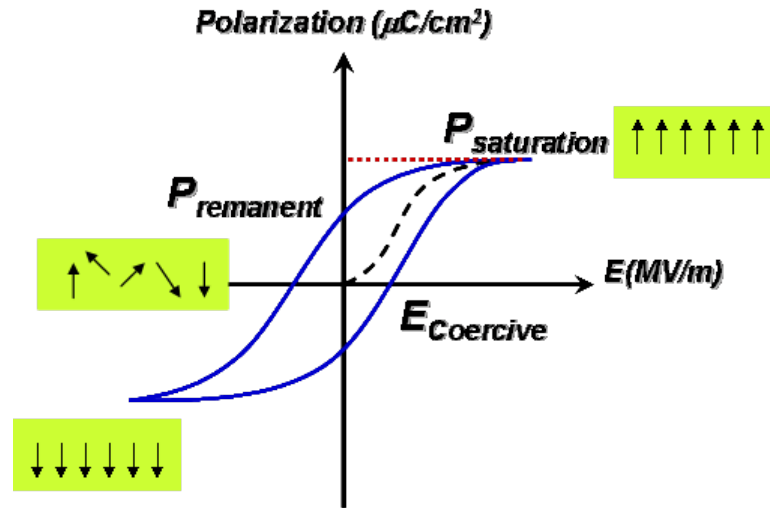
Figure 1.3 Polarization hysteresis in a ferroelectric material

1.2.3   Ferroelectric domains

A ferroelectric crystal often consists of regions called domains within each of which all dipole moments are aligned in the same direction, while this direction may differ from an adjacent domain. The individual dipoles, and as a result the spontaneous polarization are generated upon cooling the crystal below the Curie point. The region between two domains is called the domain wall. The walls between domains with oppositely orientated polarization are called 180° walls and those between regions with mutually perpendicular polarization are called 90° walls **[14]**. As the temperature is cooled down the Curie point, the generation of spontaneous polarization leads to formation of surface charge and this

surface charge in turn produces a so called *depolarizing field*, E_d, whose direction is the opposite of the spontaneous polarization. In principle, ferroelectric domains form to minimize the electrostatic energy of depolarizing fields and the elastic energy associated with mechanical strain generated in the ferroelectric material as it is cooled through paraelectric–ferroelectric phase transition **[15]**. The electrostatic energy generated as a result of depolarizing field may be minimized in two ways. The first is involved with the ferroelectric material into domains with oppositely oriented polarization and second with depolarizing charge being compensated for by electrical conduction through the crystal or by charges from the surrounding. On the other hand, 90° domain walls are considered responsible for minimizing the elastic energy. A combination of electric and elastic boundary conditions to which a crystal is subjected as it is cooled through the ferroelectric phase transition temperature usually leads to a complex domain structure with many 90° and 180° walls. This is schematically described in Figure 1.4.

creation of 90° walls
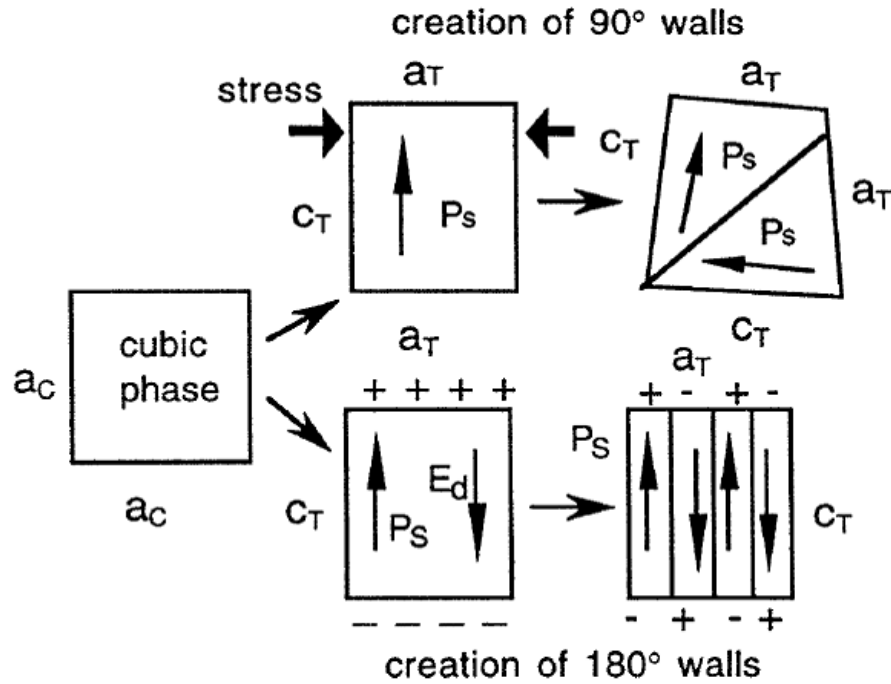
Figure 1.4 Creation of ferroelectric domains

1.3 Ferroelectric thin films

Since the goal of this study focuses on the ferroelectric thin films, in the following, it is attempted to briefly outline and review the most important issues associated with deposition, performance and applications of ferroelectric thin films.

1.3.1   Fabrication of ferroelectric thin films

Various techniques have been utilized for deposition of ferroelectric oxide thin films, including sol-gel, sputtering, chemical vapor deposition (CVD) and pulsed laser deposition (PLD).

Sol-gel processing consists of three steps, being namely, complexation, hydrolysis and polycondensation. First, a non-aqueous alkoxide precursor solution is prepared

according to desired stoichiometry, which is then hydrolyzed by solvent/water/acid solution. Next step is involved with deposition of a layer of *sol* on the substrate most commonly via spin coating. The film is then dried at relatively low temperatures to form a *gel*. Next rapid thermal annealing (RTA) is used as the post annealing treatment in order to crystallize the film and avoiding the reaction with silicon substrate. Some of the advantages of sol-gel technique are ease of processing, possibility of large-area production, control of thickness and ease of compositional control. Sol-gel is considered one of the most promising techniques in oxide ferroelectric thin film fabrication. However, there are drawbacks to this technique, which include microcrack formation and lower crystalline quality and possibility of epitaxial growth as compared to other techniques. **[16]**

In synthesis of thin film via sputtering, solid surface of a target material with desired stoichiometry is bombarded with energetic particles, which results in the ejection of surface atoms and deposition on a substrate, whose temperature is controllable. This technique provides high quality thin films due to a high vacuum required in the chamber prior to deposition which causes less contamination in the films. However, compared to other techniques, the deposition rate is relatively slow, being less than 1000Å/hour. This also leads to more interaction of the ferroelectric layer with the substrate which has to be avoided mostly from the device reliability viewpoint. **[17]**

Another technique for synthesis of oxide thin films is chemical vapor deposition (CVD), in which a compound is condensed from a gaseous phase onto a substrate. A chemical reaction or thermal decomposition is then responsible for the formation of the desired film composition on the substrate. Photonic excitation and glow discharge

sources can also be used to enhance the rate of deposition. CVD technique is popular for processing of compound semiconductors, due to its several advantages, including large-scale production, excellent compositional uniformity, and high deposition rates. One of the major challenges however is selection of the available, stable, non-toxic precursor materials. **[17]**

The technique of interest in this study is Pulsed Laser Deposition (PLD) which has been very popular in preparation of complex oxide thin films, in the past twenty years. Main advantages of PLD technique are simplicity of the process, especially with complex oxides containing a variety of elements, reproduction of target stoichiometry, high deposition rate, wide range of materials, possibility of multi-layer structures, and relatively inexpensive techniques as compared to other high quality growth techniques, such as CVD or molecular beam epitaxy (MBE). In this technique, surface of a target material with desired chemistry is ablated by laser irradiation inside a high vacuum chamber in a controlled gas atmosphere. As a result, a plasma plume is created that reacts with the background gas and is deposited on a heated substrate. The plasma plume is believed to contain atomic as well as ionic species from the target material. The main disadvantage of PLD is the small size of the film with uniform thickness and composition, which is typically around 1 cm^2. Also, the large particles, ranging from 1-5 μm in size, that are often ablated from the target surface may be present in the film. **[18-20]** Basic schematic of PLD system is shown in Figure 1.5.
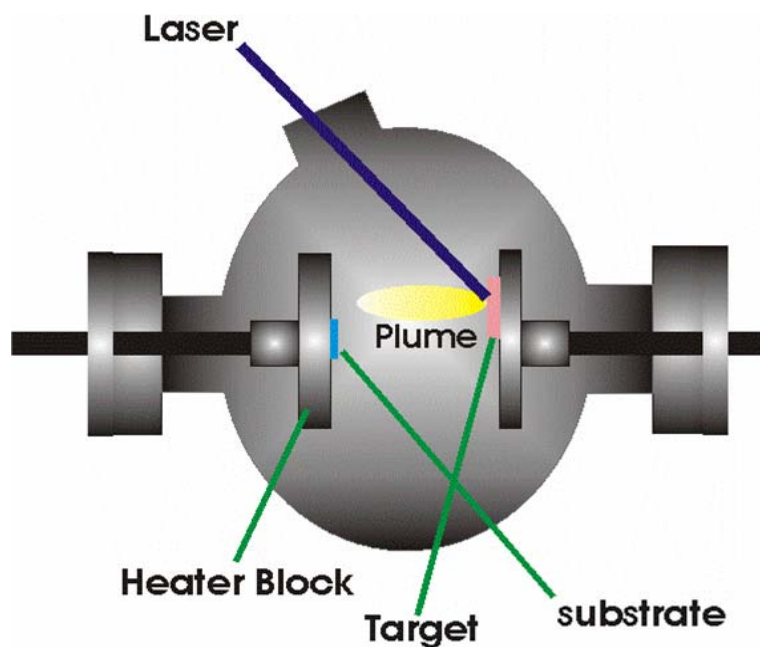
Figure 1.5 Schematic of a basic pulsed laser deposition system.

Several processing parameters are available in PLD technique and can be varied to achieve optimum quality in the thin films. The most important of these are substrate temperature, background gas pressure, laser fluence, e.g. energy and repetition rate and target-to-substrate distance. Also choice of substrate considerably influences the film growth and properties. In order to have a highly epitaxial film, it is essential to keep the lattice mismatch between the target material and the substrate of choice as small as possible.

Substrate temperature obviously affects the film microstructure through diffusivities of the atomic species of the target. Mobility and hence diffusion rate of the arriving atoms on the substrate increase with increasing the substrate temperature following an Arrhenius behavior. However, the evaporation rate of arriving atoms from the substrate is

also increased with temperature, which leads to a lower growth rate. Typical substrate temperature for deposition of oxide films ranges from 500-800°C.[21]

Oxygen is most commonly used as the background gas for the deposition of oxide thin films by PLD. The pressure is typically kept between 10 and 500mTorr. Several studies have revealed the effect of oxygen pressure on the chemical composition of the plasma plume and thus the film. This is explained through the solid-gas phase equilibrium and is especially important in case of oxide thin films. Also, higher oxygen pressures increases the number of collision events between plasma species and the oxygen molecules and thus results in a lower deposition rate. These collisions determine the shape and size of the plasma plume and therefore affect the area of uniform composition on the thin film. [22,23]

Another important processing parameter is the energy density of the laser, which is related to the laser spot size as well as the laser pulse energy. The energy of the laser pulse has to be above the threshold of ablation for all the elements in the target to avoid preferential ablation. Laser repetition rate on the other hand, increases the deposition rate and influences the quality and microstructure of the film. A higher repetition may lead a poor crystalline quality as a result of too much material arriving at the substrate before they can mobilize and rearrange on the surface.[24]

The target-to-substrate distance mainly impacts the microstructure and the deposition rate of the film. A larger target-to-substrate distance can also produce non-homogeneous plume as a result of differences in the velocities of the species. [25]

1.3.2   Electrical and electromechanical properties of ferroelectric thin films

Several factors greatly influence the behavior of ferroelectric thin films, such as mechanical clamping to the substrate, orientation of the film, the level of polarization and breakdown field strength. Therefore, this leads to very different properties of films with respect to bulk materials and this must be taken into account in design and realization of ferroelectric-containing devices.**[10]**

In general, ferroelectric thin films exhibit a lower dielectric constant and a higher dielectric loss, as compared to bulk ferroelectrics. This has been attributed mainly to the strain in thin films and a higher concentration of defects, such as oxygen vacancies. **[10]** The latter has been shown to be eliminated partially through annealing of the samples, while the former stays as the major degradation mechanism in dielectric properties of thin films. Also, relative permittivity in thin films has experimentally exhibited a linear dependence on the electric field amplitude, which may be attributed to the pinning of domain walls on randomly distributed defects. Additionally, it is observed that permittivity decreases logarithmically with the driving frequency. This also indicates that the extrinsic component of the dielectric permittivity is dominated by domain-wall pinning processes **[26]**.

One of the most significant differences between measured hysteresis loops of a bulk ferroelectric with that of a thin film is the value of the coercive field. In addition, the hysteresis loop of a thin film is usually more tilted as compared to that of bulk material. This is attributed to the difference in preparation of ceramics and thin films, thickness effects in ferroelectrics, the presence of charged defects as well as difference in polarization switching mechanism. Most of the present experimental results on

submicron ferroelectric thin films indicate a higher coercive field for thin films compared to bulk materials and a decrease of E_C with an increase in the film thickness. Several models have been proposed to explain this phenomenon including surface dielectric layer, surface pinning of the domain walls and depletion-assisted nucleation of domains of opposite polarity. [27] However, the latter two models are more consistent with the experimental observations. The first model predicts a rough estimate for E_c as 1/t which is in agreement within an order of magnitude with experiments. The second one, on the other hand, gives a more accurate prediction which is involved with the formation of a built-in electric field, as a result of Schottky barrier at the interface of a ferroelectric with metal electrode. In that case, E_c becomes $E_{cn} - eNt/2\varepsilon$, with E_{cn} being field necessary for the nucleation of oppositely oriented domains at the electrode, e the charge of electron, N the concentration of free carriers, t the thickness of ferroelectric film and ε its dielectric constant.

In addition to difference in coercive field, polarization hysteresis loops of a thin film exhibit a tilted behavior which can be explained by the presence of a dielectric layer on the top of the ferroelectric [28, 29]. This layer separates the bound charges that are due to the ferroelectric polarization from the compensating charges on the electrode. The tilt of the loops or the slope of the loop at E_C is proportional to the d/t ratio, with d being dielectric layer's thickness and t that of the ferroelectric layer. [28] Polarization hysteresis behavior of a typical ferroelectric thin film is sketched in Figure 1.6 for different film thicknesses.
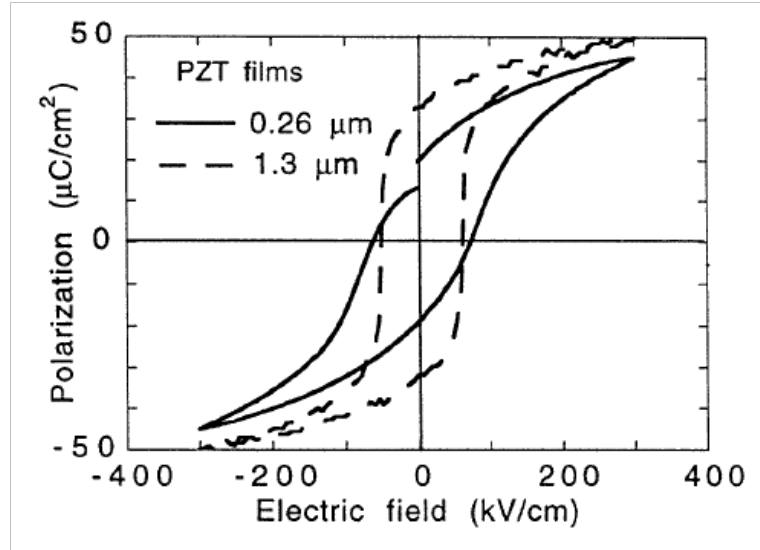
Figure 1.6 Polarization hysteresis behavior of PZT thin film showing tilt in the loop in smaller thicknesses

Piezoelectric properties of a ferroelectric thin film are also affected mainly by the clamping of the film to the substrate. The measured piezoelectric coefficient in films is always smaller relative to unclamped bulk ceramics, which can be at least partly explained by the clamping effects of the substrate. This has been studied by Lefki et al in detail. **[30]**

The strain–field butterfly loops in ferroelectric thin films are often observed to be highly asymmetrical even when no asymmetry was observed in the polarization loops. The origin of the asymmetry in the strain loops is attributed to a presence of residual substrate–film interfacial stresses **[31,32]**.

1.3.3   Applications of ferroelectric thin films

Ferroelectric materials are now being used in a wide spectrum of applications. In thin film form, ferroelectrics are now being developed for several years in RF devices and in

nonvolatile memories, MicroElectroMechanical Systems (MEMS) as well as for various sensor and actuator applications and for tunable microwave circuits. During the late 1990s, portable telephones became a mass product and the introduction of ferroelectric thin films recently contributed to their further miniaturization and improved performance. In this section, two of the most important applications of ferroelectric thin films are reviewed.

1.3.3.1 NV-RAM

One of the main applications of ferroelectric thin films is non-volatile memories or NV-RAM (Non-Volatile Random Access Memory). $Pb(Zr,Ti)O_3$-based FRAMs (Ferroelectric Random Access Memory) have now found their position in the markets and appear to be more and more established in low-power/low-voltage nonvolatile memories. The principle of nonvolatile FRAMs is based on the polarization reversal by an external applied electric field of metal-ferroelectric-metal capacitors. The computational "0" and "1" are represented by the nonvolatile storage of the negative or positive remanent polarization state, respectively. The destructive readout operation is performed via the displacement current. With respect to the electronic properties, FRAMs show attractive features, for example, write and read cycle times in the sub-100 ns range and low power consumption, which are in most cases superior to the performance of other nonvolatile technologies. After the demonstration of ferroelectric memories integration with silicon CMOS (Complementary metal–oxide–semiconductor) FRAMs capacity has exceptionally grown while the size has been constantly reduced. Also, most important to all ferroelectric thin film applications including memories, is the finding a

ferroelectric material that showed little or no degradation of the switchable ferroelectric polarization while cycling through typical read and write operations. Of the alternative ferroelectric materials, the Bi-based compounds exhibited the most improved read/ write cycling endurance, but only $SrBi_2Ta_2O_9$ (SBT) has led to marketable FRAM products. The SBT-based products are currently limited to low memory capacity (less than 16 kb) smartcard applications, although test chips with capacity as high as 4 Mbytes have been demonstrated.[33]

1.3.3.2 Actuators and sensors (MEMS)

Ferroelectric materials and most frequently $Pb(Zr,Ti)O_3$-based ceramics, have been utilized in actuator and sensor applications for many years, due to their outstanding electromechanical properties. Piezoelectric sensor exploit the piezoelectricity of such materials in direct effect while for actuators, the converse effect is used. Some of the main advantages of using ferroelectric materials are their high dielectric constant, high speed and high frequency operations, high efficiency of energy conversion, and a rather linear behavior, to name a few. As a result, ferroelectrics are used for ultrasonic imaging in 1-50MHz, nondestructive testing at the same frequencies due to large efficiency of energy conversion, piezoelectric resonators in signal filtering in 0.1-10GHz because of their high quality factor, high-K dielectrics and also in microscale devices as thin films. However, in thin films, the performance of the materials may be lower in terms of generation of voltage and force and higher resonance frequency.

Use of ferroelectric PZT materials in piezoelectric MEMS applications has been widely studied and one of their main applications is inkjet printers. The published value

of piezoelectric coefficient, $e_{31,f}$ of thin films in the past couple of decades indicates the progress of ferroelectric thin films for MEMS applications, with $D_3 = e_{31,f} (S_1 + S_2)$ where D_3 is the displacement field (charge Q_3 per electrode area), and S_1 and S_2 are the in-plane strains. As plotted in Figure 1.7, the $|e_{31,f}|$ value shows a steady increase for PZT thin films integrated on silicon, outperforming epitaxial films. This is due to the integration and seeding issues which were solved in case of integrated PZT films on silicon in the 1990's. Epitaxial films exhibit less extrinsic contribution due to smaller population of a-domain with no significant improvement in the piezoelectric performance over the studied range.[34]
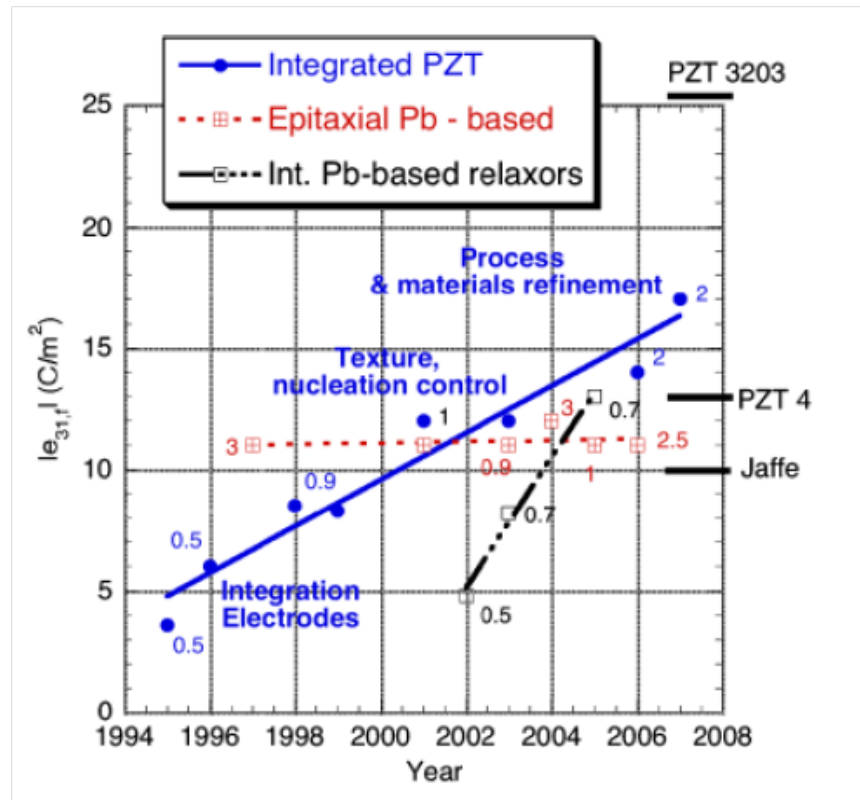
Figure 1.7 Reported $e_{31,f}$ values for lead-based thin films over the past 15 years

1.4 Summary

In this chapter, basic concepts of ferroelectricity, structure of perovskite ceramics and their main characteristics were described. Techniques for thin film fabrication were explained with the main focus on pulsed laser deposition (PLD) as the development technique used in this study. PLD system and component were introduced and most important PLD parameters such as substrate temperature and background gas pressure were discussed. Electrical and electromechanical properties of ferroelectric thin films were briefly reviewed and their major applications were summarized.

References

[1] H. D. Megaw, *Ferroelectricity in Crystals* (Methuen, London, 1957)

[2] W. G. Cady, *Piezoelectricity* (Dover Publications, New York, 1962)

[3] M. Deri, *Ferroelectric Ceramics* (Gordon and Breach, New York, 1969)

[4] J. C. Burfoot, *Ferroelectrics* (Van Nostrand, New York, 1967)

[5] B. Jaffe, W. R. Cook Jr., and H. Jaffe, *Piezoelectric Ceramics* (Academic Press, London, 1971)

[6] R. C. Buchanan, ed., *Ceramic Materials for Electronics - Processing, Properties and Applications* (Marcel Dekker, New York, 1986)

[7] Y. Xu, *Ferroelectric Materials and their Applications* (North Holland, Amsterdam, 1991)

[8] J. F. Nye, *Physical Properties of Crystals* (Clarendon Press, Oxford, 1990)

[9] A. Safari, R. Panda, V. F. Janas, *"Ferroelectric Ceramics: Processing, Properties and Applications"*, unpublished work

[10] D. Damjanovic, *Rep. Prog. Phys.* **61**, 1267 (1998).

[11] K. Uchino, *Ferroelectric Devices*, Marcel Dekker Inc. New York, 2000.

[12] M. E. Lines, A. M. Glass, *Principles and Applications of Ferroelectrics and Related Materials ,* 1979 (Oxford:Clarendon)

[13] M. J. Haun, E. Furman, S. J. Jang, H. A. McKinstry, L. E. Cross, *J. Appl. Phys.* **62,** 3331 (1987)

[14] S. Stemmer, S. K. Streiffer, F. Ernst, M. Ruhle, *Phil. Mag.* A **71,** 713 (1995).

[15] R. E. Newnham, *Structure–Property Relations* (Berlin: Springer) 1975.

[16] C. Tantigate, PhD thesis, Rutgers University, New Brunswick, NJ, 1996.

[17] J. –C. Lee, PhD thesis, Rutgers University, New Brunswick, NJ, 1994.

[18] J. A. Bellotti, PhD thesis, Rutgers University, New Brunswick, NJ, 2003.

[19] J. S. Horowitz, J. A. Sprague, *Pulsed laser deposition of thin films*, John Wiley and sons, 1994.

[20] R. E. Leuchtner, D. B. Chrisey, J. S. Horowitz, *SPIE Excimer laser*, **1835**, 31 (1991).

[21] C. M. Cotell, J. S. Horowitz, J. A. Sprague, R. C. Y. Auyeung, P. D. Antonio, J. Konnert, *Mat. Sci. Eng. B*, **32**, 221 (1995).

[22] T. Nakamura, Y. Yamanaka, A. Morimoto, T. Shimizu, *Jpn. J. Appl. Phys.*, **34**, 5150 (1995).

[23] J. Gonzalo, C. N. Afonso, J. Perriere, R. Gomez San Roman, *Appl. Surf. Sci.*, **96**, 693 (1996).

[24] B. Dam, J. H. Rector, J. Johansson, S. Kars, R. Griessen, *Appl. Surf. Sci.*, **96**, 679 (1996).

[25] M. Mertin, D. Offenberg, C. W. An, D. A. Wesner, E. W. Kreutz, *Appl. Surf. Sci.*, **96**, 842 (1996).

[26] D. V. Taylor, D. Damjanovic, *J. Appl. Phys.* **82,** 1973 (1997).

[27] A. K. Tagantsev, *Integr. Ferroelectr.* **16** 237 (1997).

[28] A. K. Tagantsev, M. Landivar, E. Colla, N. Setter, *J. Appl. Phys.* **78** 2623 (1995).

[29] U. Robels, J. H. Calderwood, G. Arlt, *J. Appl. Phys.* **77,** 4002 (1995).

[30] K. Lefki, G. J. M. Dormans, *J. Appl. Phys.* **76,** 1764 (1994).

[31] J. –F. Li, D. D. Viehland, T. Tani, C. D. E. Lakeman, D. A. Payne, *J. Appl. Phys.* **75** 442 (1994).

[32] J. –F. Li, D. D. Viehland, C. D. E. Lakeman, D. A. Payne, *J. Mater. Res.* **10,** 1435 (1995).

[33] N. Setter, D. Damjanovic, L. Eng, G. Fox, S. Gevorgian, A. Kingon, H. Kohlsted, N. Y. Park, G. B. Stephenson, I. Stolitchnov, A. K. Taganstev, D. V. Taylor, T. Yamada, S. Streiffer, *J. Appl. Phys.* **100**, 051606 (2006).

[34] P. Muralt, *J. Am. Ceram. Soc.* **91**, 5, 1385 (2008).

2 Literature Review on Lead-free piezoelectric ceramics and thin films

2.1 Introduction

For more than five decades, lead-based piezoelectric ceramics have been considered the most dominant piezoelectric materials due to their remarkable properties and relative low cost of processing. This was mainly owing to the existence of a Morphotropic Phase Boundary (MPB) between two ferroelectric phases which results in their effective poling and hence their outstanding electromechanical properties. In particular, $Pb(Zr_x,Ti_{1-x})O_3$ (PZT) has attracted a great deal of attention with large piezoelectric and coupling coefficients, as well as a high Curie temperature. Another great advantage of PZT composition was found to lie in its high solubility for various elements and therefore the possibility of formation of modified compositions with desirable properties. To exemplify, effects of La doping in PZT solid solution have been extensively studied and found to improve the piezoelectric properties of PZT. Therefore, PZT-based compositions have been dominantly used for numerous applications and commercially promoted for a variety of devices, namely, sensors and actuators, transducers. However, in the past couple of decades, certain disadvantages have been raised to affect the use of lead-based piezoelectric ceramics in commercial applications. Lead and its derivatives, particularly lead oxide (PbO) have been found to be toxic and globally considered a hazardous material. On the other hand, processing of PZT-based compositions, e.g. calcination and sintering, containing more than 50Wt% PbO, is mostly carried out at elevated temperatures, typically above 1000^oC. At such high temperatures, lead is volatilized and extensively evaporates into the environment. As a result, restrictions have been legislated for near future in many countries around the world, including European

Union and Japan, to limit the use of lead for civil applications. Consequently, a new surge has been induced in order to find lead-free piezoelectric compositions with comparable properties to their lead-based counterparts. Lead-free piezoelectric ceramics in various categories have been studied to explore the possibility of new systems with moderately high electromechanical properties. Among the most researched lead-free compositions, are perovskite barium titanate, alkaline niobates and bismuth sodium titanates. A summary of the properties of some of lead-free compositions is shown and contrasted with those of PZT-based compositions in Table 2.1.

In this chapter, first, primary lead-free compositions as well as their most recent modification are introduced, and their piezoelectric properties are discussed. Second and more importantly to the goal of this thesis, the state-of-the-art techniques for development of lead-free piezoelectric thin film are briefly described and recent advances in such thin films are overviewed.

Table 2.1 Dielectric and piezoelectric properties of basic Pb-free and PZT compositions

Material	e/e_0	tan d	d_{33} (pC/N)	k_p	T_c	$T_{o\text{-}t}/T_d$
$(K_{0.5},Na_{0.5})NbO_3$*	500	0.04	95	0.35	400	195/-
$(Bi_{0.5},Na_{0.5})TiO_3$	300	0.01**	98	0.2	315	-/200
BaTiO3	1700	0.005	190	0.36	115	5/-
PZT-4	1300	0.004	289	0.58	328	-

* With additives, e.g. Mg, Ca, Ba
** BNT-BT6%

2.2 Alkaline Niobates

Since the discovery of ferroelectricity in potassium niobate, $KNbO_3$ (KN) composition by Matthias in 1950's **[1]**, several solid solutions were formed with KN and various end members including $NaNbO_3$ (NN). Potassium niobate itself shows a phase transition sequence reminiscent to $BaTiO_3$ (BT), as illustrated in Figure 2.1, however, with transition temperatures much higher than those of BT. Sodium niobate (NN), specifically was studied extensively and shown to form an MPB with KN, according to Shirane et al. Phase diagram of the KNN solid solution is shown in Figure 2.2. **[2]**
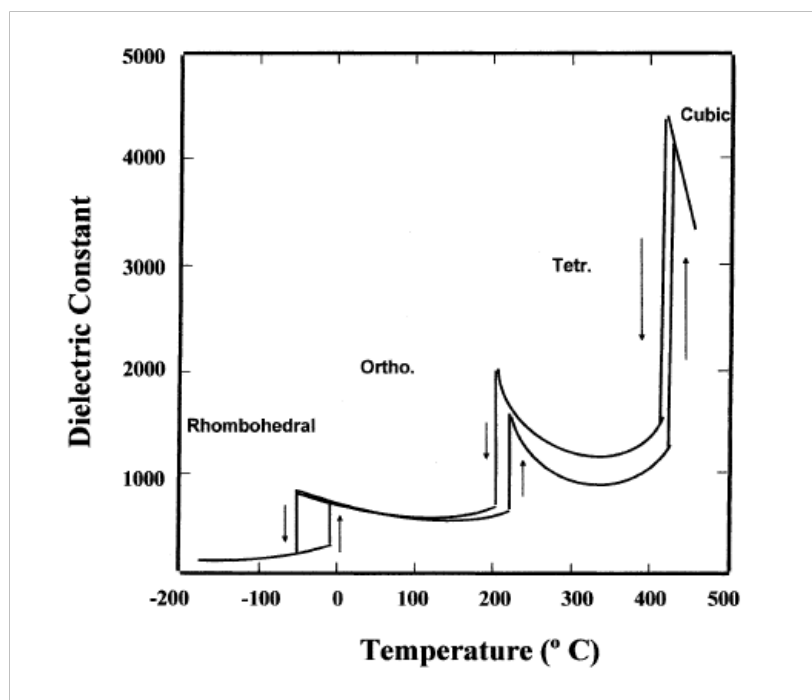
Figure 2.1 Phase transitions sequence in KNbO$_3$
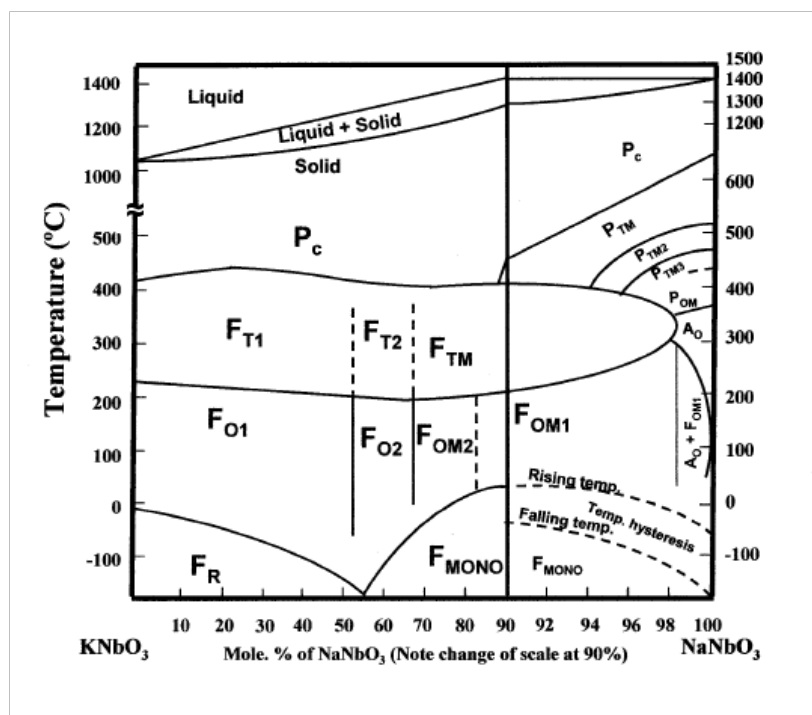
Figure 2.2 Phase diagram of KNbO$_3$-NaNbO$_3$

KNN-based compositions were the focus of great deal of research in the past few years after the pioneering work by Saito et al, **[3]** showing incredible piezoelectric properties in modified KNN system, comparable to those of PZT4 at room temperature. Addition of $LiTaO_3$ and $LiSbO_3$ to KNN system resulted in a tremendous improvement in the piezoelectric performance of this composition. This discovery triggered an enormous amount of interest in researchers to investigate the origin of the mentioned enhancement in KNN properties and explore the possibility of further progress.

2.2.1 Modifications to KNN composition

As mentioned earlier, addition of Li, Ta, and Sb showed to improve the piezoelectric properties of KNN system. Although, it was proposed to be due to the existence of a MBP in KNN-LT and KNN-LT-LS, however, several recent reports have shown that the high piezoactivity of KNN-LT-LS system was mainly due to the shift of a polymorphic phase transition (PPT) between ferroelectric tetragonal and orthorhombic phases, present in KNN phase diagram. **[4,5]** The presence of such phase boundary dictates instability in the electrical properties with temperature, making the composition unsuitable for a variety of applications. There have been, therefore, studies to investigate the effect of different dopants to shift the PPT boundary to both higher or lower temperatures, and hence avoiding the unstable region. Some of the major modifications to KNN compositions are concisely explained in the following sections.

I. $(K_{0.5},Na_{0.5})NbO_3$-$LiTaO_3$ (KNN-LT)

Hollenstein et al reported a d_{33} of over 300 pC/N and k_t of 52% for Li and Ta–substituted KNN ceramics, prepared at pressure-less sintering, comparable with those of hard PZT compositions. [6] Additionally, an MPB between orthorhombic and tetragonal phases was apparently observed in (1-x)KNN-xLT at x=5–6 mol.% by Guo et al. A d_{33} value of ~200 pC/N and k_p of ~36% were achieved in such MPB composition. [7] Shortly afterwards, Saito et al released their results on KNN-LT system, reporting a d_{33} of 230 pC/N, k_p of 50.5% and a relative permittivity of 1256. [8] Interestingly, the significant enhancement in the piezoelectric properties of KNN was attributed to the existence of MPB between orthorhombic and tetragonal phase, in all the previously mentioned studies. It was later shown by Dai et al, that the notable properties of KNN-LT ceramics around RT is in fact associated with the shift of orthorhombic-tetragonal phase transition (T_{o-t}) in KNN phase diagram to the vicinity of RT. [9] This hypothesis was further approved by others, and was generally considered as the basis of room temperature instability in the properties of modified KNN compositions. This could be explained as a drastic increase of T_c and decrease of T_{O-T} (down to RT) upon addition of $LiTaO_3$ into the composition. Furthermore, it was shown by Wang et al that addition of Li and Ta in KNN system through conventional method leads to remarkable compositional inhomogeneity, which could be diminished by pre-reacting the Nb and Ta through formation of $(Nb,Ta)_2O_5$ solid solution. [10] It was suggested as an efficient way to achieve compositionally well-homogenized ceramics and thus to obtain improved and reproducible electrical properties. In another report by Wang et al, processing of KNN-LT composition was studied as a function of annealing temperature, time and

environment. A secondary phase, having a partially filled tungsten bronze structure and a saturated Na content, was observed to precipitate and evolve in the form of abnormal grains. The T_{o-t} and hence the final electrical properties of the composition were shown to be influenced greatly by the compositional changes, made by significant volatilization of K, in particular and segregation of Na and probably Li during annealing in unprotected atmosphere, e.g. unsealed crucible. [11] Therefore more attention must be paid in processing of this complex system to control the compositional homogeneity. Individual effects of Li and Ta in the phase transitional behavior and electrical properties of KNN will be further discussed in section IV.

II. $(K_{0.5},Na_{0.5})NbO_3$-$LiSbO_3$ (KNN-LS)

Effect of $LiSbO_3$ substitution on the properties and transitional behavior of KNN system was investigated by Zhang et al. (1-x)KNN-xLS, x = 0.052 with densities greater than 95% exhibited good piezoelectric properties near RT with electromechanical coupling factors of k_p of 27%, k_{33} of 62% and k_{31} of 30%, and piezoelectric coefficients of d_{33} of 265 pC/N and d_{31} of −116 pC/N. [12] The improvement in piezoelectric behavior at room temperature is achieved by shifting the polymorphic phase transition from 200 °C for the pure KNN to approximately 35^oC, increasing the polarizability. Also, the observed mixed piezoelectric soft and hard behaviors in KNN-LS composition was attributed to the distinctly different domain states, associated with orthorhombic and tetragonal phases. This was evidenced by the simultaneous increase of coercive field and piezoelectric coefficient and corresponding softening of the elastic properties. In addition, decrease of coupling factor after thermal cycling was related to cycling through regions

with distinct domain states in the two-phase region. Individual effect of Sb on the phase transition temperatures of KNN composition will be reviewed in section IV.

III. Effects of doping in A-site and B-site cations

Effect of Li substitution in KNN composition has been investigated by several groups. Guo et al first reported large d_{33} of 235 pC/N with fairly high k_p of 44% in (1-x)KNN-xLiNbO$_3$, x = 0.06. [13] This increase was initially attributed to the formation of an MPB between tetragonal and orthorhombic phase in KNN-LN phase diagram at x = 0.06. Kakimoto et al used the Raman scattering to study the structure of (1-x)NKN-xLN ceramics (0 < x < 0.70) and showed excellent piezoelectric properties at compositions with x = 0.05-0.07. [14] The measured Raman-active vibrations were classified as lattice translations involving the motion of the alkaline cations and the internal modes of the NbO$_6$ octahedra. On the basis of their transitions, it was concluded that NKN and LN form a solid solution as a single phase in the orthorhombic side of the MPB corresponding to the orthorhombic-tetragonal transition, however heavy distortion of NbO$_6$ octahedra and formation of a KLN secondary phase begin to occur on the tetragonal side of the MPB composition with increasing x (LN). Wang et al on the other hand, indicated that addition of excess Na$_2$O reduced sintering temperature of (1-x)(Na$_{0.535}$,K$_{0.48}$)NbO$_3$–xLiNbO$_3$ (x = 0.058–0.090) ceramics to 950 °C, and enhanced piezoelectric coefficient d_{33} of 280 pC/N and k_p of 48.3% were obtained at x = 0.080. Moreover, the d_{33} of such composition showed relative temperature stability around RT with 15% decrease up to 100°C. [15]

Among niobate perovskites with monovalent A-site cations, in addition to $LiNbO_3$, $AgNbO_3$ solid solution with KNN was shown to have interesting piezoelectric performance. Ye et al reported an increase in d_{33} at x = 0.2, while the T_{o-t} showed a monotonic decrease with Ag over the whole range of study (x = 0-0.4). **[16]** Also, the measured high d_{33} of 186 pC/N at RT for x = 0.2 was reported with T_{o-t} occurring at 170^oC. Therefore the increase in piezoelectric properties of KNN-$AgNbO_3$ appeared to be distinct in mechanism than previously reported KNN-LT or KNN-LS, which was based on the shift of polymorphic phase transition to RT. Effect of lithium and silver addition on the phase diagram of KNN system is demonstrated in Figure 2.3.

Various B-site cations have also been attempted substituting for Nb in KNN system, mainly to improve the densification and sintering behavior in addition to piezoelectric performance. Effect of Sb and Ta on the phase transition temperatures of KNN composition is summarized in Figure 2.4. Both cations substituted the B-site cation, were shown to decrease the transition temperatures, T_C as well as T_{O-T}, with Ta being more significant.

Forming solid solution of KNN with metal titanates, such as $CaTiO_3$, $BaTiO_3$, etc. has also been explored by many groups and various studies have been reported on the electromechanical properties of such solid solutions as a function of titanate end member content. Introducing $SrTiO_3$, $BaTiO_3$, $CaTiO_3$ in KNN composition showed an improvement in densification of KNN samples via formation of a liquid phase and resulted in large grains microstructure.**[17-19]** However, T_C peak was broadened with increasing CT and BT content, which indicates diffuse phase transition from tetragonal to cubic phase and the change from a normal ferroelectric to a relaxor type. $(Ba,Sr)TiO_3$

addition on the other hand resulted in a decrease in grain size of KNN samples even at low doping levels. In general, addition of titanates, regardless of the A-site elements, showed dramatic decrease in T_C and T_{O-T} transition temperatures, with T_{O-T} showing no dependence on the A-site element. **[20]** In addition, T_C exhibited decreases quite similarly with different titanate's A-site elements. This is summarized in Figure 2.5.
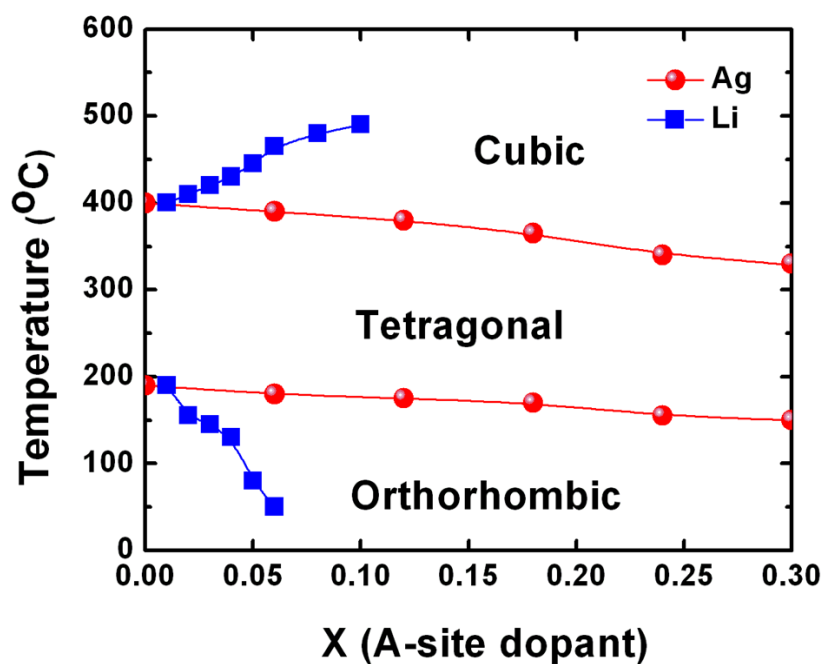
Figure 2.3 Effect of A-site cations (Li, Ag) on the transition temperatures of KNN system
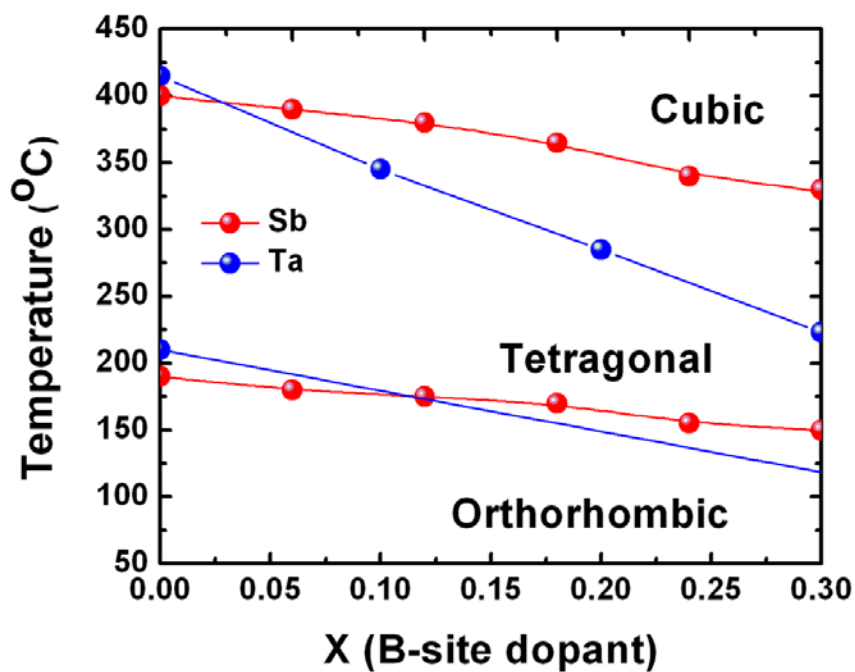
Figure 2.4 Effect of B-site cations (Ta, Sb) on the transition temperatures of KNN system
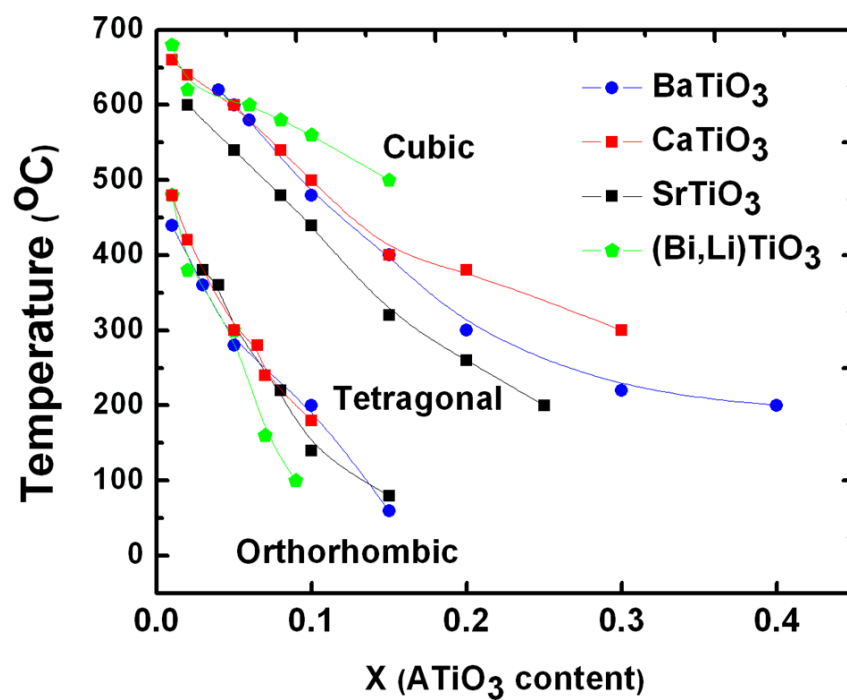
Figure 2.5 Phase diagram of KNN-MTiO$_3$ solid solution systems

Effect of manganese addition/substitution in KNN-based compositions has been reported in the past couple of years. Manganese has shown to improve the sinterability of KN through B-site substitution, and exhibited a hardening effect, thus enhancing the poling state under higher temperature and electric field. **[21]** This then led to increase in the piezoelectric properties of KN samples. On the other hand, it was shown that introduction of 1 mol% Mn in KNNT system decrease the T_{o-T} down to RT while having no effect on T_c. As a result, dielectric permittivity and d_{33} showed a moderate increase at RT. **[22]**

Addition of Cu in KNN-LT-LS composition was studied as a function of additive content by Hagh et al, **[23]** where an increase in grain size and a change in growth behavior was observed. Moreover, addition of Cu was shown to stabilize the orthorhombic phase through shifting the T_{o-t} to higher temperature while showing no change in T_c. As a result, d_{33} and k_p were slightly degraded and dielectric loss was drastically decreased. Another study carried out by Hagh et al was involved with Ba-substitution in KNN-LT-LS compositon. **[24]** Incorporation of the Ba^{+2} shifted the Curie temperature downward and increased the room temperature relative permittivity. This was accompanied by a broadening of the relative permittivity-temperature peak. The bulk resistivity of KNN-LT-LS increased with increasing barium content and then dropped at high Ba^{2+} concentration (>1.5 mol%).The dielectric and piezoelectric properties along with the polarization and coercive field results implied that soft piezoelectric characteristics could be achieved.

IV. KNN-LT-LS

As discussed earlier in this chapter, solid solution of KNN with LT and LS simultaneously resulted in significant improvement of piezoelectric properties with d_{33} over 300 pC/N, k_p of and k_t of , initially reported by Saito et al in 2004, followed by Hagh et al in 2006, **[25]** demonstrated the highest achievable properties in the KNN-based system. Hagh et al, systematically studied the effect of various processing parameters, such as oxygen annealing and purity of precursor materials. It was shown that the samples, prepared with high purity raw materials, sintered under oxygen flow exhibited much larger relative permittivity as well as a high d_{33} of 350 pC/N.

Table 2.2 summarizes major KNN-based ceramics with their most important electrical properties.

Table 2.2 Properties of some of KNN-based compositions

Material	$\varepsilon/\varepsilon_0$	tan δ	d_{33} (pC/N)	k_p	T_c	T_{o-t}	Ref
$(K_{0.5},Na_{0.5})NbO_3$	290	0.04	80	0.35	420	195	Egerton et al
$0.93KNN-0.07LiNbO_3$	950	0.08	240	0.45	460	20	Hollenstein et al
$0.82KNN-0.18AgNbO_3$	500		175	0.42	360	160	Ye et al
KNNT-Mn	1490	0.017	240	0.45	193	23	Watanabe et al
KNN-Ba(1%)	580	0.035		0.32			Maeder et al
$0.95KNN-0.05SrTiO_3$	950		200	0.37	277	27	R. Wang et al
$0.95KNN-0.05BaTiO_3$	1058		225	0.36			Park et al
$0.95KNN-0.05LiTaO_3$	570	0.04	200	0.36	430	55	Guo et al
KNN-LT	1210	0.024	215	0.35	320	50	Y. Wang et al
$KNN-LiSbO_3$	1380	0.02	265	0.5	392	45	Zhang et al
$KNN-LS-CaTiO_3$	1000		210				Zhang et al
$0.95KNN-0.05CaTiO_3$	1316		241	0.41			Park et al
KNN-BNT	~600		195	0.43	375		Zuo et al
KNN-LT-LS	1650	0.024	340	0.48	264	31	Hagh et al

V.   State-of-the-art processing

In order to improve sinterability of KNN-based ceramics, several diverse methods have been utilized. Hot pressing of KNN ceramics have been the earliest technique to obtain high density samples. Jaeger et al in 1962 conducted a study on hot-pressing of KNN ceramics and demonstrated a very marked change in microstructure of the samples with virtually no residual porosity. [27] These high density ceramics showed a high dielectric constant and enhanced piezoelectric characteristics.

Spark plasma Sintering (SPS) has been recently exploited for production of dense dielectric materials, although it has been traditionally used for metal and engineering ceramics. Wang et al reports the SPS sintered KNN ceramics, with a wide range of composition and showed a decrease in the relative densities with increasing Na content. [28] The relative density of the $Na_{0.2}K_{0.8}NbO_3$ reached the highest value of 98%, in $(Na_xK_{(1-x)})NbO_3$ system ceramics prepared by all kinds of methods.

Apart from various techniques to process KNN-based samples, many researchers have sought ways to improve the densification in conventional processing methods. Lee et al investigated addition of K_2O and Na_2O in solid state reaction processing to offset the volatile mass and enhance sinterability. Interestingly, it was shown that although addition of excess 44mol% K along with 22mol% Na resulted in a ~30% improvement of d_{33}, relative permitivity displayed no significant change, while k_p decreased and tan δ increased significantly.[29]

Bernard and Kosec et al showed an improvement in the densification of KNN ceramics by the addition of a small amount (from 0.5 to 4 wt%) of (K, Na)-germanate, which melts at around 700^oC. Germanate-modified KNN ceramics were shown be

sintered to high density (95.6 % TD) at 1000^oC, which is over 100^oC lower than that is usually required for pure KNN. It was suggested that the addition of a sintering aid not only improves the densification but also preserves the good piezoelectric properties of KNN. **[30]**

2.3 Bismuth Sodium Titanate

Bismuth sodium titanate, $(Bi,Na)TiO_3$, (BNT) perovskite ferroelectrics have also been center of global attention in the past decade as a promising alternative to lead-based ferroelectrics. First revealed to be ferroelectric by Smolenski in 1961, BNT was found to be an excellent piezoelectric material with a moderately high T_c of 320^oC, high Pr of 38 $\mu C/cm^2$ and d_{33} of 73. **[31,32]** However, one of the major challenges in the performance of undoped BNT piezoelectric ceramics exist due to their very large coercive field (above 70kV/cm) and high conductivity, which leads to insufficient poling and thus underdeveloped piezoelectric performance. On the other hand, preparation of BNT-based compositions is relatively easy and less complicated as compared to KNN-based ceramics. Therefore, it is essential to seek alternative routes e.g. formation of MBP in solid solutions to obtain high piezoelectric performance in such system without losing the ease of processing. Numerous reports have demonstrated the existence of such MPB in BNT-based solid solution. In PZT-based compositions the MPB is a temperature-independent boundary at around 52/48 PT/PZ molar ratio, whereas in BNT-based systems phase diagram it is curved and hence temperature-dependent. Furthermore, existence of a non-polar state in the BNT-based system phase diagram, leads to a low depolarization temperature, T_d, above which piezoelectricity of the samples is vanished. A great deal of research on BNT-based compositions has been done in Takenaka's group at Tokyo University.

2.3.1   Binary and ternary BNT-based solid solutions

Sasaki et al demonstrated the formation of an MPB between binary BNT-BKT solid solution, in the range of 0.16-0.2 BKT. A k_p of 31%, k_t of 42% and dielectric permittivity of 1030 was achieved for MPB BNT-BKT composition. [33]

Takenaka et al reported an MPB region in (1-x)BNT-xBT system at x = 0.06-0.07 with a T_c of 288°C and a low depolarization temperature (T_d) of 130°C, above which an antiferroelectric phase is formed based on X-ray diffraction data. [34]

$[Bi_{0.5}(Na_{1-x-y}K_xLi_y)_{0.5}]TiO_3$ (BNKLT) lead-free piezoelectric ceramics have been developed by Lin et al and their piezoelectric and ferroelectric properties have been studied. [35] The partial substitution of Na^+ by K^+ and Li^+ effectively decreased the coercive field E_c but simultaneously maintain the very strong ferroelectricity, which results in an obvious improvement on the piezoelectric properties. A d_{33} of 231 pC/N, k_p=41.0%, k_t of 50.5%. were reported as the optimized electromechanical properties of BNKLT with x = 0.15 and y = 0.075.The depolarization temperature T_d of such ceramics, was reported to be approximately 195 °C. Also, Hiruma et al carried out a detailed study on the phase transition temperatures such as T_d, T_{R-T} and piezoelectric properties of BNT-BKT-BLT. [36] It was realized that the variation of T_d is related to the variation of lattice distortion such as rhombohedrality 90-α and tetragonality c/a. It was demonstrated that a small amount of Li-substitution (0.04) was very effective for increasing the T_d, and that of BNLKT increased from 185°C to 221°C at the rhombohedral composition. It was also observed that T_d drastically decreased with increasing the amount of Li-substitution.

Nagata et al investigated the dielectric and piezoelectric properties of solid solutions of the ternary system, aBNT–bBT–cBKT, focusing on the MPB between tetragonal and

rhombohedral phases. **[37]** In their work, it was demonstrated that the maximum d_{33} of 191pC/N, was obtained for a/b/c = 85.2/2.8/12 with the tetragonal phase around the MPB region. The T_c, k_{33}, and relative permittivity of such composition were found to be 301°C, 0.56 and 1141, respectively. In a separate study by Wang et al, variations of the electrical properties and structure with the amount of BKT have been examined. **[38]** During sintering, the incorporated BKT diffuses into the lattice of BNT–BT-based composition to form a solid solution. The incorporation of 5mol% BKT was shown to significantly enhance the piezoelectric properties, increase the remanent polarization; however, it did not result in any reduction of T_d.

Another study in Takaneka's group focused on the phase transition temperatures of BNKT-BT solid solution as a function of the amount (x) of BNT using electrical measurements. **[39]** The depolarization temperature, T_d, for BNT-based ceramics was clearly determined by measuring the dielectric properties of fully poled samples. T_d corresponds to the temperature of the phase, in the impedance frequency characteristic of the fully poled longitudinal (33) mode. An approach as to identify the rhombohedral–tetragonal phase transition temperature, T_{R-T}, on the rhombohedral side was suggested and T_d and T_{R-T} were clarified thereby. It was then realized that T_{R-T} corresponds to the T_d at x = 0.94. An intermediate phase, which is antiferroelectric or ferroelectric and antiferroelectric coexistance, was shown to exist at temperatures higher than the T_d around the MPB.

With the purpose of enhancing the strain and displacement properties for piezoelectric actuator applications, the possibility of formation of BNT-KNN solid solution has been explored in the past few years, following the successful development of

individual compositions. Zhang et al observed a giant electric-field-induced strain of 0.45% in the lead-free 0.92BNT-0.06BT-0.02KNN system. **[40]** This giant strain was attributed to the disruption of long-range ferroelectric order and field-induced antiferroelectric-ferroelectric transition. Later, Jo et al investigated the origin of the giant piezoelectric strain in 0.92BNT−0.06BT−0.02KNN by comparing polarization and strain hysteresis with those of 0.93BNT-0.06BT−0.01KNN. **[41]** It was demonstrated that the enhanced unipolar strain was closely related to a reduction in the remnant strain S_{rem} due to a dominant presence of a nonpolar phase at zero electric field. It was then proposed that the giant strain originated from a combined effect of the intrinsically high poling strain S_{pol} of BNT-BT based systems, the presence of a nonpolar phase at zero electric field which destabilizes and randomizes an electrically induced ferroelectric order, and an easy transition between the nonpolar and ferroelectric phases due to their comparable free energies. Some of the BNT-based solid solutions and their electrical properties are presented in Table 2.3, where properties were fine-tuned by modifying the composition for actuator applications with higher d_{33} in 0.852BNT-0.12BKT-0.028BT and high power applications with a larger Q_m in 0.92BNT-0.04BLT-0.08KT with 0.6mol% added Mn.

Table 2.3 Properties of some of BNT-based solid solution systems

Material	$\varepsilon/\varepsilon_0$	tan δ	d_{33} (pC/N)	k_p	T_c	T_d	Q_m	Ref
0.94BNT-0.06BT	580	0.013	125		288	150	81	Takenaka et al
0.8BNT-0.2BKT	1030	-	47 (d_{31})	0.27	-	-	109	Sasaki et al
0.7BNT-0.1BLT-0.2BKT	1200	0.045	231	0.41	-	160	-	Lin et al
0.92BNT-0.04BLT-0.08BKT-(0.6%Mn)	493	-	85	0.23	272	200	700	Hiruma et al
0.852BNT-0.12BKT-0.028BT	999	-	181	0.319	-	113	84	Hiruma et al
0.81BNT-0.16BKT-0.03NN	1005	0.037	146	0.3	289	190	-	Yuan et al

2.4 Thin films progress

For applications such as MEMS devices or non-volatile memories, similar to composites and transducers, PZT has been the most popular composition among all the piezoelectric/ ferroelectric materials. There has been systematic studies in the late 80's and 90's on PZT-based thin films, developed by different techniques, such as sol-gel, RF sputtering and pulsed laser deposition, so as to highly optimize the ferroelectric and piezoelectric properties and obtain similar values to the bulk PZT.[41,42] However, in case of lead-free piezoelectric thin films, especially the fabrication of KNN-based thin films is rather complicated due to its highly volatile constituents, namely sodium and potassium and requires a judicious control of the deposition parameters. Following is a brief review of what has been achieved in the development of most important lead-free thin films, namely of KNN-based and BNT-based compositions.

2.4.1   KNN-based thin films

KNN-based thin films have been fabricated using different techniques, such as RF magnetron sputtering, metal-organic chemical vapor deposition (MOCVD), sol-gel deposition and pulsed laser deposition (PLD).[43-49] Many have reported loss of the monovalent elements present in this composition, during the sputtering, PLD or sol-gel deposition.[49-51] Preserving volatile potassium and sodium contents in the films, and avoiding pyrochlore formation were found to be the major challenges in development of thin films. In order to overcome the elemental loss issue, it was suggested and further

attempted that excess amount of the volatile species be provided into the precursor materials. **[52]**

As mentioned earlier, sol-gel processing, rf sputtering and PLD were among the most popular techniques to fabricate KNN-based thin films. Sol-gel processing of KNN-based thin films has been studied by several research groups, due to the ease of processing and possibility of large area film production. **[51-56]** As a result of the elemental loss and hence chemical deviations from stoichiometry, KNN films exhibited high leakage current densities. Ahn et al showed a decrease of an order of magnitude in leakage current density by addition of 20 mol% K and Na excess precursor solution, as indicated in Figure 2.6. **[52]** Enhanced ferroelectric properties were reported by Ahn et al and Lai et al **[53-55]** in Li-substituted KNN thin films by chemical solution deposition (CSD). Ahn et al showed that 5 mol % LN in 350 nm KNN thin films inhibited generation of secondary phase, and improved the morphology with reducing the porosity and increasing the grain size. The 0.95NKN-0.05LN thin film showed well saturated *P-E* hysteresis loop, as shown in Figure 2.7, with a remnant polarization P_r and coercive field E_c values reaching 10 μC/cm^2 and 45 kV/cm, respectively. On the other hand, Lai et al found a very similar results at x= 0.06, shown in Figure 2.8, with maximum local effective piezoelectric d_{33} and remnant polarization P_r of 192 pm/V and 9.7 μC/cm^2 respectively, which is comparable to the PZT films. However, LKNN films exhibited no improvement in resistivity as compared to KNN thin films.
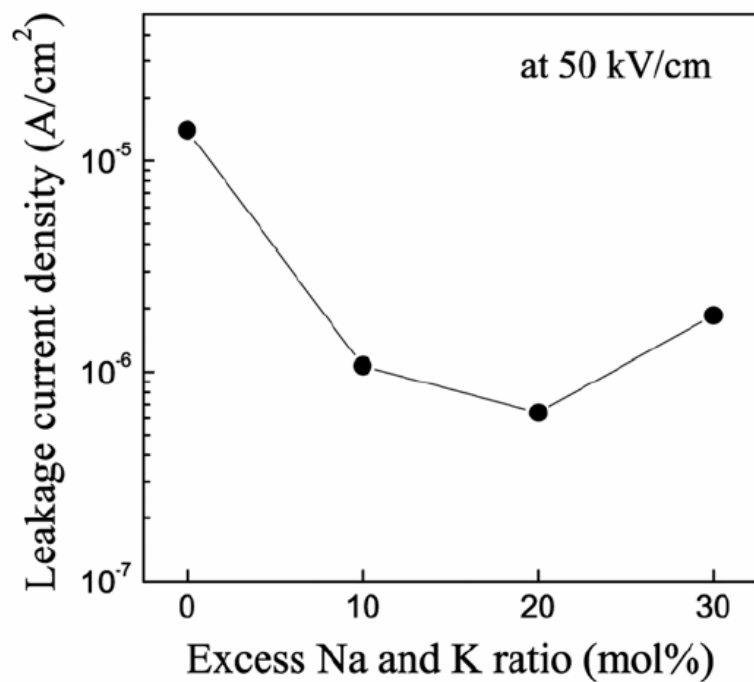
Figure 2.6 Leakage current density of KNN thin films as a function of excess precursor solution
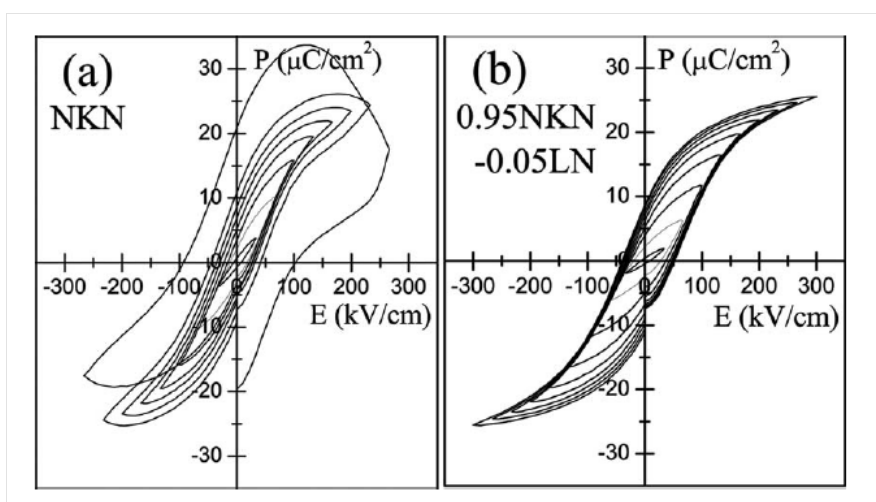
Figure 2.7 PE loops of 350 nm a) KNN and b)0.95KNN-0.05LN thin films
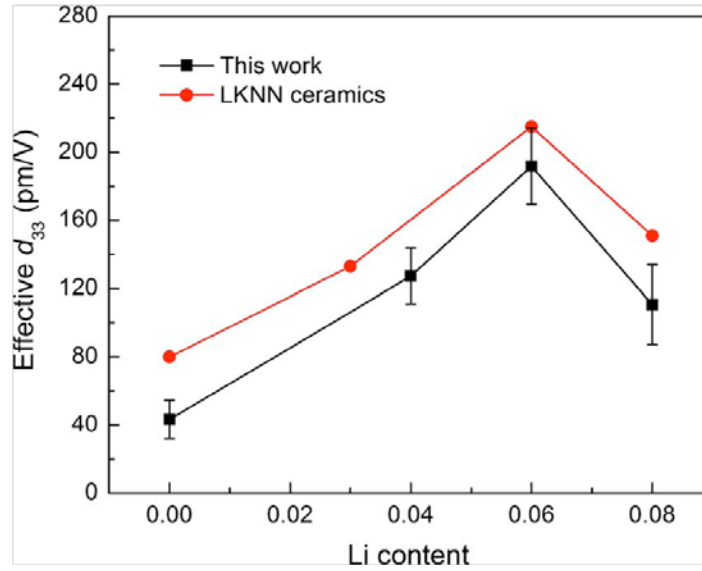
Figure 2.8 d_{33} of KNN-0.06LN thin films with 400nm thickness

In addition to sol-gel processing, there are several reports in the literature on development of KNN-based thin films on various substrates by sputtering technique. **[57-59]** Shibata et al reported high-quality KNN films on Pt/MgO substrates with a transverse piezoelectric coefficients e_{31} (d_{31}/s_{11}) of 3.6 C/m^2. Compared to polycrystalline thin films on Pt/SiO$_2$/Si substrate with e_{31} of 5.5 C/m^2, the value of e_{31} was smaller which was attributed to the epitaxial quality of the films. Similarly, dielectric constant values were higher for the polycrystalline films on Pt/SiO$_2$/Si compared to Pt/MgO substrate, being 185 and 598 respectively. **[57]** The effect of post-annealing for NKN thin films on the Pt/Ti/SiO$_2$/Si substrates deposited by rf sputtering was studied at various temperatures by Lee et al. **[58]** Post annealing resulted in a significant improvement of polarization as compared to in-situ films. The film annealed at 700 ^{o}C exhibited a perovskite orthorhombic structure with a high P$_r$ of 25 μC/cm^2 and E$_c$ of 90 kV/cm. Also, XRD results indicated that the crystallinity of the films, presented as the broadness of the

peaks, as well as the surface roughness were improved with increasing annealing temperature. Wu et al studied phase transitions and electrical behavior in 300 nm $(K_{0.5}Na_{0.5})NbO_3$ thin film deposited on the $SrRuO_3$-buffered <100> $SrTiO_3$ substrate by off-axis rf magnetron sputtering and observed a strong (100) preferred orientation. The phase transition temperatures were shown to be lower than those in the bulk ceramic, namely 120^oC and 310^oC for T_{O-T} and T_C as compared to 190^oC and 410^oC for those of ceramic. A P_r of 12 $\mu C/cm^2$ and almost fatigue-free up to 109 switching cycles were observed for the KNN thin film, and demonstrated in Figure 2.9 and Figure 2.10 respectively. A higher dielectric constant of 452 at 1 kHz as compared to that of bulk, being 417, and lower dielectric loss of 1.7% as compared to 2-3% for bulk, was observed in the films with enhanced polarization, the latter being related to the presence of preferred <001> orientation in the films. Oxygen vacancies were shown to be involved in the conduction process of the KNN thin film, with activation energy of 0.93 eV, being close to the average value of 1eV for most oxide thin films.[59]
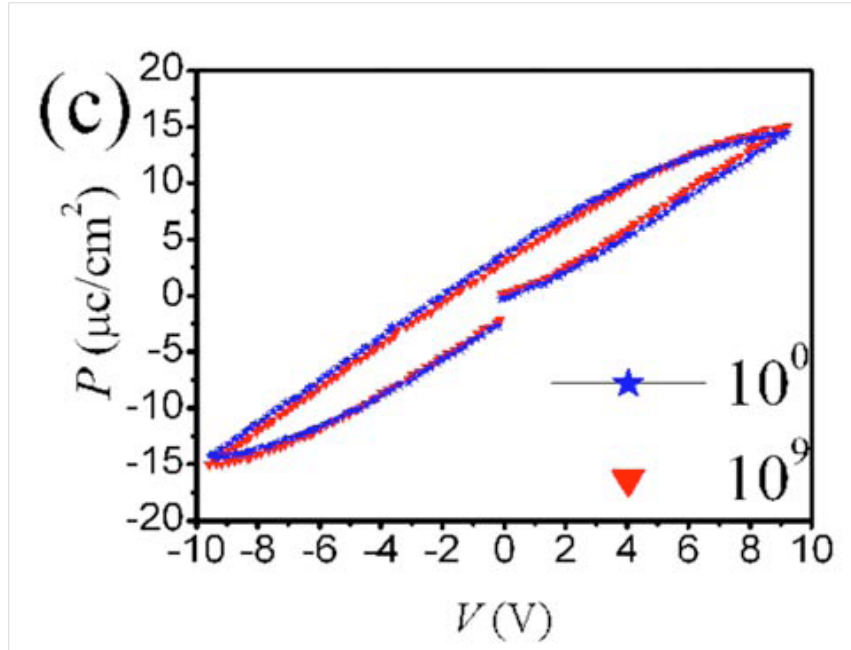
Figure 2.9 PE loops of 300 nm KNN thin films on SRO/(100)STO
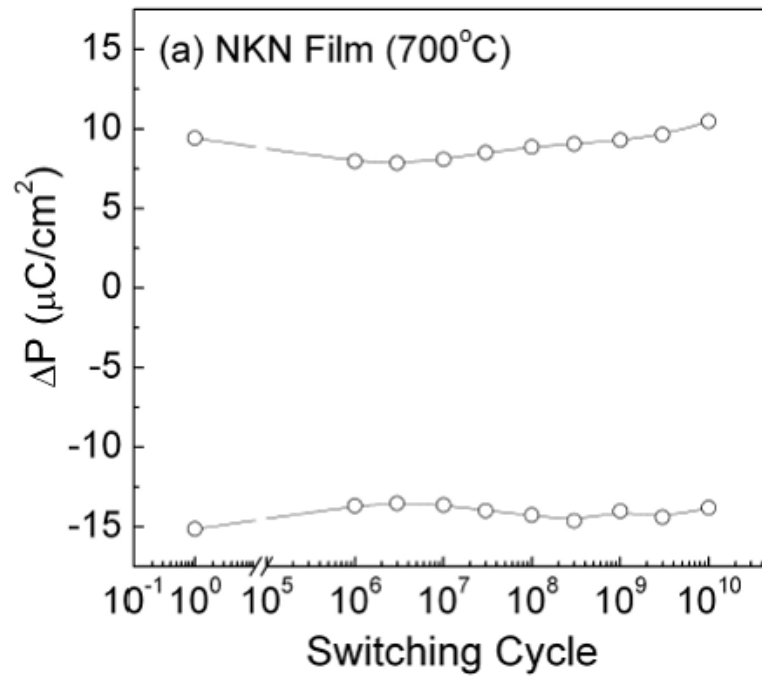
Figure 2.10 Fatigue tests at 1 MHz for 300 nm KNN thin films on SRO/(100)STO

Also, pulsed laser deposition (PLD) of KNN-based thin films has been explored, due to the versatility of the technique and ease of processing. **[43,45,49,50,60]** As mentioned earlier, the loss of volatile elements has remained a challenge for the deposition of KNN-based thin films. That is particularly important for KNN-based systems, as they contain at least two volatile species (K^+, Na^+), which are also light elements. Therefore, the growth of KNN-LT-LS films is prone to the so-called "thermalization problem" in addition to the complications associated with volatilization.**[43]** The effect of oxygen partial pressure (P_{O_2} hereafter) during PLD film synthesis on the properties of lead-based films was shown to play a critical role in suppressing Pb volatilization and in ensuring proper oxygen stoichiometry concomitantly. **[61-64]** Cho et al. has demonstrated that decreasing the P_{O_2} led to the formation of pyrochlore phases in KNN films and proposed that discriminated thermalization is the underlying phenomenon, while making no reference to the effect of P_{O_2} on gas-solid phase equilibrium in the context of preserving film stoichiometry.**[65]** Also, Wada et al reported the deposition of epitaxial KNN-LT-LS thick films with <001> preferred orientation on $SrTiO_3$ substrate. A P_r of 3.7 $\mu C/cm^2$ was obtained in these thick films, as shown in Figure 2.11, while compositional analysis revealed an increase of K content across the thickness of the film with a more stoichiometric composition at the film's surface.**[45, 66]**
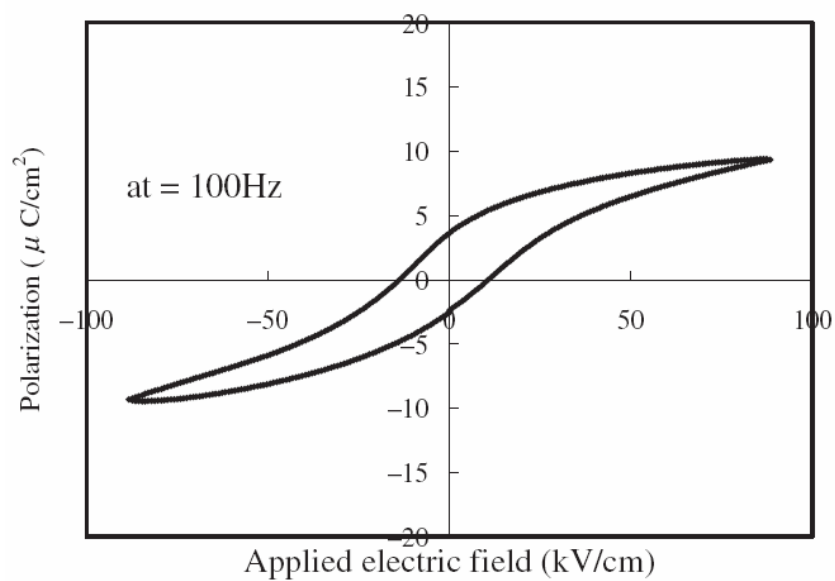
Figure 2.11 Polarization hysteresis loop of 2.8 μm thick KNN-LT-LS films

2.4.2   BNT-based thin films

Similar to KNN-based thin films, BNT-based thin films have been fabricated previously by various techniques. Sol-gel processing has been widely used for development of BNT-based thin films by many researchers. [67-70] Yu et al demonstrated polycrystalline ferroelectric lead-free $Bi_{0.5}$-$Na_{0.5}TiO_3$ (BNT) thin films on $Pt/Ti/SiO_2/Si$ substrates by a modified sol–gel spin-coating process. [66] Dielectric constant and loss of such 600nm thin films at 100 kHz were found to be 277 and 0.02, respectively, with P_r and E_c of 8.3 $\mu C/cm^2$ and 200 kV/cm, respectively, under electric field of 1100 kV/cm. Tang et al. [68], obtained highly (111)-textured growth in BNT thin films on $Pt/Ti/SiO_2/Si$ substrates by a *sol-gel* process, while a slight (100) preferential orientation was found in $(Bi_{0.5},Na_{0.5})TiO_3$-$BaTiO_3$ thin films on (100) MgO substrates by Scaisoreanu.[71] Additionally, Cheng et al. fabricated $(1-x)(Bi_{0.5},Na_{0.5})TiO_3$-$xBaTiO_3$ thin films on (00*l*) $LaAlO_3$ substrates by pulsed laser deposition with a combinatorial methodology, was developed to accelerate the process of materials discovery and optimization. [72] Guo et al followed a chemically modified solution to develop [001]-oriented $(Na_{0.5}Bi_{0.5})_{0.94}Ba_{0.06}TiO_3$ films with thickness of 250 nm on LNO/γ-Al_2O_3/Si substrates.[70] Dielectric constant and loss tangent of ~740 and ~5% (100 Hz) were obtained for such films. According to Guo et al and Lu et al, volatility of the A-site elements (Bi and Na) in this system, strictly limited the evaluation of their electrical properties due to an increased conductivity. [70,73]

$(Na_{0.5}Bi_{0.5})TiO_3$ thin films were also synthesized using magnetron sputtering by Zhou et al. These NBT thin films exhibit a lossy hysteresis loop, in Figure 2.12, with a P_r and E_c of 11.9 $\mu C/cm^2$ and 37.9 kV/cm, respectively. [74] A change in the mechanism of

electrical conduction from the grain interior to the grain boundary was observed with increasing temperature. Hopping of oxygen vacancies was found to be responsible for the dc conductivity, which apparently affects the dielectric and ferroelectric behavior.

Lu et al studied $Bi_{0.5}(Na_{0.7}K_{0.2}Li_{0.1})_{0.5}TiO_3$ (BNKLT) deposited on Pt/Ti/SiO$_2$/Si substrates by PLD. The substrate temperature 600°C and the ambient oxygen pressure 225 mTorr were found to be optimum conditions for the growth of fine, dense and uniform BNKLT films with perovskite structure with a laser energy density of 1.6 J/cm^2. The dielectric properties of the BNKLT films were influenced by the oxygen pressures, with an enhanced dielectric constant of 139 and relatively low loss tangent of 0.054 at 225 mTorr. [73] The polarization-electric field hysteresis loop of such films is shown in Figure 2.13.
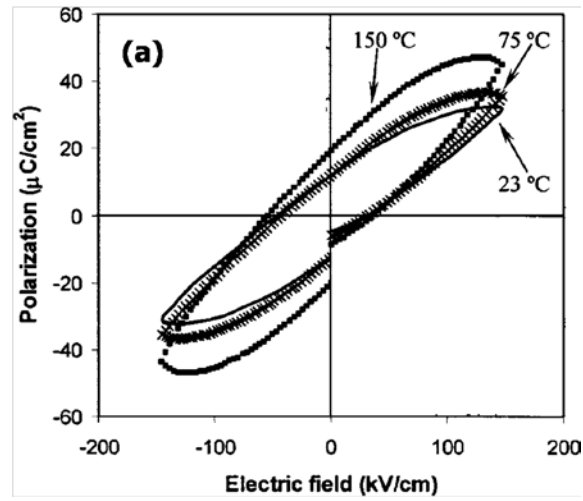
Figure 2.12 (a) Polarization hysteresis loops, for BNT thin films annealed at 700°C, measured at different temperatures
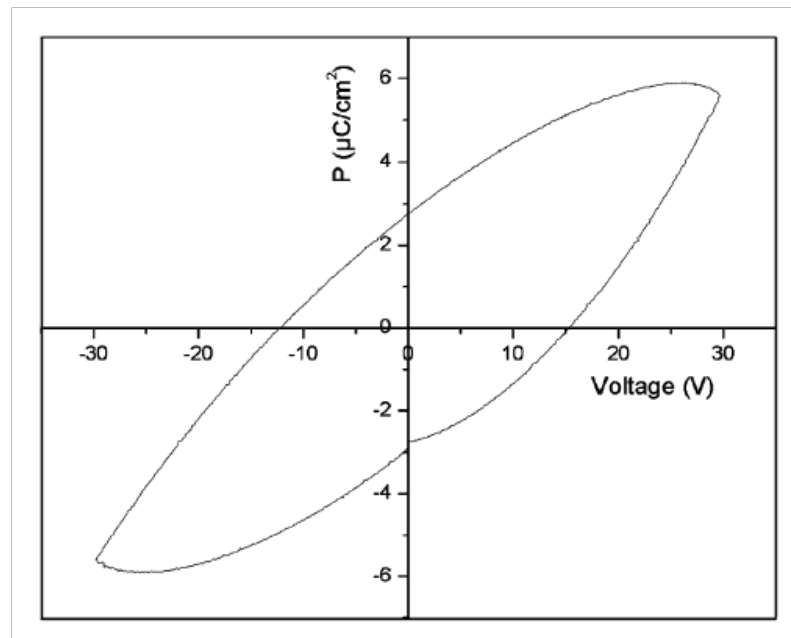
Figure 2.13 P–E loop of BNKLT thin film on Pt/Ti/SiO$_2$/Si substrates

2.5 Summary

In this chapter, the most important ferroelectric/piezoelectric lead-free compositions were introduced and their main properties were discussed. Some of the challenges facing the development of novel lead-free compositions were reviewed and present solutions were described. Among all the current lead-free ceramic compositions, $(K,Na)NbO_3$-$LiTaO_3$-$LiSbO_3$ and $(Bi,Na)TiO_3$-$(Bi,K)TiO_3$-$BaTiO_3$ were shown to have the most remarkable properties and their great potential for improvement and substitution of lead-based counterpart in future environment-friendly devices.

Despite extensive studies on lead-free composition with competitive electrical properties, in the area of thin films, however, the several problems such as the evaporation of volatile species and low resistivity have hindered the development of high quality films for applications such as MEMS devices. Therefore, more attention must be paid to the synthesis, optimization and understanding of the properties of such thin films, in order to obtain high quality thin films to meet future demands of piezoelectric device applications.

References

[1] B. T. Matthias, *Physical Review*, **75**, Issue 11, 1771 (1949).

[2] G. Shirane, R. Newnham, R. Pepinsky, *Phys. Rev.* **96**, 581 (1954).

[3] Y. Saito, H. Takao, T. Tani, T. Nonoyama, K. Takatori, T. Homma, T. Nagaya, and M. Nakamura, *Nature* **123**, 84 (2004).

[4] S. J. Zhang, R. Xia, T. R. Shrout, *J. Am. Ceram. Soc.* **19**, 251 (2007).

[5] E. K. Akdoğan, K. Kerman, M. Abazari, and A. Safari, *Appl. Phys. Lett.* **92**, 112908 (2008).

[6] E. Hollenstein, M. Davis, D. Damjanovic, and N. Setter, *Appl. Phys. Lett.* **87**, 182905 (2005).

[7] Y. Guo, K. -I. Kakimoto, H. Ohsato, *Matt. Lett.* **59,** 241 (2005).

[8] Y. Saito, and H. Takao, *Ferroelectrics* **338**, 17 (2006).

[9] Y. Dai, X. Zhang, and G. Zhou, *Appl. Phys. Lett.* **90**, 262903 (2007).

[10] Y. Wang, D. Damjanovic, N. Klein, E. Hollenstein and N. Setter, *J. Am. Ceram. Soc.*, **90**, 11, 3485 (2007).

[11] Y. Wang, D. Damjanovic, N. Klein, and N. Setter, *J. Am. Ceram. Soc.*, **91**, 6 1962 (2008).

[12] S. Zhang, R. Xia, T. R. Shrout, G. Zang and J. –F. Wang, *J. Appl. Phys.* **100**, 104108 (2006).

[13] Y. Guo, K. -I. Kakimoto, H. Ohsato, *Appl. Phys. Lett.* **85**, 4121 (2004).

[14] K. –I. Kakimoto, K. Akao, Y. Guo and H. Ohsato, *Jpn. J. Appl. Phys.* **44**, 9B, 7064 (2005).

[15] K. Wang, J. –F. Li, and N. Liu, *Appl. Phys. Lett.* **93**, 092904 (2008).

[16] C. Lei and Z. -G. Ye, *Appl. Phys. Lett.* **93**, 042901 (2008).

[17] H. Park, C. Ahn, H. Song, J. Lee, S. Nahma, K. Uchino, H. Lee, H. Lee, *Appl. Phys. Lett.* **89**, 062906 (2006).

[18] H. –Y. Park, K. –H. Cho, D. –S. Paik, S. Nahma, H. –G. Lee D. –H. Kim, *J. Appl. Phys.* **102**, 124101 (2007).

[19] K. H. Cho, H. Y. Park, C. W. Ahn, S. Nahm, K. Uchino, S.H. Park, H. G. Lee, H. J. Lee, *J. Am. Ceram. Soc.* **90**, 1946 (2007).

[20] M. Kim, H. Song, J. Choi, Y. Cho, H. Kim, S. Yoon, *J. Electroceram* (2008).

[21] K. Matsumoto, Y. Hiruma, H. Nagata and T. Takenaka, *Jpn. J. Appl. Phys.* **45**, 5B 4479 (2006).

[22] Y. Watanabe, K. Sumida, S. Yamada, S. Sago, S. Hirano, and K. Kikuta, *Jpn. J. Appl. Phys.* **47**, 5 3556 (2008).

[23] N. M. Hagh, K. Kerman, B. Jadidian, A. Safari, *J. Euro. Ceram. Soc.* **29**, 2325 (2009).

[24] N. M. Hagh, B. Jadidian, E. Ashbahian, A. Safari, *IEEE Trans. Ultrason. Ferro. Freq. Contr.* **55**, 214 (2008).

[25] N. M. Hagh, B. Jadidian, A. Safari, *J. Electroceram.* **18**, 339 (2007).

[26] S. Wada, M. Nitta, N. Kumada, D. Tanaka, M. Furukawa, S. Ohno, C. Moriyoshi, Y. Kuroiwa, *Jpn. J. Appl. Phys.* **47**, 9 7678 (2008).

[27] R. E. Jaeger, L. Egerton, *J. Am. Ceram. Soc.*, **45**, 209 (1962).

[28] R. P. Wang, R. J. Xie, T. Sekiya, Y. Shimojo, *Mat. Res. Bull.* **39**, 11, 1709 (2004)

[29] Y. –H. Lee, J. –H. Cho, B. Kim, and D. Choi, *Jpn. J. Appl. Phys.* **47**, 6, 4620 (2008).

[30] J. Bernard, A. Bencan, T. Rojac, J. Holc, B. Malic, M. Kosec, *J. Am. Ceram. Soc.* **91**, 2409 (2008).

[31] G. A. Smolenski, V. A. Isupov, A. I. Agranovskaya and N. N. Krainik, *Sov. Phys. Solid State* **2**, Issue 11, 2651 (1961).

[32] Y. Hiruma, H. Nagata, T. Takenaka, *J. Appl. Phys.* **105**, 084112 (2009)

[33] A. Sasaki, T. Chiba, Y. Mamiya, E. Otsuki, *Jpn. J. Appl. Phys*. **38** 5564 (1999).

[34] T. Takenaka, K. Maruyama, K. Sakata, *Jpn. J. Appl. Phys.* **30**, 9B 2236 (1991).

[35] D. Lin, D. Xiao, J. Zhu, P. Yu, *Appl. Phys. Lett.* **88**, 062901 (2006).

[36] Y. Hiruma, H. Nagata and T. Takenaka, *Jpn. J. Appl. Phys.* **45**, 9B 7409 (2006).

[37] H. Nagata, M. Yoshida, Y. Makiuchi and T. Takenaka, *Jpn. J. Appl. Phys.* **42**, 7401 (2003).

[38] X. X. Wang, X. G. Tang, and H. L. W. Chan, *Appl. Phys. Lett.,* **85**, 91 (2004).

[39] T. Takenaka, H. Nagata, and Y. Hiruma, Jpn. *J. Appl. Phys*. **47**, 5 3787 (2008).

[40] S. Zhang, A. B. Kounga, E. Aulbach, H. Ehrenberg, J. Rödel, *Appl. Phys. Lett.* **91**, 112906 (2007).

[41] W. Jo, T. Granzow, E. Aulbach, J. Rödel, D. Damjanovic, *J. Appl. Phys.* **105**, 094102 (2009).

[41] T.J. Zhu, L. Lu, M.O. Lai, *Appl. Phys. A* **81**, 701–714 (2005)

[42] I. Y. (Steve) Shen, G. Z. Cao, C. –C. Wu.,C. –C. Lee, *Ferroelectrics* **342**,15–34, (2006)

[43] C.-R. Cho, A. Grishin , *Appl. Phys. Lett.* **75**, 268 (1999).

[44] K. Tanaka, K. Kakimoto, and H. Ohsato, *J. Cryst. Growth* **294,** 209(2006)

[45] T. Saito, H. Adachi, T. Wada, *Jpn. J. Appl. Phys.* **244,** L573-L575 (2005)

[46] K. Tanaka, K. Kakimoto, H. Ohsato, and T. Iijima, *Jpn. J. Appl. Phys.* **46,** 1094(2007)

[47] X. wang, et al, *J. Mat. Res.* **17**, 1183 (2002)

[48] X. Wang, U. Helmersson, S. Olafsson, S. Rudner, L. D.Wernlund and S. Gevorgian, *Appl. Phys. Lett.* **73**, 927 (1998).

[49] T. Saito, T. Wada, H. Adachi and I. Kanno, *Jpn. J. Appl. Phys.* **43**, 6627 (2004).

[50] C. Zaldo, D. S. Grill, R. W. Eason, J. Mendolia, and P.J. Chandler, *Appl. Phys. Lett.* **65**, 502 (1994).

[51] Y. Nakashima, W. Sakamoto, H. Maiwa, T. Shimura, T. Yogo, *Jpn. J. Appl. Phys.*, **46**, No. 14, L311 (2007).

[52] C. W. Ahn, S. Y. Lee, H. J. Lee, A. Ullah, J. S. Bae, E. D. Jeong, J. S. Choi, B. H. Park, I. W. Kim, J. *Phys. D: Appl. Phys.* **42**, 215304 (2009).

[53] C. W. Ahn, E. D. Jeong, S. Y. Lee, H. J. Lee, S. H. Kang, I. W. Kim, *Appl. Phys. Lett.* **93**, 212905 (2008).

[54] F. Lai, J. –F. Li, *Ferroelectrics* **358**, 181 (2007).

[55] F. Lai, J. –F. Li, Z. –X. Zhu, Y. Xu, *J. Appl. Phys.* **106**, 064101 (2009).

[56] K. Tanaka, K. Kakimoto, H. Ohsato, *J. Cryst. Gro.* **294**, 209 (2006).

[57] K. Shibata, F. Oka, A. Ohishi, T. Mishima, and I. Kanno, *Appl. Phys. Exp.* **1**, 011501 (2008).

[58] J. S. Lee, H. J. Lee, J. Y. Lee, S. H. Kang, I. W. Ki, C. W. Ahn, G. S. Chung, *J. Kor. Phys. Soc.* **52**, No. 4, 1109 (2008).

[59] J. Wu, J. Wang, *J. Appl. Phys.* **106**, 066101 (2009).

[60] S. Yamazoe, Y. Miyoshi, K. Komaki, H. Adachi, T. Wada, *Jpn. J. Appl. Phys.* **48**, 09KA13 (2009).

[61] H. Fujita, S. Goto, M. Sakashita, H. Ikeda, A. Sakai, S. Zaima, Y. Yasuda, .Jpn. J. *Appl. Phys. Lett.* **39**, 7035 (2000)

[62] J. Lee, A. Safari, and R. L. Pfeffer, *Appl. Phys. Lett.* **61,** 1643 (1992).

[63] K. S. Grabowski, J. S. Horwitz, D. B. Chrisey, *Ferroelectrics* **116**, 19 (1991)

[64] W. B. Wu, K. H. Wong, C. L. Mak, C. L. Choy, and Y. H. Zhang, *J. Appl. Phys.* **88,** 2068 (2000).

[65] C. Cho and A. Grishin, *J. Appl. Phys.* **87**, 4439 (2000).

[66] T. Saito, H. Adachi, T. Wada, *Jpn. J. Appl. Phys.* **44**, L573 (2005).

[67] T. Yu, K. W. Kwok, H. L. W. Chan, *Mat. Lett.* **61**, 2117 (2007).

[68] T. Yu, K.W. Kwok, H. L. W. Chan, *Thin Solid Films* **515**, 3563 (2007).

[69] X.-G. Tang, J.Wang, X.-X.Wang, H.L.-W. Chan, *Chem. Mater.* **16**, 5293 (2004).

[70] Y. Guo, D. Akai, K. Sawada, M. Ishida, *Sol. St. Sci.* **10**, 928 (2008).

[71] N. Scarisoreanu, M. Dinescu, F. Craciun, P. Verardi, A. Moldovan, A. Purice, C. Galassi, *Appl. Surf. Sci.* **252**, 4553 (2006)

[72] H.-W. Cheng, X.-J. Zhang, S.-T. Zhang, Y. Feng, Y.-F. Chen, Z.-G. Liu, G.-X. Cheng, *Appl. Phys. Lett.* **85**, 2319 (2004).

[73] L. Lu, D. Xiao, D. Lin, Y. Zhang, J. Zhu, *Physica B* **404** 325 (2009).

[74] Z. H. Zhou, J. M. Xue, W. Z. Li, J. Wang, H. Zhu, J. M. Miao, *Appl. Phys. Lett.* **85**, 2, 805 (2004).

3 Research Objectives and Scientific Approach

Since its discovery in 1950's, remarkable dielectric and piezoelectric performance of lead zirconate titanate (PZT) and many other lead-based solid solutions have led to their widespread use in sensors and actuators applications. Thus far, a great deal of research has been conducted on PZT-based compositions to further tune their properties for different applications. Variety of dopants have been studied in PZT solid solution to modify certain characteristics of the material, such as piezoelectric coefficient, coercive field, etc. PZT-based thin films, also, have attracted a good deal of attention to be used in non-volatile ferroelectric memories as well as a functional component in microelectromechanical systems (MEMS). However, PZT as well as other lead-based compositions contain considerable amount of lead whose toxicity was evidenced in the past few decades. Primarily, volatility of lead results in its substantial exposure to the environment during processing steps, such as calcination, sintering, and machining of those compositions. Also, disposal of lead-containing devices has become a secondary challenge regarding their usage all around the world. Therefore, measures are being taken to seriously restrict usage of lead-based materials for many commercial applications in the United States, while Europe and Japan have been the leading nations in this matter, having already abandoned any research funding on such materials. Therefore, there is need to develop and establish novel lead-free piezoelectric compositions whose properties are comparable to those of PZT materials. Two major lead-free compositions, namely $(K,Na)NbO_3$-based and $(Bi,Na)TiO_3$-based solid solutions have been the center of focus for the past few years, although many years of dedicated research and development are required before realization of lead-free devices is possible.

Discovery of high piezoelectric activity in the ternary lead-free KNaNbO$_3$-LiTaO$_3$-LiSbO$_3$ (KNN-LT-LS) and (Bi,Na)TiO$_3$-(Bi,K)TiO$_3$-BaTiO$_3$ (BNT-BKT-BT) systems in the past few years, has revived interest in these compositions as future substitutes for PZT. However, there are significant differences in the processing and electrical performance of bulk materials with those of thin films. Only little effort has been made to produce high quality, reliable thin films with properties competitive to their lead-based counterparts and a detailed study, on the effect of processing parameters on the properties of the lead-free KNN-LT-LS and BNT-BKT-BT thin films has not been presented. Also lead-free compositions such as KNN-LT-LS exhibit a low resistivity, due to existence of a large defects concentration, which is originated from evaporation of volatile species, e.g. K and Na. Various dopants have been attempted to reduce the conductivity of KNN-based ceramics, such as Cu and Ba. The conductivity issue is even more significant in the thin films, due to the more likely chemical deviations from the stoichiometry. Another major issue in the performance of lead-free piezoelectric components, especially KNN-LT-LS, in functional devices is the temperature dependence of their electrical properties. This is in part due to the existence of phase transitions in the phase diagram, which could not be avoided. However, this is not desirable from the device realization standpoint and a temperature stability region has to be attained whose range is application specific. As BNT-BKT-BT and KNN-LT-LS ceramics have their distinct differences, diverse applications may be proposed for each of them, considering their ferroelectric and piezoelectric behavior and more importantly temperature stability range. Consequently, lead-free thin films based on these two systems may be utilized according to their specific characteristics, such as piezoelectric coefficient, remanent polarization or leakage and

breakdown behavior. Therefore, a comparison study is needed to recognize their individual strength and distinctions.

Thus, the main motivations for this study can be described as follows:

1.   The primary objective of this thesis is to understand the effect of the deposition parameters on the perovskite phase formation of $(K_{0.44}Na_{0.52}Li_{0.04})(Nb_{0.84}Ta_{0.1}Sb_{0.06})O_3$ (KNN-LT-LS) thin films prepared by pulsed laser deposition (PLD). These processing parameters included mainly substrate temperature and oxygen partial pressure, substrate type and laser energy density. The KrF laser with $\lambda = 248$ nm was used in this study. To optimize the deposition conditions, effect of one variable will be investigated at a time, since the optimum condition for one parameter may change the optimum condition of other parameters. Single-phase formation, crystallinity, epitaxial growth, chemical composition, microstructure and surface morphology, dielectric and ferroelectric properties of the films will be studied as a function of the deposition parameters and a detailed explanation will be provided for the observed correlation between each of the deposition parameters and the final properties.

2.   Effects of several donor and acceptor dopants in the KNN-LT-LS composition will be investigated to enhance the resistivity and resultant electrical properties of such thin films. These films are to be deposited at the optimized processing conditions following the first part of the study.

3.   From the perspective of development of future lead-free piezoelectric devices, it is essential to understand domain structure and piezoelectric properties of the thin films. Capability of such films for piezoelectric MEMS devices will be examined and

experimental results as well as the technique exploited for the piezoelectric measurements will be presented.

4.   Dielectric constant and leakage current behavior of the KNN-LT-LS thin films will be studied as a function of temperature to investigate the stability of the properties and gain more knowledge in the transport phenomena in the films.

5.   Preliminary studies on the electrical properties of MPB composition $0.88(Bi_{0.5}Na_{0.5})TiO_3$-$0.08(Bi_{0.5}K_{0.5})TiO_3$-$0.04BaTiO_3$ (BNT-BKT-BT) thin films will be presented and the results are contrasted with those of KNN-LT-LS and PZT thin films.

4 Experimental set up and procedures

4.1 Introduction

In this chapter, a detailed description of the experimental techniques and procedures for preparation of ceramic PLD target, film deposition and structural characterization of lead-free KNN-LT-LS and BNT-BKT-BT thin films is first provided. Second section of the chapter deals with measurement techniques used for structural and compositional analyses of thin films which are necessary for understanding and interpretation of the material's behavior. The third section is involved with measurement setup for the electrical properties of thin films, including dielectric, ferroelectric properties and electromechanical performance of KNN-LT-LS and BNT-BKT-BT thin films.

4.2 Laser Ablation Deposition of thin films

4.2.1   Target preparation

The process of PLD target preparation is similar to bulk synthesis of the ferroelectric composition. The quality of the target with respect to level of impurities, density and phase homogeneity is undoubtedly reflected in the thin film's structure and properties. In case of KNN-LT-LS and BNT-BKT-BT systems, previous studies have shown that the purity of the precursor materials, the processing environment and sintering atmosphere play important roles in the densification of the pellets and hence the bulk properties.[1]

Powder Processing (Mixed-oxide Route):

In mixed-oxide route, the two lead-free compositions, $(K_{0.44},Na_{0.52},Li_{0.04})(Nb_{0.84},Ta_{0.1},Sb_{0.06})O_3$ (KNN-LT-LS) and $0.88[(Bi_{0.5}Na_{0.5})TiO_3]$-$0.08[(Bi_{0.5}K_{0.5})TiO_3]$-$0.04BaTiO_3$ (BNT-BKT-BT) were prepared by using the oxide/carbonate raw materials.

1. Precursor powders (K_2CO_3 (99.99%, Alfa Aesar), Na_2CO_3 (99.95%, Alfa Aesar), Nb_2O_5 (99.9%, Alfa Aesar), Li_2CO_3 (99.99%, Alfa Aesar), Ta_2O_5 (99.99%, Alfa Aesar), Sb_2O_5 (99.99%, Alfa Aesar), for KNN-LT-LS and Bi_2O_3 (99.9%, Aldrich), K_2CO_3 (99.99%, Alfa Aesar), $BaCO_3$ (99.9%, Aldrich), Na_2CO_3 (99.95%, Alfa Aesar), and TiO_2 (99.5%, Aldrich), for BNT-BKT-BT) were dried in oven at 120^oC over night to remove any possible absorbed moisture.

2. Appropriate molar ratios of precursors were manually mixed and subsequent milling was carried out in dry Acetone for 12 hours. Table 4.1 and Table 4.2 shows the weight percent of precursors with purity level for a typical 100gr batch for mixed oxide route.

3. The mixture was then dried over night at 120^oC in an oven and calcined at 800^oC for 5 hours.

4. The batch was ball milled for 12 hours to grind and reduce the particle size to improve the pressing.

5. The batch was manually sieved through 150mm sieve.

Dry-pressing

1. A 1.33 inch diameter, D2 tool-steel die was sprayed with dry film lubricant, and filled with 15 g of the calcined powder. No binder was added to the powder to avoid additional heat-treatment.

2.   The die was loaded to 2,000 psi and released to help eliminate trapped air.

3.   The pellet was then pressed to 12,000 psi to achieve sufficient green density, while not casing delamination, capping, or ring cracks.

Sintering and Densification

4. The pressed pellets were sintered (one at a time) on top of a porous ZrO_2 setter in tube furnace with oxygen flowing at a rate of 18 cm^3/minute. The heating rate was 5^oC/min up to 1150^oC for 1 hour (2 hours in case of BNT-BKT-BT) and cooled at 5^oC/min to room temperature.

5. The sintered density of the target was determined geometrically and plays an important role in the quality of the grown films. Low density results in the fracture of the target or the expulsion of particulates or nanocrystallites that can influence the crystallization of the thin films. Secondary orientations or even polycrystalline films can result if the particulates contaminate the epitaxial film surface.

Table 4.1 Weight of precursor materials in a 100 gram batch of KNN-LT-LS

Composition	KNN-LT-LS
Precursor	Weight(g)
K_2CO_3	16.81
Na_2CO_3	15.23
Li_2CO_3	0.817
Nb_2O_5	61.72
Ta_2O_5	12.22
Sb_2O_5	5.37
1mol% MnO_2	0.483
1mol% $BaCO_3$	0.96
1mol% TiO_2	0.444

Table 4.2 Weight of precursor materials in a 100 gram batch of BNT-BKT-BT

Composition	BNT-BKT-BT
Precursor	Weight(g)
K_2CO_3	1.3
Na_2CO_3	10.93
TiO_2	37.445
$BaTiO_3$	3.699
Bi_2O_3	52.4

4.2.2　　　Thin Film Deposition Procedure

After appropriately mounting the substrate on the heater block, using the silver paint (Ted Pella Inc.), the temperature of the heater was increased to the deposition temperature and meanwhile the chamber was pumped down to a pressure of $\sim 5 \times 10^{-6}$ Torr to improve the desorption of water vapor and other contaminations entered from all surfaces inside the chamber. The completer procedure for film deposition is detailed as the following:[2]

I. Preparation of the instruments

1. Laser chiller, Laser and the two mechanical pumps were first turned on and warmed up for a few minutes. The mechanical pumps were turned on one at a time to prevent the current overflow and fuse break. The chiller was kept on when the laser and/or turbo pump are running and the water pressure must not exceed 25 psi.

2. Heater flange was removed by removing the bolts and increasing pressure inside the chamber to push the flange outward.

II. Substrate preparation and installation

3. Two small beakers and a pair of tweezers were cleaned using methanol.

4. Substrates were removed from packaging using Teflon tweezers and placed in acetone for 1-2 minutes. The substrate was rinsed in acetone and methanol and then placed in methanol.

5. While the substrate was soaked in methanol, the chamber is vented with oxygen (set pressure at 10 psi) through the backfill valve with the shutter closed on the substrate

heater before removing the heater flange from the chamber. Heater was then removed and immediately replaced with the blank flange.

6. The substrate is then rinsed with methanol, then de-ionized water and blowed clean with compressed air/nitrogen.

7. Silver paint was applied as a small drop on the heater block. Substrate is placed carefully on the drop of paint and allowed to flow to the edges.

8. Silver paint was dried by turning on the heater and running to $150^{o}C$, which could be part of the heating up procedure to the final deposition temperature. The heater was shut off and allowed to cool to $125^{o}C$, while the heater flange was placed back into the chamber.

III. Base Pressure Pump-down

9. The right angle valve to pump #2 was opened (roughing pump directly connected to chamber) to begin the pump-down sequence and shutter was raised.

10. The heater is started again to run to deposition temperature while the roughing pump was evacuating the chamber.

11. At approximately 50 mTorr oxygen was bled into the system to flush out contaminants. This was repeated several times to ensure a better and faster pump-down.

12. The right angle valve to pump #1 was then opened to rough out the turbo-pump while the heater was reaching the desired temperature.

13. Once the pressure on Convectron gauge was below 20 mTorr, the turbo-pump is started.

14. The right angle valve to pump #2 was closed, and the gate valve was opened to switch to the high vacuum turbo-pump.

15. The system was then allowed to pump-down for 1.5 hours at minimum, or until the pressure was in the range: 5-8 x 10^{-6} Torr.

IV. Oxygen Pre-anneal

16. The switch on the MKS oxygen controller was turned to AUTO and the gate valve was immediately closed. The right angle valve to pump #2 was then turned two turns using the screw on the handle to judge to stabilize at the desired pressure. The turbo-pump was shut off and the right angle valve to pump #1 was closed to isolate the turbo. Turbo-pump was vented by attaching the plastic tube to nitrogen cylinder to let the nitrogen into the turbo-pump for 10 seconds.

17. The pressure on MKS controller was readjusted to the desired valve, and the substrate was allowed to equilibrate and burn off organic residue for a minimum of 1 hour before film deposition.

V. Film Deposition

18. The laser was first started to allow the pulse energy to stabilize. Using the laser power meter in front of the beam, the power output was then measured for a 40 second trend to ensure the stability of the output.

19. Lens assembly and laser port were uncovered and the shutter on the heater was closed. Target was selected and target rotation was started.

20. The beam stop was then opened to begin the film deposition for the predetermined time.

21. After deposition for the desired time, the laser was stopped using first the beam stop and then the keypad to stop the deposition.

22. The right angle valve to pump #2 was closed, the switch on the MKS controller was turned to CLOSE, and target rotation was stopped.

VI. Post-deposition anneal

23. The heater was shut off the heater or allowed to continue with the cool down/annealing program.

24. The chamber was filled the chamber with 1 atm oxygen at the start of the annealing segment.

25. After the annealing procedure heater was automatically switched off and reset.

VII. Cooling and Shut-down

26. All equipments were shut down if not continuing with another film/layer (Convectron and turbo-pump controller). Films were grown by this technique, with variation in deposition time to control film thickness.

4.2.3   Deposition of bottom electrode

For bottom electrode layer deposition, a commercial $SrRuO_3$ (SRO) target was purchased and used. (Super Conductor Materials Inc., Suffern, NY) SRO layer was deposited prior to deposition of ferroelectric film so as to serve as the bottom electrode. Deposition of the SRO was followed in the same manner as described in film deposition in the previous section. The deposition parameters are summarized in Table 4.3. In order to access the bottom electrode, following the deposition of SRO layer, the chamber was opened and a small glass piece was used to mask an area of the SRO coated substrate, which was later used to contact SRO. Piezoelectric film was then deposited in the same fashion as described in previous section, starting with base pressure pump-down.

Table 4.3 Deposition parameters for $SrRuO_3$ bottom electrode

Deposition temperature (^{o}C)	**800**
Oxygen pressure (mTorr)	**150**
Laser energy density (J/cm^2)	**2**
Laser repetition rate (Hz)	**5**
Duration/thickness (minutes/nm)	**60/150**
Post-annealing temperature (^{o}C)	**650**
Post-annealing duration (min)	**60**

4.2.4   Deposition of top electrode

Prior to deposition of top electrodes, the surface of the deposited was cleaned using nitrogen/air, upon removal of the sample from the PLD chamber. Platinum/gold top electrodes were deposited using DC sputtering technique (Blazers Inc. Amherst, NY) at room temperature. Electrodes were patterned using a shadow mask (Stencils Unlimited Inc., Lake Oswego, OR) with circular patterns of 200μm diameter mounted on top of the sample. The chamber was first evacuated for 20 minutes or once the pressure inside the chamber reaches 10^{-5} Torr. Then Argon was allowed to flow in the chamber keeping with the pressure at 5 x 10^{-5} Torr. High voltage was then increased to 200V while the current was raised to 35-45 mA. The deposition was performed for 4 minutes once the voltage and current stabilizes. A post-deposition annealing was mostly recommended at 450°C for 30 minutes following the deposition to ensure a good contact between the film and electrode.

4.3 Structural and compositional characterization

4.3.1   X-ray Diffraction

Qualitative X-ray phase analysis with Cu-K_{α} radiation was used to examine the phases present in the heterostructure by a Philips X'pert MRD high-resolution diffractometer. The x-ray diffraction technique involves detecting the diffracted beam by planes of atoms in the crystalline lattice, satisfying the Bargg's equation:[3]

$$\lambda = 2d \sin \theta \qquad (1)$$

Cu source was used for the x-ray incident beam in conjunction with an asymmetric monochromator optics consisted of single crystal germanium in asymmetric

configuration. The asymmetric monochromator results in a beam of 17 arc seconds angular divergence, but still allow for a reasonable intensity through. In order to reduce the sources of error in the diffraction pattern due to the sample/beam mis-alignment, a standard procedure must be followed to eliminate any such errors:

I.   θ-2θ scans

The regular θ-2θ diffraction patterns were collected using computer controlled software MDI operated at 45 kV and 40 mA. The scan was performed at continuous mode in the range of 10 to 70° with the step size of 0.01^o and dwell time of 2 seconds at each step. Figure 4.1(a) shows the schematic of diffraction used for θ-2θ scans. The collected data was then plotted and analyzed using the MDI JADE software.

II.   Φ scans

If a sample has a crystallographic texture, the θ-2θ diffraction pattern appears with more intense peaks belonging to the specific family of planes corresponding to the texture direction. While this preferred orientation in the films can be detected in the regular θ-2θ scans, ϕ scans must be carried out to analyze the in-plane texture of the film. In polycrystalline samples with a preferred orientation direction, multiple in-plane orientations are detected in the ϕ scan. However, in case of an epitaxial film, single orientation is expected. Figure 4.1(b) shows the schematic diagram of ϕ scan. First the sample was tilted by $\alpha=45^o$ along ψ axis. Then the 2θ angle is fixed at the angle corresponding to a peak, other than the preferred orientation direction to detect the diffracted beam from that plane. The scan oss then performed with a step size of 0.05^o for 360°. The collected pattern versus the ϕ angle provides a measure of the distribution of grains alignment parallel to the substrate surface.
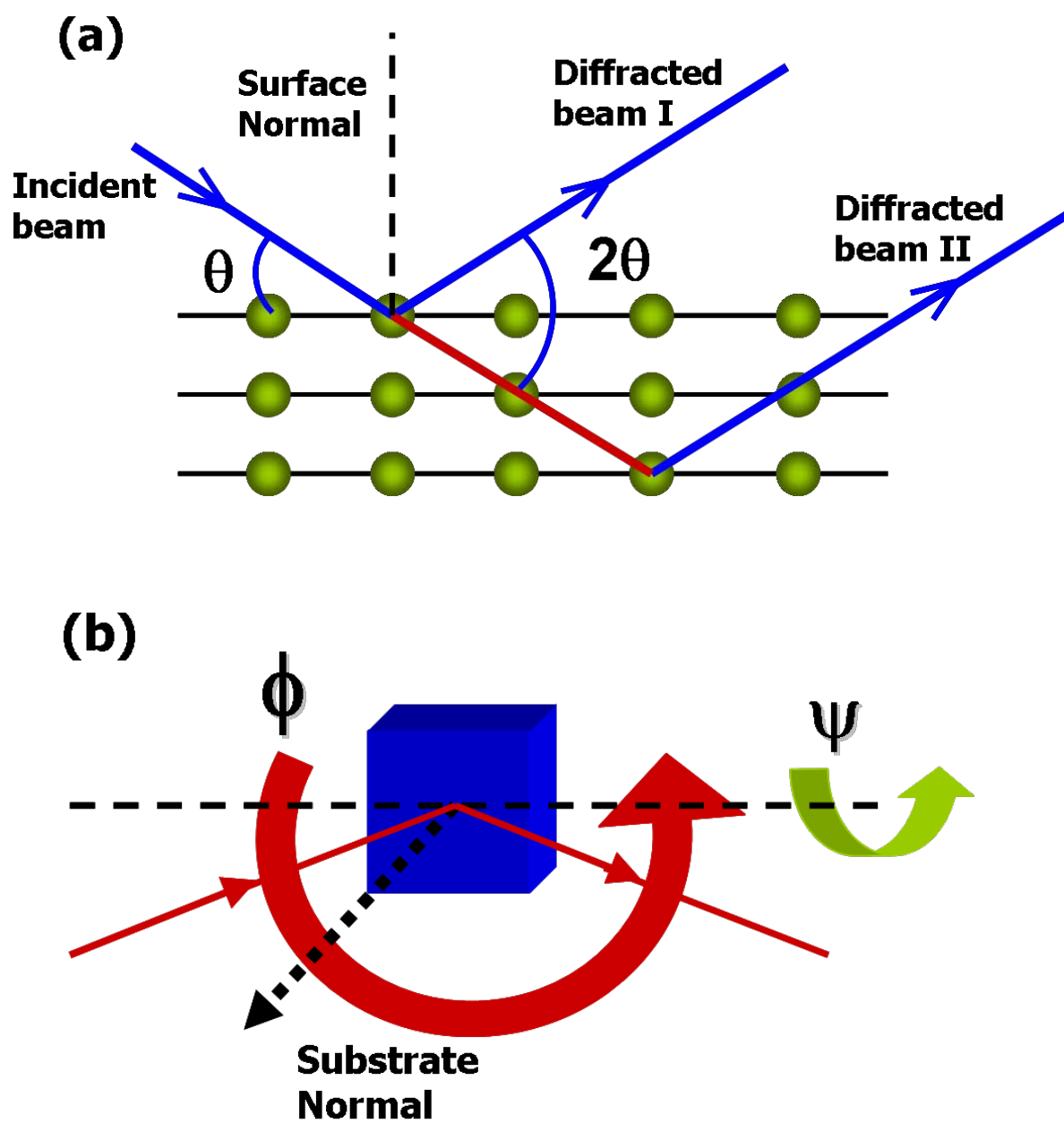
Figure 4.1 X-ray diffraction, (a) basic principles, and (b) instrument schematic and axes rotations

4.3.2 Surface morphology and microstructural analysis

Microstructural evolution and surface morphologies were studied using a Field Emission Scanning Electron Microscopy (Leo Zeiss 982) operated at 5 kV on as-deposited (non-coated) surface of the sample. The samples were cut in half after the deposition and the fresh cross section was used for cross sectional SEM images.

4.3.3 Piezoresponse measurements

Piezoresponse force microscopy (PFM) is a powerful scanning probe microscopy (SPM) technique to study ferroelectric domain structures due to its high resolution and capability of domain switching observation. For the domain structure observation, using PFM, a conductive AFM tip is brought into contact with the sample surface, i.e. contact mode AFM. An AC bias is then applied between the tip and the sample bottom electrode, resulting in a local piezoresponse from the sample. Domains are then visualized by monitoring the first harmonic of the tip deflection signal, whose amplitude is proportional to the local longitudinal piezoelectric coefficient d_{33} and phase reflecting the polarization direction. Piezoresponse (PR) imaging was carried out utilizing a MultiMode series AFM with a Digital Instruments Nanoscope IIIA controller equipped with conductive tips (Pt/Ir coated silicon) to serve as top electrode. The force constant of the tips was 10N/m and the resonance frequency of the cantilever was approximately 204-497 kHz. The operating procedure for domain imaging using AFM is described in the following.

First, the system was engaged on the surface with the tip brought down to the surface. Obtaining a good topographical image is necessary in order to reveal an area with the least surface roughness, thus minimizing damage to the sample or the tip. All of the

parameters required for the PR imaging can be accessed via "Feedback" or "Scan" panel. **[4]** The deflection signal was set as the input to the lock-in amplifier identified as the "PR lock-in" in the feedback panel, shown in Figure 4.2.

The parameters typically used for topography imaging are: scan size, X/Y offsets, scan angle, scan rate and number of samples. For the tip engagement at the start, scan size must be set to a small area, such as 100nm. The size can then be further increased to an area of interest. For domain imaging study in this thesis, the oscillation frequency was set at 17 kHz, while the oscillation amplitude was kept at 1.5 V.

For domain writing, a DC bias was applied to the tip which was grounded in imaging mode. DC voltages must be above the coercive field to ensure switching the domains. Once DC bias was connected to the tip, it could be engaged and the scan could be carried out in a similar fashion to imaging. Upon scanning the area of interest, DC bias was removed and the scanned area was imaged immediately afterwards. The magnitude of the DC bias can be increased up to 10 V and depends on the sample specifications, e.g. coercive field, beak down voltage, etc.

Three different types of data is collected using PR mode imaging: amplitude, phase, and hybrid response. "Amplitude" data is always positive and yields information about the magnitude of the polarization of the sample at the AC driving frequency. "Phase" can be positive or negative, and shows the direction of the polarization of the sample at the driving frequency. A hybrid data combines amplitude and phase data, i.e. magnitude multiplied by the sign of the phase, and therefore contains information on both magnitude and direction of the polarization.
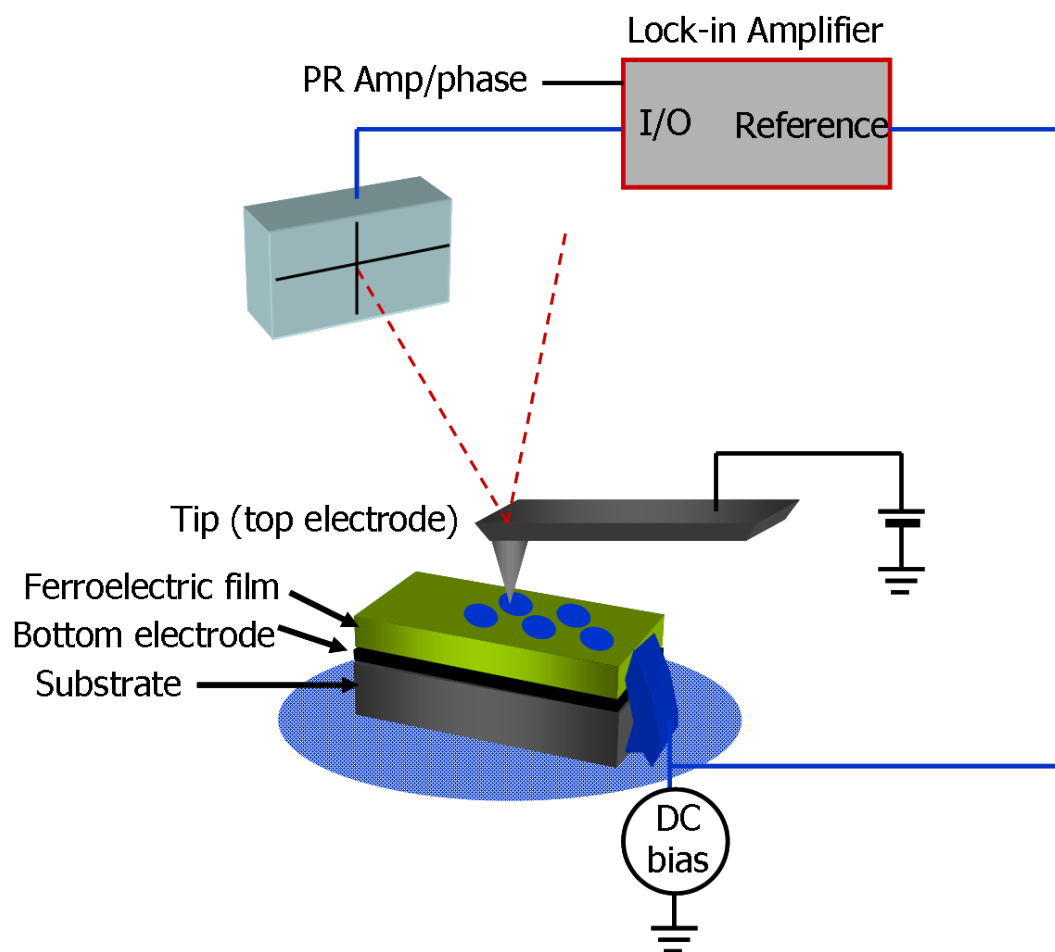
Figure 4.2 Experimental setup for Piezoresponse Force Microscopy

4.3.4   Rutherford Backscattering Spectroscopy for compositional analysis

Rutherford Backscattering Spectroscopy (RBS) technique is commonly used for the elemental analysis of thin films. Various parameters can be determined using RBS, such as thickness, composition profile and depth distribution of elements which specifically helpful in case of interdiffusion of the elements in the substrate and quality of the interface. One of the significant advantages of this technique lies in the fact that the quantitative analysis of the composition does not require a standard sample. Typically RBS is capable of determining the thickness of the films from a hundred up to several thousands of angstroms. A basic RBS instrument generally includes three main components:[5]

1. An ion Source (usu. He^+)

2. Linear particle accelerator, capable of accelerating incident ions to high energies, usually in the range 2-4 MeV.

3. A detector capable of measuring the energy of backscattered particles.

The basic principle of this technique is to apply a monoenergetic beam of light ions, which is usually He with energy in a range of 2-4 MeV to impinge on the sample. The technique employs the elastic collision between a high kinetic energy particle from the incident beam (He^+ ion source) and a stationary particle (atoms) located in the sample. Elastic in this context means that no energy is either lost or gained during the collision. High energetic ions, therefore, can penetrate few microns below the surface of the sample before they elastically scattered off an atom. These backscattered particles which escape the sample are detected and analyzed based on their energy.
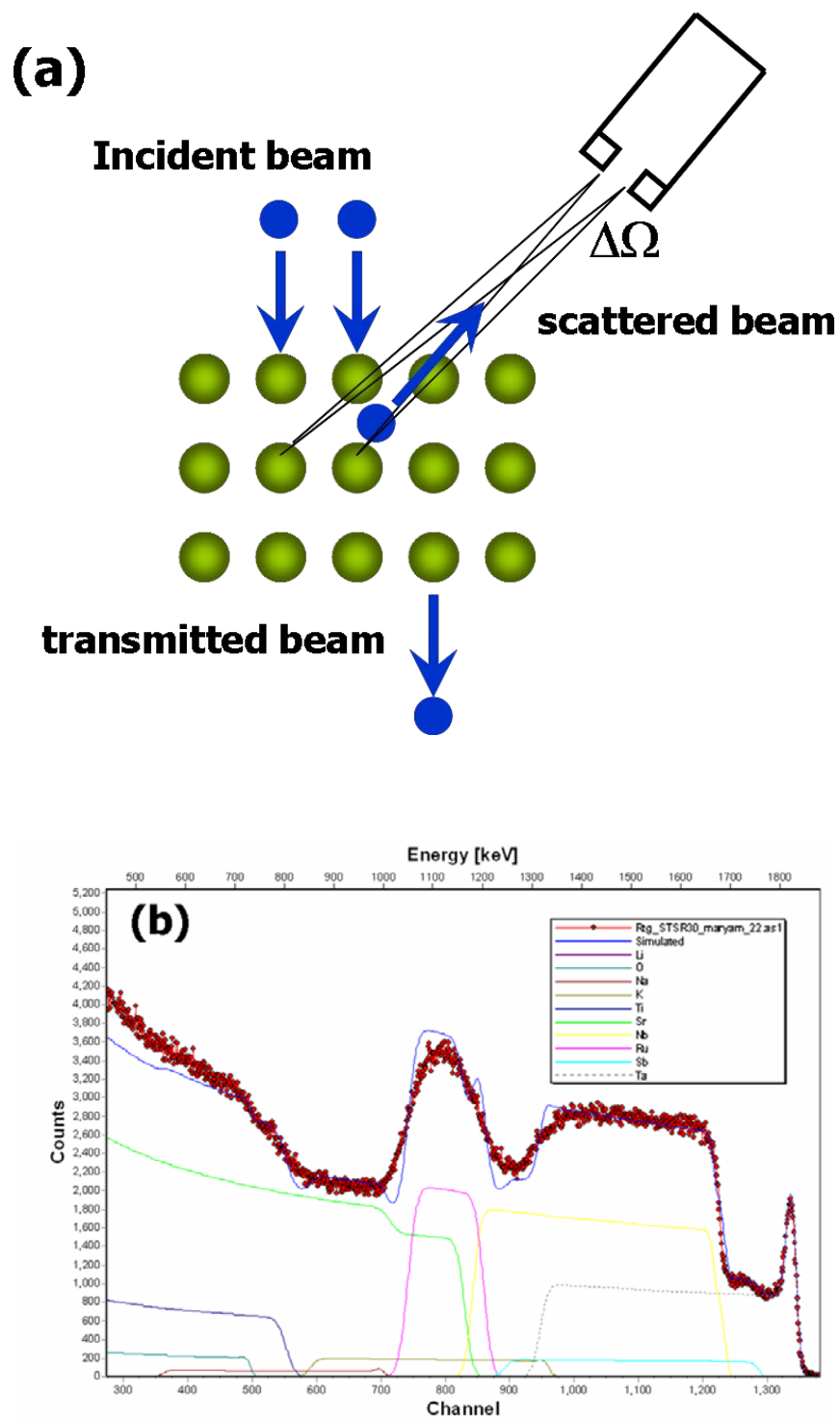
Figure 4.3 Rutherford Backscattering Spectroscopy (RBS), (a) basic principles and (b) data collection and simulation in SIMNRA

A compositional depth profile can be determined from an RBS measurement. The elements contained by a sample can be determined from the positions of peaks in the energy spectrum. Depth can be determined from the width and shifted position of these peaks, and relative concentration from the peak heights. This is especially useful for the analysis of a multilayer sample, or for a sample with a composition which varies more continuously with depth. Figure 4.3 shows a schematic diagram of the RBS principles and instrumentation. The chemical compositions of the films grown on silicon substrate were examined by RBS, with a 2 MeV He^+ probe. The composition of the films was then analyzed by the SIMNRA 6.0 software package, developed by Dr. Matej Mayer in Max-Planck-Institut fur plasmaphysik.

4.3.5 Energy Dispersive X-ray Spectroscopy for chemical analysis

Chemical composition of the deposited films was analyzed using Energy Dispersive Spectroscopy (EDS). EDS is the one of the most common techniques for elemental analysis of thin film samples. However, the accuracy of the technique can be affected by different parameters, mainly the thickness of the sample and nonuniformity of the composition. For EDS measurements, the electron beam was scanned on an area of 100 x 100 μm operating at 10 kV. The scan was repeated at 3-5 different locations on the sample surface. The x-ray signal generated from the area was collected for 300 seconds at a quant mode using IMIX software.

4.4 Electrical properties

4.4.1 Dielectric properties

The relative permittivity (K_{33}) and the dissipation factor ($\tan\delta$) of the films were measured in the 1-1000 kHz frequency range. The measurements were performed at a zero bias field and 50mV oscillation level. The dielectric constant was then calculated from the measured capacitance using the formula $\varepsilon_r = Cd/(A\varepsilon_0)$. Here A is the area of the top electrode and d is the thickness of the ferroelectric layer in parallel-plate capacitor configuratuion, shown in Figure 4.4 (a). Capacitance of the films was also measured using two top electrodes, shown in Figure 4.4 (b), which are connected via the grounded SRO bottom electrode, forming two capacitors in series. Dielectric constant could then be measured using the formula $\varepsilon_r = 2Cd/(A\varepsilon_0)$, where factor 2 is considered for the series capacitor configuration. It should be noted that the distance between two Pt/Au circular top electrodes is 2mm, which is an order of magnitude larger than the diameter of the electrodes. Hence the fringe field effect can be neglected. No significant difference was observed in the dielectric constant values measured from the two presented methods.
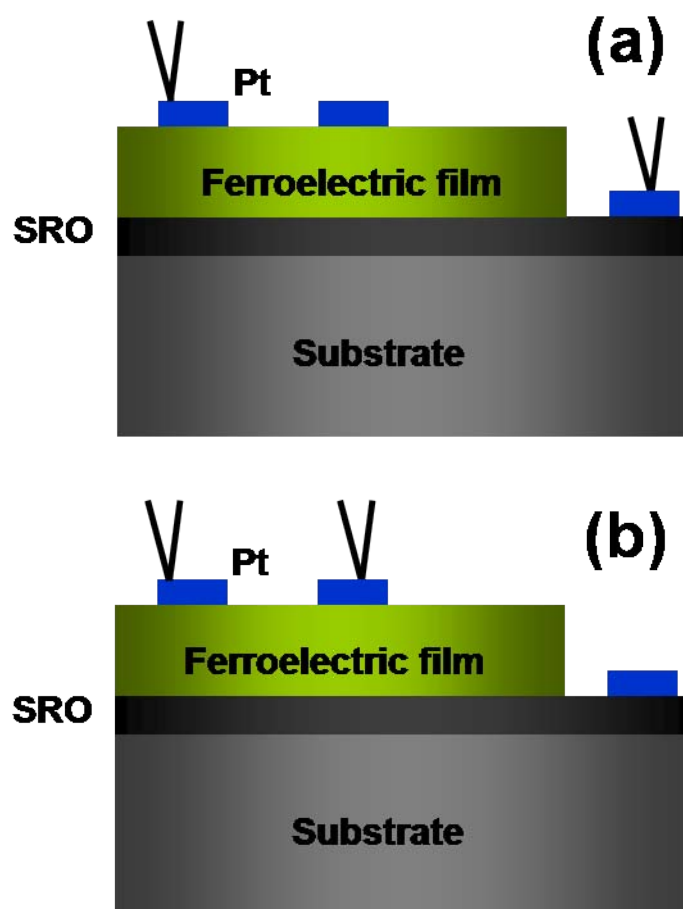
Figure 4.4 Experimental setup for electrical measurements, (a) parallel-plate capacitor configuration, and (b) two-top electrode configuration

In order to measure the temperature dependence of the dielectric constant at temperatures above room temeprature, the sample was glued to an alumina substrate with silver paste, and was subsequently heated for 10 minutes at 120°C. Gold micro-wires were then carefully bonded to the patterned electrodes on the sample on one side and steel wires on the other side, using small amount of silver paint. Steel wires were connected to the HP4194A using the HP 1 m fixture for capacitance measurements. The alumina substrate was inserted in a tube furnace and heated to 450°C with 5°C/min ramp rate. The capacitance measurements were reported on the cooling down ramp. For low temperature measurements, the sample was first placed on the sample stage using thermal conductive glue. The chamber was then evacuated and once the vacuum has reached, the stage was cooled down using liquid nitrogen. The current measurements were carried out using a semiconductor parameter analyzer, Agilent hp4140b. The details of the low temperature set up were described by Eda **[6]**.

4.4.2   **Polarization Hysteresis measurements**

Ferroelectric hysteresis loops are measured using Precision LC 10V, Radiant Technologies. A virtual tester called Vision operates Radiant's tester hardware. The test configuration is the same as dielectric measurements. Vision can construct complex programs with any number of tests to characterize all aspects of the sample in one execution while keeping track of the measurement results and the history of the sample being tested. The Precision LC has the following specification and capabilities:

- Min charge sensitivity of 30.5 fC
- Min capacitor area of 3.05 μm^2

- Max charge measurement of 5.8 mC

- Max hysteresis loop frequency of 2 kHz

- Min hysteresis loop frequency of 0.1 Hz

The P/E loops of lead-free thin films in this study are measured at a pulse width of 1-10 msec (100 Hz-1 kHz) using a triangular wave signal, shown in Figure 4.4. Also, for the low temperature hysteresis measurements, the Precision LC is connected to a Quantum Design PPMS system which is capable of cooling down to 4 K (below room temperature).

4.4.3   Leakage current study

Precision LC is capable of performing I/V curves without changing the test configuration. I/V curves in this study were measured at various temperatures. The radiant system was connected to a probe station with an on-stage heater block. The temperature of the stage can be varied from 70 K to 400 K. The measurement is carried out once the temperature fluctuation was below 2-3%.

4.5 Electromechanical properties

4.5.1   Longitudinal piezoelectric coefficient (d_{33}) measurements

For d_{33} measurements, sample setup was the same as described for the PFM measurement. Upon finding a reasonably smooth area, the scan size was set to 0 nm in order to keep the tip at the point of interest. A LabVIEW program (National Instruments Inc.) was then utilized to control the measurement, as demonstrated in Figure 4.5(a). The

controlling parameters were set as follows, according to previous works **[7]** to ensure an accurate response:

- DC bias = 7V (well above the coercive field to ensure switching)

- Oscillation amplitude = 1-2 V (below coercive field)

- Oscillation frequency (ω) = 17 kHz

- Time constant = 300 ms-1 sec

- Number of data points (N) = 70

The displacement of the tip under the dc bias field was then measured and d_{33} was derived according to the following formulation, thereby:

$$d_{33} = \pm\Delta Z(t)/V\sin(\omega t) \qquad\qquad (2)$$

where $\Delta Z(t)$ is longitudinal displacement of the film under the tip.**[7]**

In order to translate the AFM tip deflection signal in the "*SPM*" mode into assessable values of electromechanical (d_{ij}) coefficients, the deflection of the AFM cantilever must be described quantitatively. For this purpose, the cantilever deflection signal must be calibrated using a standard sample, such as single crystal X-cut quartz. The X-cut quartz relevant coefficient, d_{11} is known to be -2.3 pm/V. It is important to note that the calibration of the tip deflection must be performed at the same level of absolute deflection of the cantilever. For the calibration experiment, a 0.2 mm thick x-cut quartz single crystal was electroded with gold on both sides. Wire bonding was used for the top electrode contact, while for bottom electrode silver paste was used to glue the sample to a sample disc. The AFM tip was held at the same potential as the top electrode. The tip vibration amplitude signal is then plotted against the AC applied voltage. The slope of the

curve gives the conversion constant between the voltage signal of the photodiode and the piezoelectric-induced deflection of the tip. Electromechanical coefficient, d_{33}, were then calculated as below:

$$d_{33} = \frac{\text{Lock-in reading (comp. units)} \times d_{11,quartz}}{\text{Slope} \times V_{AC, \text{ used to acquire the } d_{33} \text{ loop}}} \qquad (3)$$

From Figure 4.5(b), the slope of the plot was found to be 0.10518 pm/V. The V_{AC} in the above equations is associated with the rms value of the applied ac voltage.
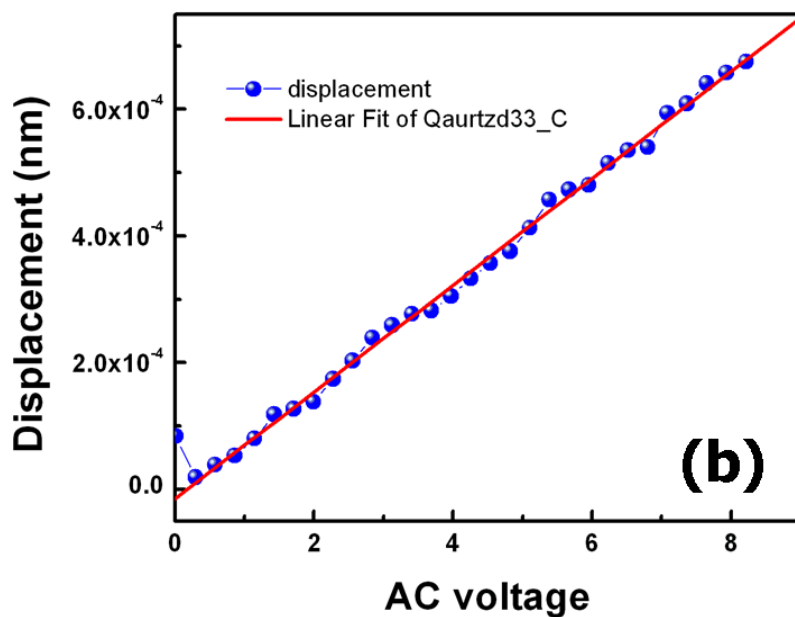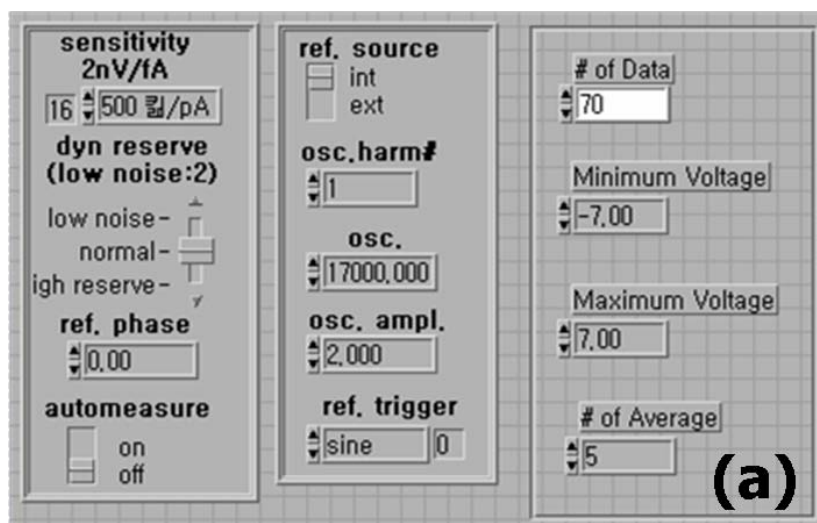
Figure 4.5(a) d_{33} measurements control parameters, and (b) tip deflection calibration using quartz displacement

4.5.2   Transverse piezoelectric coefficient ($e_{31,f}$) measurements

The in-plane thin film piezoelectric coefficients were measured using a wafer flexture method as described in the following. It is important to note that a limitation to wafer flexture technique was that the knowledge of the elastic constants was required for the calculations of d_{31} coefficients according to the following equations:

$$D_3 = d_{31}T_1 + d_{31}T_2 + d_{33}T_3 + \varepsilon_{33}^T E_3 \qquad (4)$$

$$D_3 = d_{31}\frac{S_1 + S_2}{(s_{11}^E + s_{12}^E)} \qquad (5)$$

where D_3 is the dielectric displacement in the out-of-plane direction, T_j is the applied stress in the reduced notation, S_i is the mechanical strain and s_{ij} denotes the mechanical compliance matrix. In order to avoid uncertainty in the film's elastic constants, e_{31} values are preferable and used to study the transverse piezoelectric performance of the films. The relationship between e_{31} and d_{31} coefficients is described as the following:[8]

$$d_{31} = e_{31}(s_{11}^E + s_{12}^E) + e_{33}s_{13}^E \qquad (6)$$

$$e_{31,f} = \frac{d_{31}}{s_{11}^E + s_{12}^E} = e_{31} + e_{33}\frac{s_{13}^E}{s_{11}^E + s_{12}^E} \qquad (7)$$

According to the above equations, considering $S_1 = S_2$ in biaxial strain conditions, therefore:

$$D_3 = 2S_1 \times e_{31,f} \qquad (8)$$

In wafer-flexure method, a cavity to which a silicon wafer is sealed was pressurized using an audio speaker, driven by 0.5V at 4 Hz. A lock-in amplifier (Stanford Research

Inc. SR-830) was connected to the sample which measured the generated piezoelectric charge in current integration mode during the application of pressure to the cavity/silicon. The measured charge allows calculation of the stress-induced polarization. In order to rely on the stress transfer from silicon wafer to the substrate and subsequently the film, it was necessary that the substrate be bonded to the silicon wafer using a cyanocrylate adhesive to achieve a biaxial strain on the film's surface. Schematic of the measurement setup is illustrated in Figure 4.6. The strain associated with the films were measured using a strain-gauge (Omega Inc.) attached to the sample during measurement. The output of the strain gauge was sent to the lock-in amplifier that drove the audio speaker and an rms value for the strain was obtained thereby. $e_{31,f}$ values could then be determined using the following equation:

$$ e_{31,f} = \frac{Q_{piezo}}{2 * A * \delta x} \quad\quad (9) $$

where Q_{piezo}, A and δx were generated charge on the sample, area of the electrode and rms strain, respectively.[9]
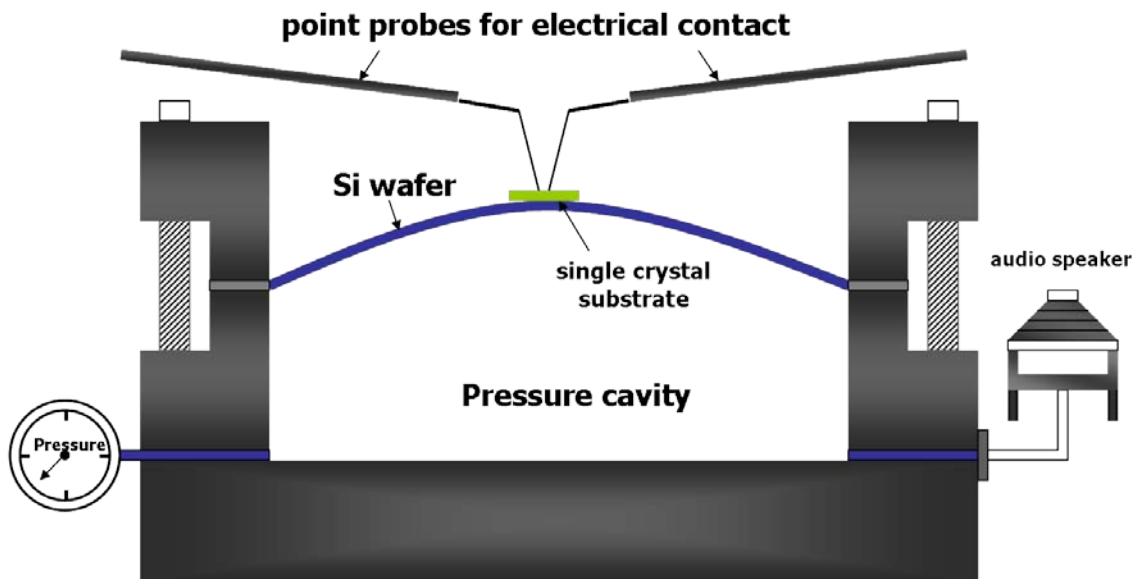
Figure 4.6 Measurement setup for transverse piezoelectric coefficient measurements

4.6 Summary

In this chapter, basic procedures for operation of pulsed laser deposition system were described. Also various structural characterization and compositional analyses techniques were reviewed and measurement processes were explained. Dielectric and piezoelectric characterization techniques developed for thin films such as piezoresponse force microscopy and wafer-flexure method for obtaining piezoelectric charge coefficients were also demonstrated.

References

[1] N. Marandian Hagh, PhD thesis, Rutgers University, New Brunswick, NJ (2006).

[2] J. A. Bellotti, PhD thesis, Rutgers University, New Brunswick, NJ (2003).

[3] B. D. Cullity, *Elements of X-ray diffraction*, 2nd edition, Addison-Wesley Publishing Company Inc. Reading, MA.

[4] Atomic Force Microscope User's Manual.

[5] Rutherford Backscattering Spectroscopy Analysis.

[6] Goki Eda, PhD thesis, Rutgers University, New Brunswick, NJ (2009).

[7] V. V. Shvartsman, N. A. Pertsev, J. M. Herrero, C. Zaldo, and A. L. Kholkin, *J. Appl. Phys.* **97**, 104105 (2005).

[8] K. Prume, P. Muralt, F. Calame, T. Schmitz-Kempen, and S. Tiedke, *IEEE trans. on ultrason. ferro. and freq. cont.* **54**, No. 1 (2007).

[9] J. -P Maria, J. F. Shepard, S. Trolier-McKinstry, T. R. Watkins and A. E. Payzant, *Int. J. Appl. Cerami. Technol.* **2**(1) 51-58 (2005).

5 Piezoelectric $(K_{0.44}Na_{0.52}Li_{0.04})(Nb_{0.84}Ta_{0.1}Sb_{0.06})O_3$ ceramics

5.1 Introduction

Outstanding piezoelectric properties of $(K_{0.44}Na_{0.52}Li_{0.04})(Nb_{0.84}Ta_{0.1}Sb_{0.06})O_3$ (KNN-LT-LS), synthesized by Saito et al. have been receiving much attention in the past few years, as indicated in Chapter 2. Saito et al. attribute the remarkable increase in d_{33} to a MPB in this system, which is created by doping KNN with $LiTaO_3$ and $LiSbO_3$ in addition to texturing. Although the enhancement of piezoelectric properties in this lead-free system was first attributed to a MPB, recent reports suggest the contrary, as exemplified by the KNN-LT binary a subsystem of KNN-LT-LS.[1-7] Room temperature x-ray data, which was collected using Cu K_α radiation and by using a step-scan procedure with 0.02°/step and 2 s dwell time in the range of 20–80°, was refined by whole profile fitting (WPF) using the software package JADE.[8] The purpose of this chapter is to examine the structure of synthesized KNN-LT-LS at room temperature so as to find a relationship between the structure and the reported properties.

5.2 Phase and structure of KNN-LT-LS composition

Figure 5.1 shows the X-ray diffraction pattern of KNN-LT-LS powder, which was calcined in mixed-oxide route according to the procedure described in previous chapter. The pattern is indexed based on tetragonal as well as orthorhombic structure. Several fitting strategies were investigated in the analysis of the X-ray pattern of KNN-LT-LS using WPF, as summarized in Table 5.1. First, the pattern was refined using the crystallographic data in the ICDD-71-0948 card as starting point, which involved

constraining the refinement to point group P4mm -a primitive polar unit cell of tetragonal symmetry. The refinement was repeated, however, this time allowing all possible reflections in the tetragonal Laue classes 4/m and 4/mmm. In both cases the results were perfectly reproducible, yielding a unit cell volume of 62.2 $\mathring{A}^3$, which is typical for ferroelectric perovskites with primitive unit cells. To check the possibility of an orthorhombic phase, the same pattern was refined with WPF using data on ICDD-77-1098 card, a crystallographic data set which has been used in some previous reports [9], while constraining the refinement to orthorhombic space group Amm2. The refinement gave a good fit to the data. However, the computed unit cell turned out to be 125.67 $\mathring{A}^3$, which is an unrealistically large unit cell for a material with a perovskite structure and a primitive lattice. Therefore, refinements were carried out first with Pmm2 constraint, and then by allowing all orthorhombic reflections in the Laue class mmm. Under these circumstances, the unit cell volumes were 62.1 and 62.3 $\mathring{A}^3$; respectively.
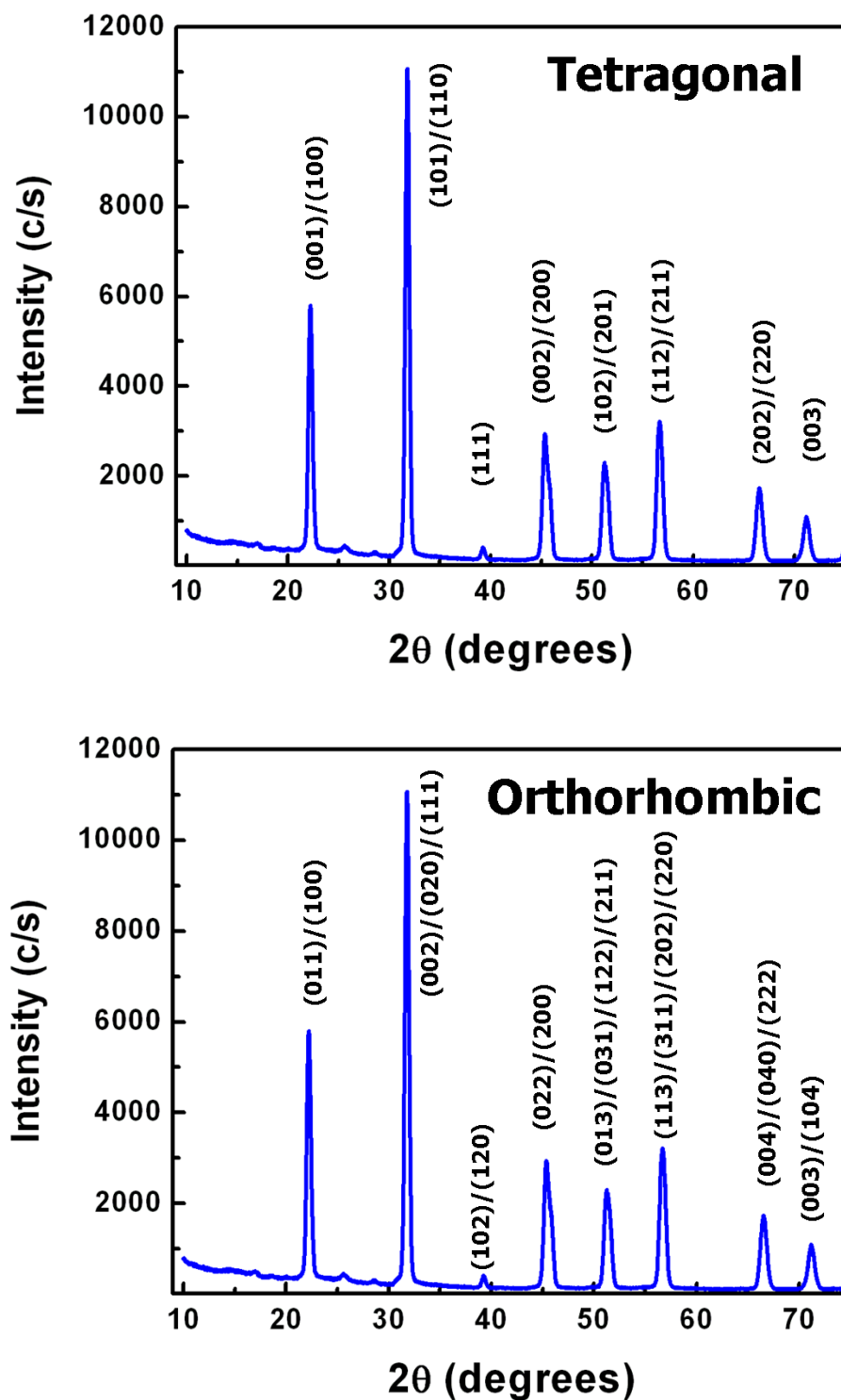
Figure 5.1 High resolution X-ray diffraction of KNN-LT-LS synthesized powder, the indexing is based on a tetragonal structure.

Table 5.1 Structure and lattice constants of KNN-LT-LS ceramic

Phase	a(Å)	b(Å)	c(Å)	V_{cell}(Å³)	Refinement type
Tetragonal	3.9494	3.9494	3.9881	62.2	ICDD 71-0948 (P4mm)
Tetragonal	3.9490	3.9490	3.9876	62.2	Tetragonal primitive
Orthorhombic	3.9478	5.6597	5.6244	128.67	ICDD 77-1098 (Amm2)
Orthorhombic	3.9659	3.9383	3.9771	62.1	Orthorhombic (All)
Orthorhombic	3.9631	3.9401	3.9901	62.3	Orthorhombic (Pmm2)

As can be verified from Table 5.1, both constrained and unconstrained refinements of the tetragonal and orthorhombic Laue classes give consistent results, since the computed unit cell volumes are physically plausible, while a unit cell volume of 125.67 Å^3 is not. By comparing the unit cell volumes of the refinements for tetragonal and orthorhombic Laue classes one notices that both are very close in value. As 2θ peak positions are governed by the unit cell volume, the results suggest that one may not be able to discern the peaks of the tetragonal and orthorhombic phase using conventional (laboratory) diffraction methods due to the peak overlap. That is very important since a two phase co-existence is expected based on thermodynamic considerations in KNN-LT-LS. Specifically, the phase transitions in the KNN-LT-LS system are first order [1]. Hence, there should be multiphase co-existence at the transition point under isobaric and isothermal as per the Gibbs phase rule. The temperature range over which such co-existence occurs may or may not be observable experimentally; however, the possibility of an orthorhombic Amm2 phase with a unit cell volume of 125.67 Å^3 is ruled out,

because of the large unit cell volume **[10]**. Therefore, at room temperature ferroelectric tetragonal and orthorhombic phase co-existence is highly probable based on the X-ray data at hand and is further confirmed by the previous polarization measurements reported in the literature.**[9, 10]**

5.3 Summary

In this chapter, the structure of the KNN-LT-LS composition was examined using high resolution x-ray diffraction of the powder. Based on XRD analysis and refinements carried out using JADE, it was found that in the vicinity of room temperature, the KNN-LT-LS exhibit a two-phase coexistence, with tetragonal and orthorhombic phase, thermodynamically being equally favorable at room temperature. This is further supported by the temperature dependence of polarization demonstrated by Hagh et al and Akdogan et al.

References

[1] E. Hollenstein, M. Davis, D. Damjanovic, and N. Setter, *Appl. Phys. Lett.* **87**, 182905 (2005).

[2] S. Zhang, R. Xia, and T. R. Shrout, *Appl. Phys. Lett.* **91**, 132913 (2007).

[3] S. Zhang, R. Xia, T. R. Shrout, G. Zang, and J. Wang, *Solid State Commun.***141**, 275 (2007).

[4] E. Hollenstein, D. Damjanovic, and N. Setter, *J. Eur. Ceram. Soc.* **27**,4093 (2007).

[5] Y. Dai, X. Zhang, and G. Zhou, *Appl. Phys. Lett.* **90**, 262903 (2007).

[6] L. Wu, J. Zhang, P. Zheng, and C. Wang, *J. Phys. D: Appl. Phys.* **40**, 3527 (2007).

[7] F. Rubio-Marcos, P. Ochoa, and J. F. Fernandez, *J. Eur. Ceram. Soc.* **27**, 4125 (2007).

[8] Jade, *The Data Analysis Software,* Materials Data, Livermore, California, USA (2007).

[9] N. M. Hagh, Ph.D. thesis, Rutgers University, New Brunswick NJ (2005)

[10] E. K. Akdogan, K. Kerman, M. Abazari, and A. Safari, *Appl. Phys. Lett.* **92**, 112908 (2008).

6 Optimization of PLD parameters for KNN-LT-LS thin film growth on SrTiO$_3$ substrate

6.1 Introduction

As discussed in the previous chapters, lead-free KNN-based ferroelectrics have attracted a great deal of attention due to their remarkable piezoelectric properties. However, little study has been done so far on promoting the synthesis and properties of such thin films. The lack of progress in these lead-free thin films can be attributed to the challenges associated with the deposition of high quality thin films. That is particularly important for KNN-LT-LS as it contains three volatile species (K$^+$, Na$^+$, and Li$^+$), which are also light elements. Therefore, the growth of KNN-LT-LS films is prone to the so-called "thermalization problem" in addition to the complications associated with volatilization.[1] There have been several reports showing a considerable loss of Na$^+$ and K$^+$ in the films grown by pulsed laser deposition and sputtering techniques.[2,3] Furthermore, the loss of monovalent species leads to high conductivity in such films, which significantly limits their ferroelectric performance.

In this chapter, deposition of single-phase KNN-LT-LS thin films are studied and effects of main deposition parameteres, namely substrate temperature and background oxygen partial pressure are investigated. Dielectric and ferroelectric properties of such films are demonstrated in order to establish a baseline for dielectric properties of the base KNN-LT-LS composition in thin film form. The substrate of choice was cubic, <100> oriented, which was first coated with SrRuO$_3$ for exploring the possibility of growing highly textured and/or epitaxial films. The films were grown to a thickness of 400-600

nm to exclude strain effects, which would otherwise complicate the analysis of nanostructural evolution in this system.

6.2 Effect of substrate temperature on phase, microstructure and properties of KNN-LT-LS thin films

6.2.1 Phase and structure

Figure 6.1(a) shows the θ-2θ X-ray patterns of the target used for ablation, and the deposited KNN-LT-LS/SrRuO$_3$ thin films with a thickness of approximately 400 nm and 150 nm for KNN-LT-LS and SrRuO$_3$, respectively. As seen in Figure 6.1(a), single-phase KNN-LT-LS thin films exhibiting (00l) orientation, as well as single phase (00l) SrRuO$_3$ bottom layer were obtained as verified by systematic absence of any other (hkl) reflections. Comparing the X-ray pattern of the ceramic target and those of the films deposited at 600-750°C (see Figure 6.1(a)), it can be concluded that only perovskite phase is obtained in all films with a preferred (00l) orientation. A close look at (002) KNN-LT-LS and SrRuO$_3$ peaks reveals that at low deposition temperature (600 ^{o}C) KNN-LT-LS (002) peak has shifted to a higher 2θ considerably, as compared to the films deposited at higher temperatures (700 and 750°C). Since the thicknesses of all films are the same, these peak shifts cannot be related to elastic strain, given that at 400 nm thickness, the films are expected to be fully strain-relieved.[4-6] The observed shifts could be due to compositional fluctuations or minute amounts of secondary crystallographic texture in lower temperature deposited films (600°C) due to slow diffusion kinetics in the growth process of the film.

Figure 6.1(b) shows the ϕ scans for KNN-LT-LS (110) reflection. The scans for 750°C deposited film shows four peaks separated by 90° indicating the locking of in-plane orientational symmetry and cube-on-cube relationship between the film and the substrate.[7] The ϕ scan of the low temperature deposited film (600°C) reveals multiple peaks of very low intensity which may correspond to an interfacial layer with a different orientational symmetry formed at the early stages of KNN-LT-LS growth. These results suggest that a more compositionally uniform and epitaxial KNN-LT-LS thin film can be obtained at a high deposition temperature of 750°C. This will be further substantiated with RBS compositional analysis.
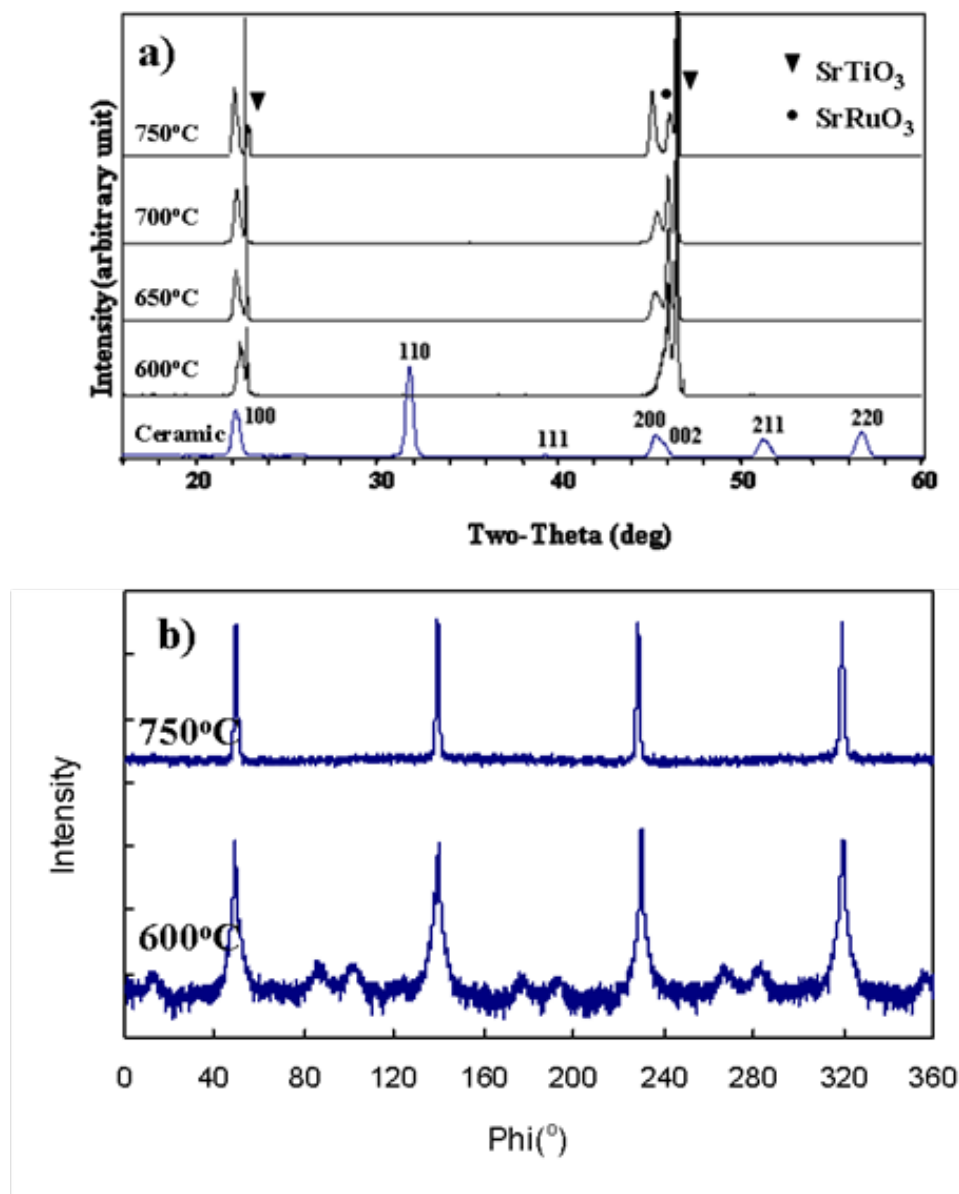
Figure 6.1 X-ray diffraction pattern of the KNN-LT-LS a) target (designated as ceramic), and KNN-LT-LS /SRO deposited at 600-750°C , b) ϕ scans of (110) pole of KNN-LT-LS for 600 and 750°C deposited films

6.2.2   Nanostructural evolution and film's chemistry

Figures 6.2 and 6.3 demonstrate the evolution of nanostructure of the KNN-LT-LS thin films at different deposition temperature. From the FESEM micrographs, it is found that at low temperatures, the films exhibit a columnar structure with 150-200nm grains in width and major axis along [001], pointing out of the plane of substrate. As observed in the FESEM images, with increasing deposition temperature, the columnar grains coalesce whereby the columnar morphology of the nanostructure is lost. Finally at 750°C, the films exhibit a uniform dense cross section as well as a smooth surface, suggesting an epitaxial state in the film.

The Rutherford Backscattering Spectroscopy (RBS) profiles for the KNN-LT-LS/$SrRuO_3$ on $SrTiO_3$ deposited at 600, 650, 700 and 750 $^{\circ}$C are shown in Figure 6.4. The RBS measurements indicate that at high temperature (750 $^{\circ}$C) the measured chemical composition of the film (dotted line) is very close to stoichiometric (simulated, solid curve), while at lower temperatures, especially at 600 $^{\circ}$C, the profile shows a considerable discrepancy between the experimental data (dotted line) and the simulated stoichiometry (solid line). Composition profile of the films deposited at 650 $^{\circ}$C and 700 $^{\circ}$C exhibited the same trend; namely, a decrease in discrepancy between experimental and calculated data with increasing deposition temperature. In the case of 600 $^{\circ}$C (Fig. 6.3(a)), the deviation from the stoichiometric KNN-LT-LS might be related to compositional non-uniformity due to low deposition temperatures where atomic mobility is low. As RBS profile represent the average composition of the exposed area, compositional non-uniformity is known to give rise to deviations from the expected norm. Furthermore, the vapor pressure of a given species increases exponentially with

temperature, and if there were any loss of volatile species that should be in the 750°C. However, from the RBS spectrum the 750 ^{o}C deposited film showed the closest fit to the desired stoichiometry. This is accompanied by a very rough top surface of the films deposited at 600 ^{o}C, as observed from the SEM images. Thus it can be inferred tha the disagreement between the measured compositions of low temperature deposited samples with the simulated stoichiometric composition be most likely due to the compositional non-uniformity and higher surface roughness.
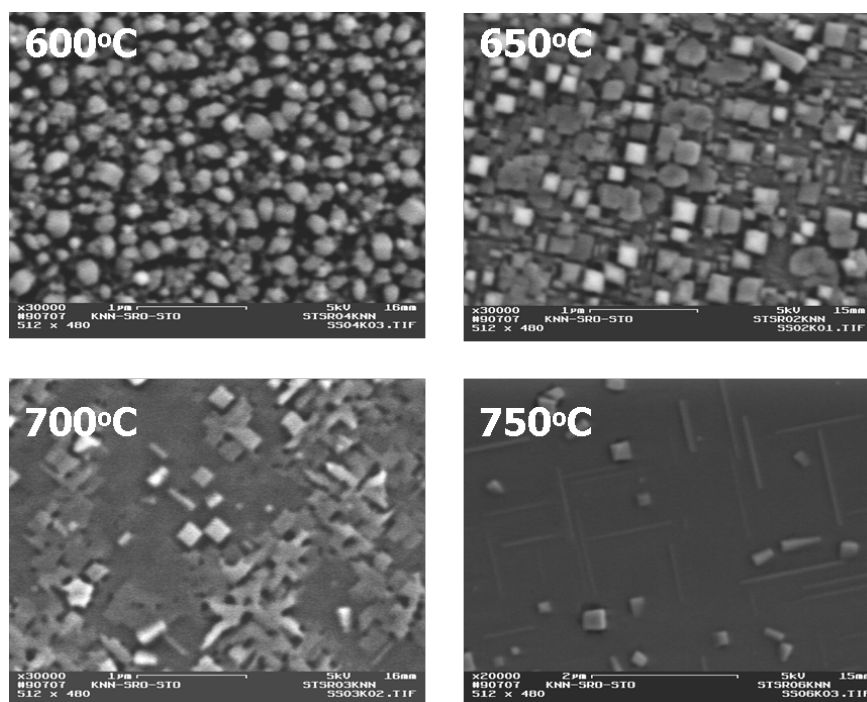
Figure 6.2 Field emission SEM images of surface of KNN-LT-LS/SRO films, deposited at different temperatures
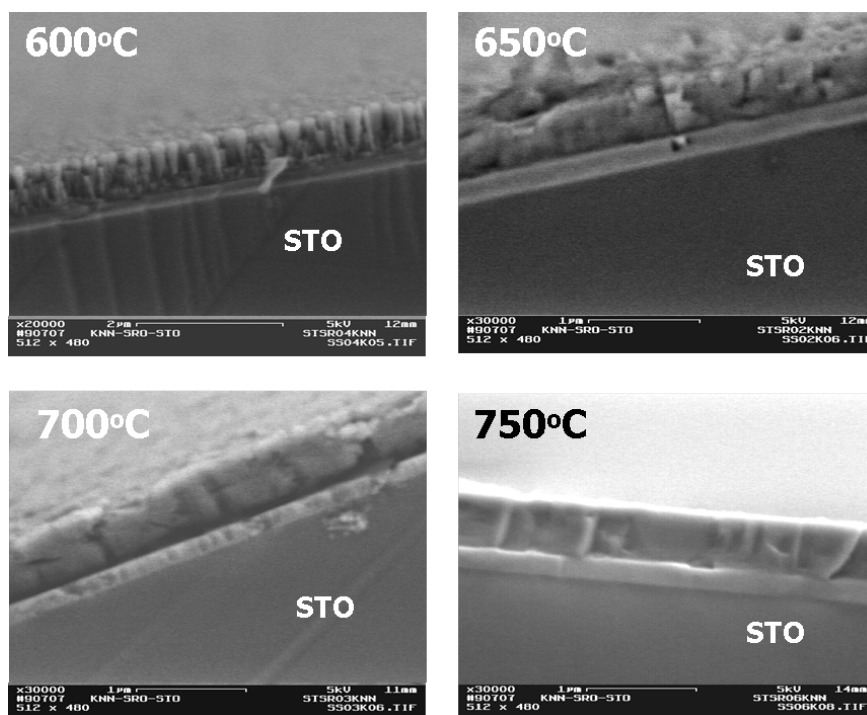
Figure 6.3 Field emission SEM images of cross section of KNN-LT-LS/SRO films, deposited at different temperatures
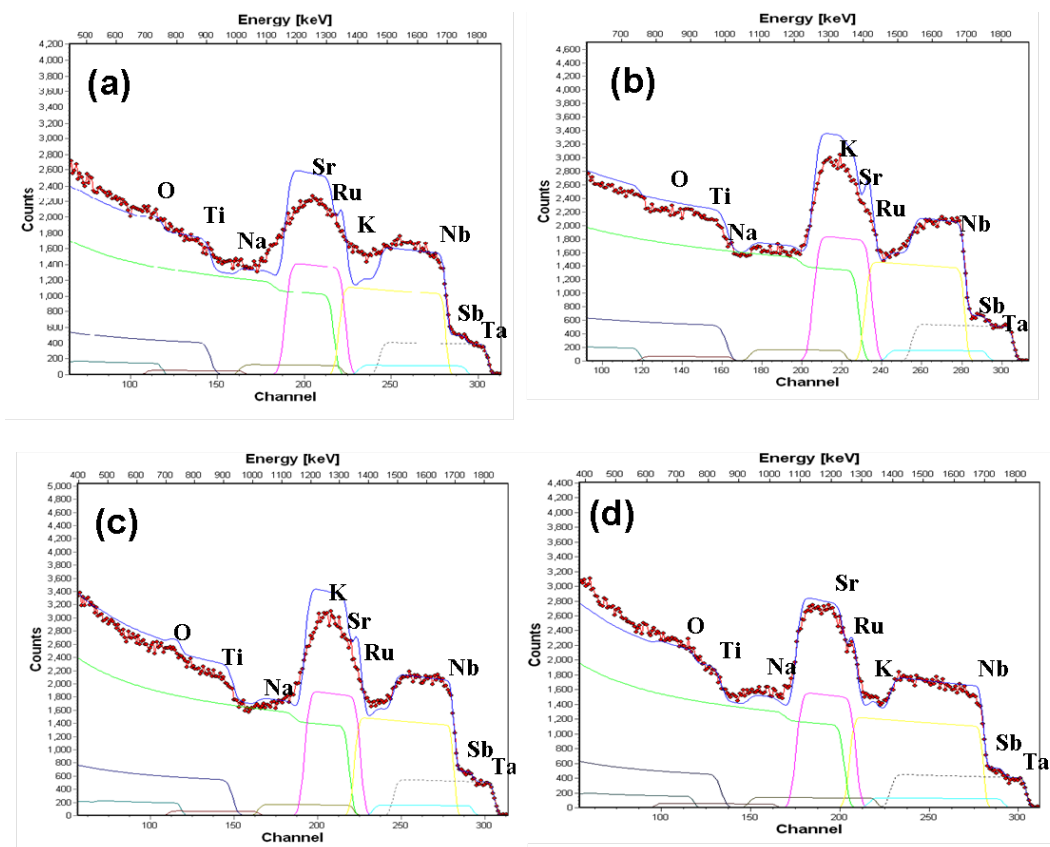
Figure 6.4 RBS composition profiles of the KNN-LT-LS/SRO on STO: a) 600 ^{o}C, b) 650°C, c) 700°C and b) 750 ^{o}C

6.3 Effects of background oxygen pressure on phase, microstructure and properties of KNN-LT-LS thin films

6.3.1   Phase and structure

The θ-2θ XRD patterns of the PLD target (bulk ceramic) and KNN-LT-LS films (deposited with P_{O_2} ranging from 100 to 400 mTorr) are shown in Figure 6.5(a). All films were deposited at substrate temperature of 750 ^{o}C and laser energy density of 1.2 J/cm^{2}, which was shown to be the optimum deposition conditions in previous section. A comparison of these XRD patterns shows that a single perovskite phase has been formed at all P_{O_2} used. Furthermore, Figure 6.5 (b) reveals that the (002) peak in the vicinity of 44° is shifted toward a lower 2θ when the P_{O_2} is increased from 100 to 400 mTorr. The said peak shift cannot be related to strain effects, since the film thickness is 450 nm. Therefore, the data in hand suggests that the shift in 2θ should be due to a change in composition. Furthermore, change in the 2θ position of the (002) peak suggests a change in the c-lattice parameter as per Bragg's law: $2d\sin\theta_{hkl} = \lambda$ (n=1) with $d_{hkl} = \left\{ \left(h^{2}+k^{2}\right) \middle/ a^{2} + l^{2} \middle/ c^{2} \right\}^{-\frac{1}{2}}$. Therefore, at higher P_{O_2} (400 mTorr) the c-parameter of the film, being 3.990 Å as measured from the (002) peak position, is larger as compared to the one at lower P_{O_2} (100 mTorr) which is 3.949Å. These changes in the c-parameter are attributed to the evaporation of volatile A-site K and Na species at lower P_{O_2} under isothermal conditions. However, another possible explanation for the observed peak shift could be a change in crystal orientation of the film with varying P_{O_2} . As the tetragonality is small in this KNN-LT-LS composition (c/a=1.009 in bulk ceramics), the (002) and

(200) peaks at 45.3 and 45.9^o 2θ overlap. Hence, a 0.6^o shift in (002) peak position toward a higher 2θ angle could potentially be induced by a change of orientation direction in the films. In PZT, it has been reported that the c-parameter increases as Pb volatilization is suppressed, resulting in a more stoichiometric film with respect to A-site content, with increasing P_{O_2} .[8] The KNN-LT-LS films appear to follow the same trend as PZT films as well as that of bulk KNN-LT-LS,[9-11] which is elaborated further using thermodynamic arguments in the context of gas-solid phase equilibrium in what follows .

Figure 6.5 (a) Comparison of room temperature X-ray diffraction θ-2θ scan of bulk ceramic and thin films $(K_{0.44}, Na_{0.52}, Li_{0.04})(Nb_{0.84}, Ta_{0.10}, Sb_{0.06})O_3$ grown at various oxygen pressures. (b) (002) peak shift in films deposited at pressures 100-400mTorr. The number to bottom right corner of the pattern is the pressure in mTorr
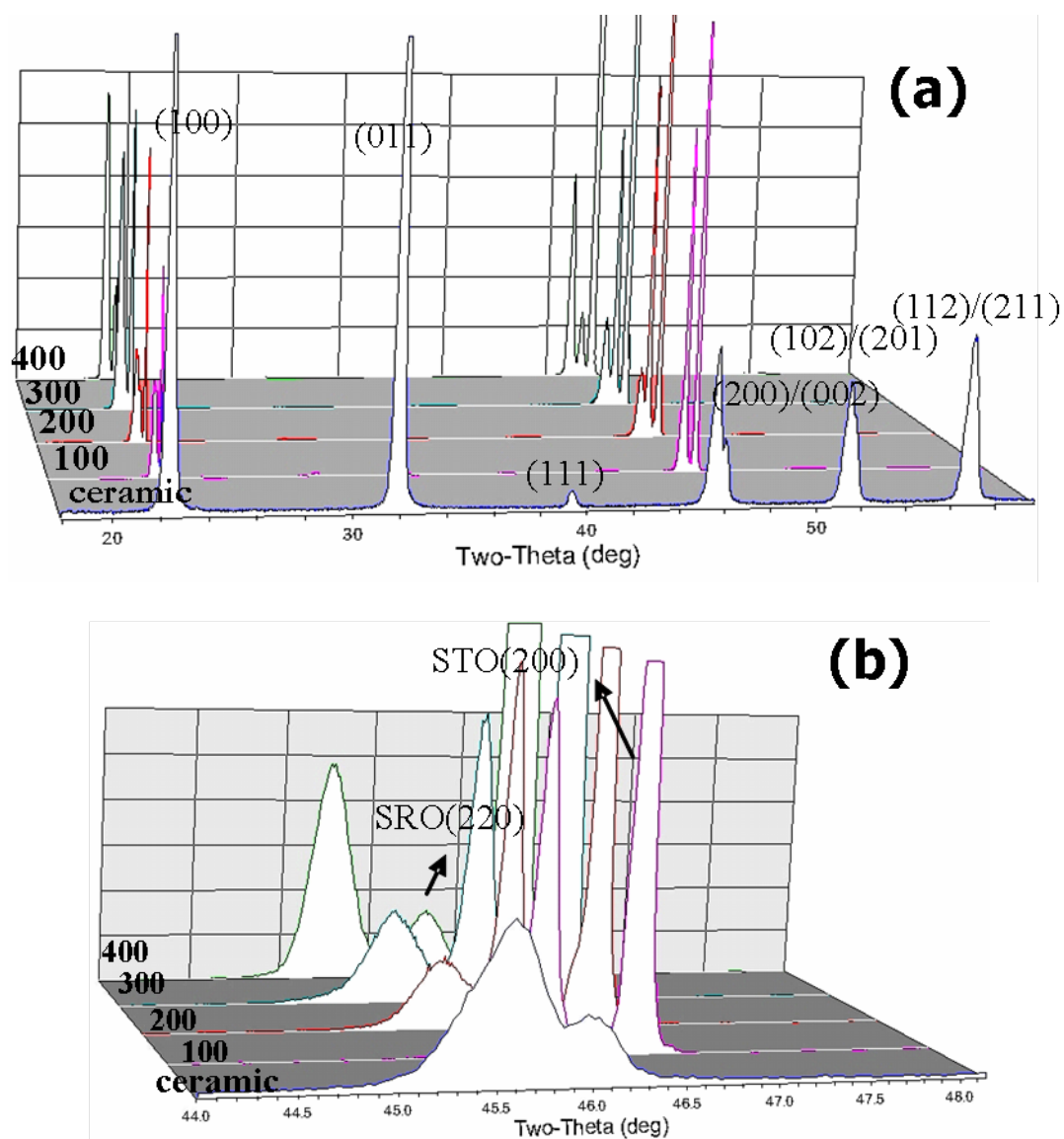
The volatilization of the A-site cations from KNN-LT-LS involves the following gas-solid phase equilibria: M_2O (s) $\leftrightarrow$ 2 M (g) + ½ O_2 (g), where M = K, Na, and Li and designations within parenthesis show standard states. The equilibrium constant (Q^{eqm}) for the phase equilibria in question is $Q^{eqm} = P_M^2 \, P_{O_2}^{1/2} / \, a_M$,[12] where M refers to A-site cations, P is the partial pressure and a is the activity. The temperature dependence of Q^{eqm} is $Q^{eqm} = \exp\{-\Delta G^o / RT\}$, and when used with the previous expression for Q^{eqm} in conjunction with the ideal gas law (n = PV/RT), the following expression is obtained

$$n_M = V\left(\frac{\sqrt{a_m}}{RT}\right)\left(\frac{1}{P_{O_2}^{1/4}}\right)\exp\left\{\frac{-\Delta G^o}{RT}\right\}$$

where n is the number of moles of species M, V is the volume of the system, and ΔG^o is the standard free energy associated with the decomposition of the oxide. As can be verified from the above equation, there is an inverse relationship between P_{O_2} and the number of moles of A-site elements in gaseous phase. In other words, the higher the P_{O_2} in the ambient, the less is the extent of volatilization of the A-site cations. This will be further confirmed by EDS chemical compositional analysis in the following section.

6.3.2   Microstructure, surface morphology and film's chemistry

The SEM micrographs in Figure 6.6 show the top surface of the films, which were grown under oxygen partial pressures of 100 mTorr and 400 mTorr. At lower P_{O_2}'s (100mTorr), the surface morphology consists of what appears to be rod-shaped features, which become much smaller or in width or indiscernible with increasing background P_{O_2}. The cross section of all the films showed a smooth crack free film with no significant

difference in the microstructure. The observed surface morphology is reminiscent to what has been previously seen in $NaNbO_3$ films on $SrTiO_3$ substrates by Saito et al.[13] Such a surface morphology, which is attributed to surface relieve patterns and ferroelastic domains, have been also observed in other oxide films and has been referred to as surface undulations[14,15]. They constitute a so-called secondary stress relief mechanism in addition to stress relief by misfit dislocation formation [15], which only appears in thicker films. The formation of such a surface morphology is attributed to the interplay between increased surface energy and the strain energy release via mass transport at high temperatures during film growth or during the cool down cycle.[14]

The results indicate that the observed surface morphology gradually disappears with increasing P_{O_2}. Therefore the observed morphological changes are most probably related to the effect of P_{O_2} on diffusion kinetics of A-site and oxygen stoichiometry since mass transport in oxides is ambipolar.[16]
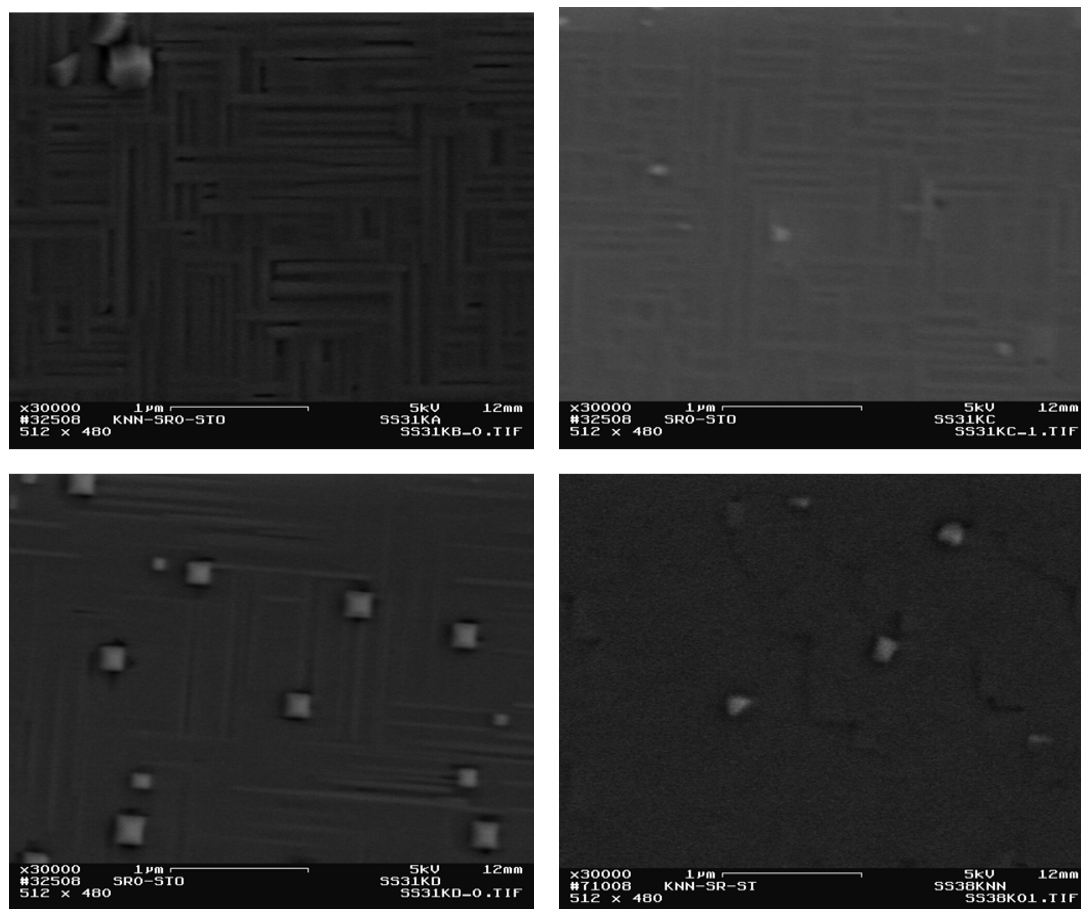
Figure 6.6 Scanning Electron Microscopy (SEM) micrographs of $(K_{0.44}, Na_{0.52}, Li_{0.04})(Nb_{0.84}, Ta_{0.10}, Sb_{0.06})O_3$ thin films deposited at a)100, b)200, c)300 and b) 400 mTorr, showing the evolution of the microstructure.

In order to assess the chemical composition of the films and investigate the hypothesis proposed in the previous discussion, EDS compositional analysis was performed and the results are shown in Figure 6.7. The analysis was performed based on the ratio of A-site and B-site elements, since precise composition could not be determined without using the standards which is a rather cumbersome process. Additionally, lithium content could not be determined using the EDS analysis due to the theoretical limitations of the technique.

The results presented in Figure 6.7 (a) shows that the ratio between K and Nb increases with increasing the partial pressure of oxygen as discussed in detail in previous section. Also, it is observed that the ratio becomes very close to stoichiometric value (dashed line) at 400 mTorr. However, the ratio of K/Nb shows a decrease upon increasing the pressure above 400 mTorr, which indicates the higher thermalization of potassium as compared to niobium. Therefore it can be inferred that there is an optimum oxygen partial pressure where the films show almost stoichiometric composition without undergoing massive thermalization.

Figure 6.7 (b) demonstrates the ratio between Na and Nb in the films. The results indicate that sodium content was close and slightly above the stoichiometric value at low pressure and increases with increasing the oxygen partial pressure. The ratio between A-site (K and Na) and B-site elements (Nb, Ta, Sb) is plotted against the oxygen partial pressure in Figure 6.7 (c). As clearly seen from the figure, the ratio increase with oxygen partial pressure monotonically, passes through the stoichiometric value, showing similar trend as the Na/Nb ratio. Looking at the three plots presented in Figure 6.7 and also looking at the vapor pressure of Na and K at the deposition temperature, it is concluded

that K volatilize significantly more than Na and this can be suppressed by increasing oxygen partial pressure. Also, at lower oxygen pressures, Na content is close to stoichiometric whereas K is far below that of desired value and this keeps the A/B ratio below the desired value of 0.96. With increasing partial pressure of oxygen, both Na and K contents as well as A/B ratio increase, such that the latter reaches above the stoichiometric value. Hence, it is suggested that excess Na ions (above the stoichiometric) substitute K in the lattice. The latter explanation will be further supported from the electrical properties of the films, as conferred in the following section.
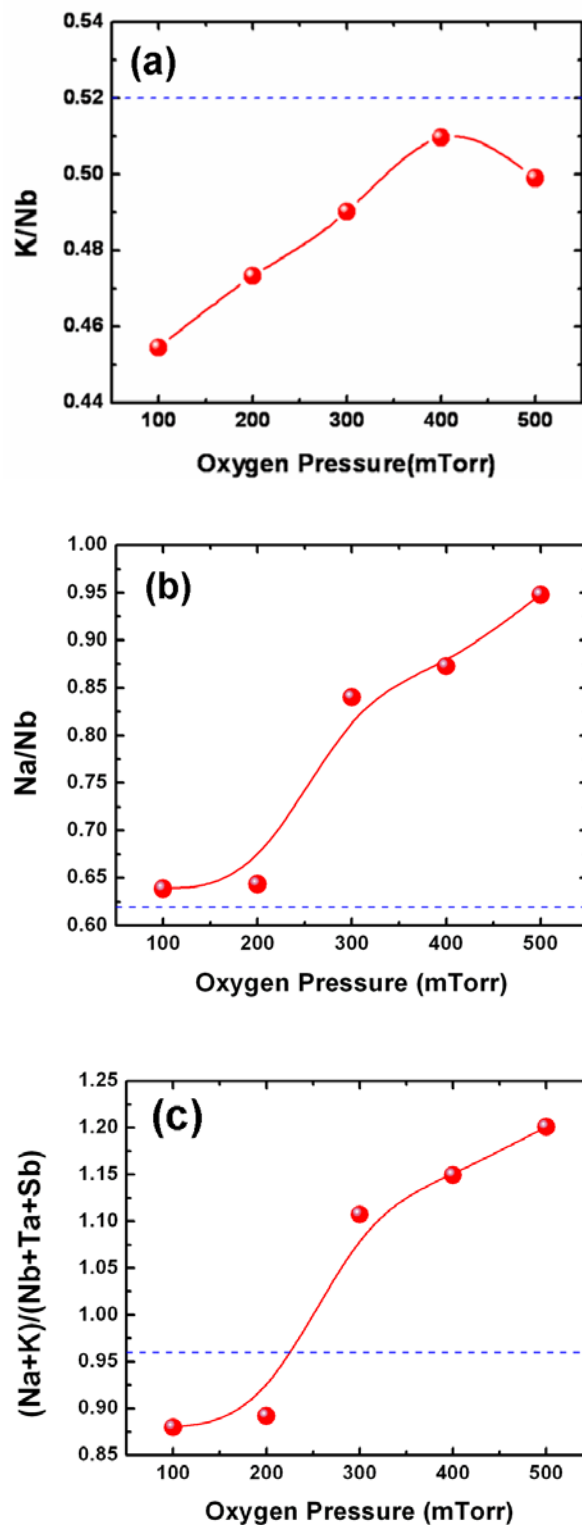
Figure 6.7 (a) K/Nb and (b) Na/Nb and (c) A/B site ratio in films deposited at various oxygen partial pressure using EDS analysis

6.3.3   Dielectric and ferroelectric properties

Polarization-electric field hysteresis loops of films at different oxygen partial pressure during deposition are shown in Figure 6.8. At P_{O_2} =100 mTorr, the loop appears to be very well saturated with saturation and remnant polarization of 10 and 3 $\mu C/cm^2$, respectively, while the coercive field (E_c hereafter) is 20 kV/cm. With increasing P_{O_2}, spontaneous polarization (intercept with y-axis) is enhanced, while the loops do not appear to be well saturated. However, the saturated and remnant polarization in 400 mTorr films are found to be 7.5 and 16.5 $\mu C/cm^2$, along with an E_c=15 kV/cm. From the hysteresis loops, it is also inferred that an increase in P_{O_2} imparts softer characteristics to the KNN-LT-LS films as the E_c decrease from 20 kV/cm at P_{O_2} =100 mTorr to 15 kV/cm at P_{O_2} =400 mTorr. Moreover, the slope of the intercept with the x-axis $\left(\partial P / \partial E \right)_{P=0}$ in films grown at 100 mTorr exhibit substantial departure (~$\pi/4$ radians) from the $\pi/2$ radians theoretical limit **[17]**, which gradually vanishes with increasing P_{O_2}. Such a deviation of $\left(\partial P / \partial E \right)_{P=0}$ from $\pi/2$ radians suggests that the films deposited at lower P_{O_2} have defect-driven internal fields [18], which should be mainly related to P_{O_2} -controlled A-site vacancies. Also, as indicated by EDS measurements in previous section, the Na content of the films was close to stoichiometric at lower oxygen pressures, i.e. 200 mTorr and it was suggested that Na replace K in the lattice with increasing the pressure. This is in agreement with the lower spontaneous polarization observed in the film deposited at lower pressure. In fact, the shape of the P/E loop, coercive field and polarization of the films deposited at such pressures were closer to those of $NaNbO_3$ thin films.**[3]** Also,

Yamazoe et al recently showed that in KNN-LT-LS thin films on Pt/(001)MgO substrate with a 150nm NaNbO$_3$ buffer layer by PLD, Na content increased and K content decreased with approaching from the surface to the interface between the NN buffer layer and the KNN-LT-LS films. As a result, large P$_r$ and P$_s$ of 26.3 μC/cm^2, 30.3 μC/cm^2, were obtained at a field of 93 kV/cm for 1.4 μm thin films, deposited at 850 ^{o}C, and 225mTorr of O$_2$ partial pressure. The values of polarization are larger than those of the KNN-LT-LS ceramic, which was attributed to the presence of preferred <001> orientation.[18]

Since the saturation of polarization seems to be less promising in the high pressure deposited films, the leakage current behavior of the films at different pressures were examined and plotted against the electric field in Figure 6.9. The current density was found to increase with increasing P_{O_2} and was the highest at 400 mTorr. The increase in the leakage current of the films may be explained based on the work by Kizaki et al on the growth of KNN single crystals where, holes generated in the oxidation process, were found to be the carriers for conduction through the reaction below:[19]

$$V_O^{\cdot\cdot} + 1/2O_2 \rightarrow O_O^* + 2\dot{h}$$
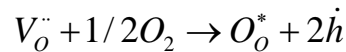
When KNN crystals absorb oxygen into the lattice, holes are generated as a result of oxygen vacancies being occupied. Therefore, the higher current density is observed at crystals grown at a higher oxygen flow. Same line of reasoning may be applied to the thin films, deposited in this study, where a higher leakage current is measured at films deposited at a higher oxygen partial pressure.

The room temperature dielectric constant of the films at 1 MHz deposited at various P_{O_2} is demonstrated in Figure 6.10. The variation of dielectric constant with P_{O_2} parallels

with the increase of spontaneous polarization with increasing P_{O_2} is found to be linear to a good approximation in the range 100-400 mTorr, increasing from ~220 to ~450.

Following the discussion above and the observed increase of dielectric constant and spontaneous polarization with P_{O_2}, it is suggested that the P_{O_2}-controlled A-site stoichiometry have the following ramifications: a) the higher the P_{O_2}, the closer the A-site cation concentration to ideal stoichiometry, the higher the domain wall mobility, resulting in b) higher spontaneous polarization. This implies that the increase in spontaneous polarization with P_{O_2} is extrinsic in origin since ferroelectric films of thickness greater than 100 nm are known to be polydomain.[20] This is justified reasoning in view of the fact that in such polydomain films, the physical properties are chiefly governed by electric field driven domain wall motion [21] at frequencies well-below the lowest soft mode frequency (~400 GHz) in first order ferrodistortive systems such as KNN-LT-LS.[22] It is also important to point out that sintering under oxygen flow rates as high as 180 cm³/min yields KNN-LT-LS solid solutions with the highest d_{33} (~350 pC/N) and spontaneous polarization (~22 $\mu C/cm^2$). [10,11] Therefore, the results reported on KNN-LT-LS thin films herein is in conformity with what is known in the case of bulk solid solutions, which in turn indicates P_{O_2} phenomena is universal across multiple length scales in this lead-free ferroelectric system.
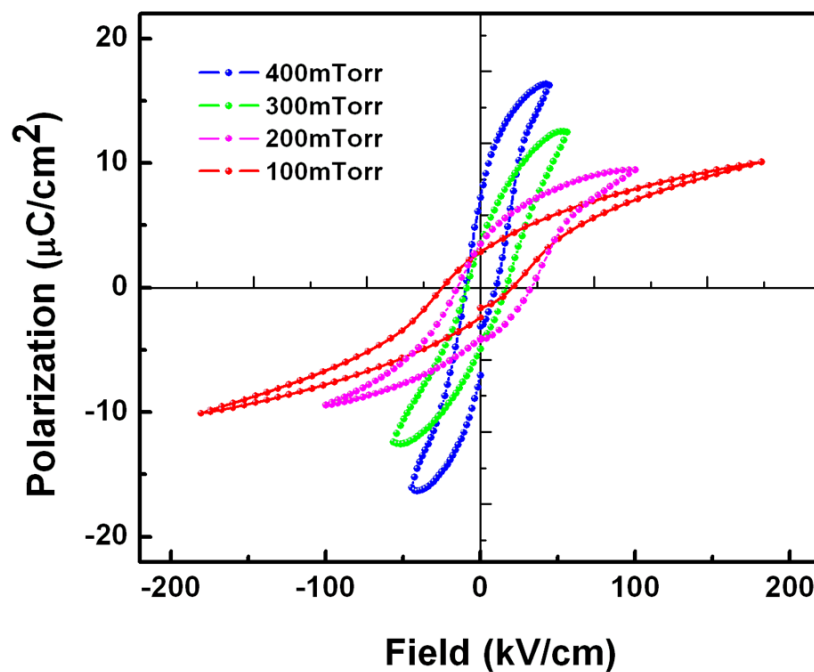
Figure 6.8 Comparison of room temperature hysteresis loops of $(K_{0.44}, Na_{0.52}, Li_{0.04})(Nb_{0.84}, Ta_{0.10}, Sb_{0.06})O_3$ thin films, at various background oxygen pressures
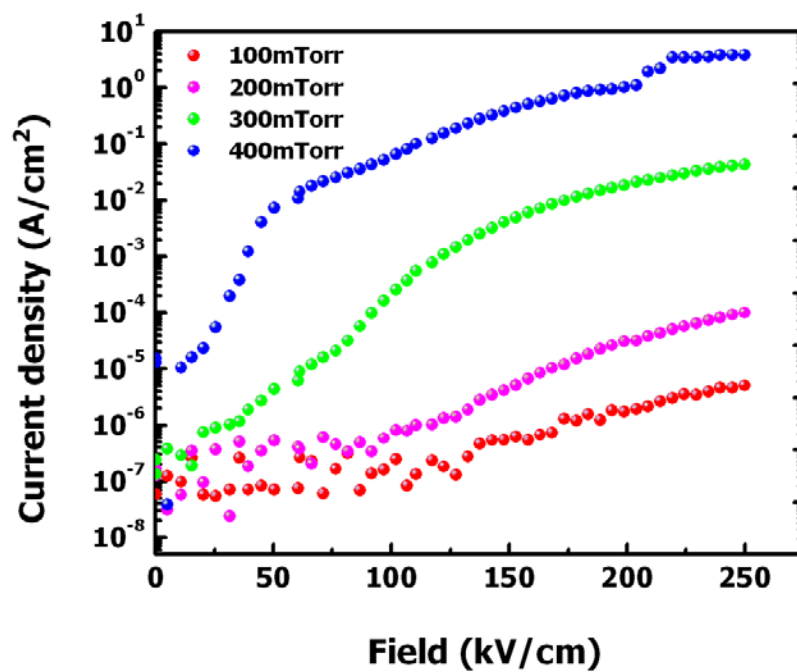
Figure 6.9 Leakage current behavior in KNN-LT-LS thin film deposited at different oxygen partial pressures.
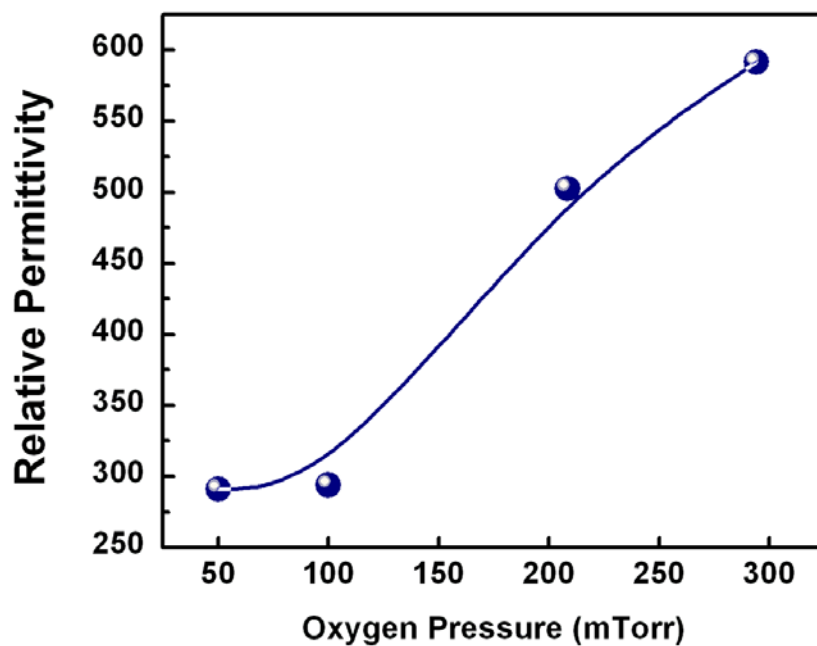
Figure 6.10 Variation of dielectric constant with oxygen partial pressure during thin film deposition at 1 MHz and room temperature
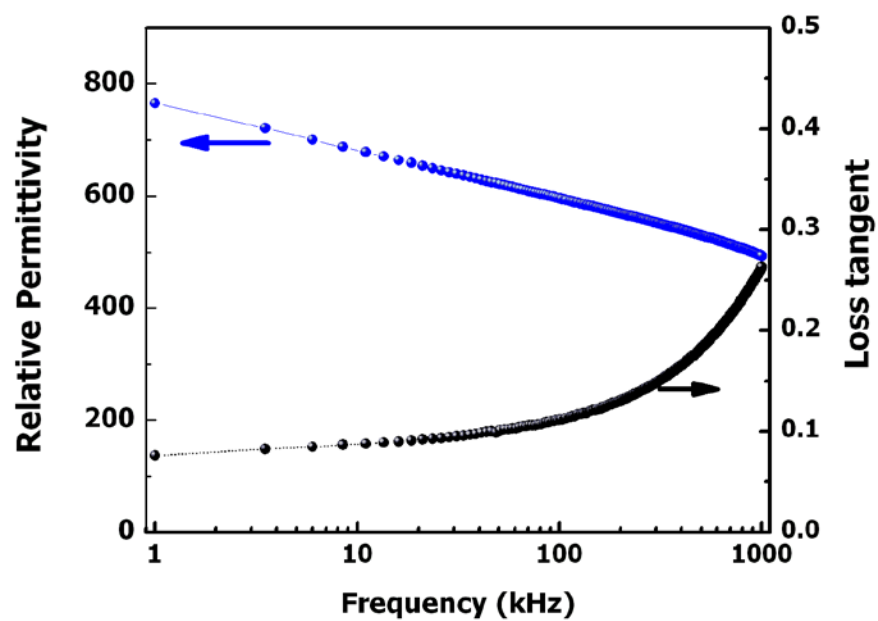
Figure 6.11 Relative permittivity and loss tangent of KNN-LT-LS films deposited at 750°C.

Frequency dispersion of relative permittivity and dissipation factor in KNN-LT-LS thin films deposited at the optimized conditions, e.g. 750 ^{o}C, 400 mTorr oxygen partial pressure and 1.2 J/cm^{2} laser energy density is examined and illustrated in Figure 6.11. The dielectric constant reaches a value of ~750 at 1 kHz, but exhibits frequency dependence and decreases monotonically to ~580 at 1 kHz. Loss tangent, on the other hand, is approximately constant around 5-6% up to 100 kHz, above which tends to increase up to 12% at 1000 kHz. These values are about half of and twice the values reported for KNN-LT-LS bulk material for dielectric constant and loss, respectively.[10] The decrease in permittivity and the increase in loss tangent with increasing frequency is attributed to low resistivity, arising probably from deviations in A-site stoichiometry in single phase KNN-LT-LS. Previous work on KNN-LT-LS film by Saito et al.[11] reported a relative dielectric constant of 800 and a loss tangent of 8% at 1 kHz in KNN-LT-LS films of 2800 nm thickness. The dielectric properties of KNN-LT-LS films obtained in this study are very comparable to those of Saito et al's, but at a much lower thickness (600 nm). The improvement in dielectric and ferroelectric properties is probably due to stringent control and optimization of deposition parameters, such as a decrease in target-to-substrate distance from 9 cm (Saito et al.) to 6.4 cm (this study). Larger target-to-substrate distance would cause the light species to undergo thermalization more significantly than the heavy species before reaching on the substrate, resulting in their deficiency during the film growth.[1]

6.4 Summary

In this chapter, it was shown that single-phase <001> oriented epitaxial KNN-LT-LS films can be grown on <100> oriented SrRuO$_3$ coated <001> SrTiO$_3$ by the judicious choice of PLD deposition parameters. The nanostructure of the films were investigated in the 600-750°C temperature range and was found to have transitioned from columnar grains with <001> texture to <001> epitaxy. The results presented irrevocably shows that the thickness of KNN-LT-LS films can safely be pulled below 1000 nm, while retaining 22% of the bulk remnant polarization. Additionally, it was shown that higher P_{O_2} enhanced the dielectric and ferroelectric properties of KNN-LT-LS thin films. The origin of such an enhancement is ascribed to the suppression of volatile A-site cations loss, which in turn results in enhanced domain wall mobility and hence reduced E$_c$. The conductivity of KNN-LT-LS remains to be a challenge, as evidenced in the dielectric loss and polarization data, despite close compositional control. This could in principle be surmounted by donor doping such as Ba^{2+} and manganese, which will be investigated further in chapter 7.

References

[1] C.-R. Cho, A. Grishin, *Appl. Phys. Lett.*, 75, 2, pp. 268-270 (1999).

[2] C. Zaldo, D. S. Grill, R. W. Eason, J. Mendolia, and P.J. Chandler, *Appl. Phys. Lett.*, **65**, 502 (1994).

[3] T. Saito, T. Wada, H. Adachi and I. Kanno, *Jpn. J. Appl. Phys.*, 43, 6627 (2004).

[4] W.K. Simon, E.K. Akdoğan, A. Safari, *J. Appl. Phys.*, **97**, 103530 (2005).

[5] J. W. Matthews, A. E. Blakeslee, *J. Cryst. Growth*, 27, 118 (1974).

[6] B. S. Kwak, A. Erbil, J. D. Budai, M. F. Chisholm, L. A. Boatner, B. J. Wilkens, *Phys. Rev. B*, **49**, 14865 (1994).

[7] B. Nagaraj, S. Agrawal, T. S. Song, T. Sawhney and R. Ramesh, *Phys. Rev. B*, **59**, 16022 (1999).

[9] J. Lee, Rutgers University, PhD thesis, New Brunswick, New Jersey (1994).

[10] N. Marandian Hagh, K. Kerman, E.K. Akdogan, A. Safari, *unpublished*

[11] N. Marandian Hagh, Rutgers University, Ph.D. Thesis, New Brunswick, New Jersey (2006)

[12] N. M. Hagh, B. Jadidian, and A. Safari, *J. Electroceram.* **18**, 339 (2007).

[13] C.H.P Lupis, *Chemical Thermodynamics of Materials*, Elsevier (1983)

[14] T.Saito, H. Adachi, T. Wada and H. Adachi, *Jpn. J. Appl. Phys.* **44**, 6969 (2005)

[15] W. K. Simon, E. K. Akdogan, A. Safari, *J. Appl. Phys.* **97**, 103530 (2005).

[16] L. B. Freund, *MRS Bull.* **17**, 52 (1992)

[17] H.-I. Yoo, D.-K. Lee, *Phys. Chem.*, 5, 2212 (2003).

[18] S. Yamazoe, Y. Miyoshi, K. Komaki, H. Adachi, T. Wada, *Jpn. J. Appl. Phys.* **48**, 09KA13 (2009).

[19] A. P. Levanyuk, *Defects and Structural Phase Transitions*, Gordon & Breach Science Publishers (1988).

[20] Y. Kizaki, Y. Noguchi, M. Miyayama, *Appl. Phys. Lett.* **89**, 142910 (2006).

[21] S. P. Alpay, and A. L. Roytburd, *J. Appl. Phys.* **83**, 4714 (1998).

[22] M.J. Haun, E. Furman, S. J. Jang, H. A. McKinstry, L. E. Cross, *J. Appl. Phys.*, **62**, 3331 (1987).

[23] R. Blinc, B. Zeks, *Soft Modes in Ferroelectric & Antiferroelectrics* (North Holland Publishing Co. 1974).

7 Effects of doping on ferroelectric properties and leakage current behavior of KNN-LT-LS thin films on SrTiO₃ substrate

7.1 Introduction

KNN-based ceramics have shown a substantial sensitivity to processing conditions, such as the purity of the precursor materials and flow of oxygen during sintering [1]. On the other hand, fabrication of KNN-based thin films by pulsed laser deposition has been reported to have more inherent difficulties associated with the film growth as indicated in chapter 2 and 6. Several reports have revealed that these problems are primarily correlated to the A-site element, especially K and Na, which are volatile and at the same time light, which in turn lead to the formation of secondary phases.[2-4] As a consequence of volatility of A-site elements and hence their deficiencies in the lattice, KNN-LT-LS sub-micron thin films have shown high leakage currents which result in the degradation of polarization, as discussed earlier in chapter 6.

In lead-based thin films with a highly volatile Pb, there have been numerous studies to improve the resistivity of the films through suppression of the volatilization and donor doping.[5-9] Donor doping is believed to affect the leakage current through introduction of extra electrons into the composition which counteracts the inherent p-type conductivity of the films, due to A-site vacancies. Several donor dopants have been tried in $Pb(Zr,Ti)O_3$ (PZT hereafter) thin films such as La^{3+}, and Nb^{5+} to name a few. In this case, introducing the aliovalent atoms into the lattice distorts the electroneutrality of the compound. Therefore, donor dopants with higher valences than the A-site elements would compensate for the negatively charged A-site deficiencies, and acceptor dopants with lower valences compensate for positively charged oxygen vacancies. Hence donor

doping increases the A-site vacancies, while acceptor doping leads to an increase in the oxygen vacancies concentration.[10-13]

In KNN-LT-LS ceramic system, specifically, few dopants, namely Ba^{2+} and Cu^{2+} have been tried by Hagh et al in order to improve the coupling coefficient and mechanical quality factor and reduction of dielectric loss. Addition of 0.5 mol% Cu^{2+} resulted in higher density, lower dielectric loss and the stabilization of the orthorhombic phase through shifting tetragonal-orthorhombic phase transition to a higher temperature. Also, 1 mol% substitution of Ba^{2+} increased the bulk resistivity as well as piezoelectric charge coefficient, d_{33}, and longitudinal coupling coefficient, k_p and k_{33} [14,15] It is interesting to note that although KNN-LT-LS system has shown a relatively low solid solubility for both Ba^{2+} and Cu^{2+} (about 2 mol%), addition of small amount of either Ba^{2+} or Cu^{2+} have made a considerable difference in the bulk properties. Surprisingly, 1 mol% addition of La^{3+} has shown to substantially degrade the densification in KNN-LT-LS pellets that is contrary to its effect in PZT system. In contrast, the ionic radius of La^{3+}, 1.36Å, was found to be close to those of A-site cations in KNN-LT-LS system, being 1.64Å, 1.39Å, 0.92Å for K^+, Na^+, and Li^+ respectively. Therefore, the low solid solubility of KNN-LT-LS might have led to the observed degradation of sintering. Also there are several reports on the effect of Mn on potassium niobate-based ceramics, showing the notable improvement on the resistivity of the ceramic and stabilization of polarization.[16-19]

In this chapter, the effects of various dopants such as Ba^{2+}, Ti^{4+} and Mn^{4+} have been studied on the phase, microstructure, electrical properties as well as leakage current behavior of the KNN-LT-LS thin films. Mn-doped as well as Ba and Ti-doped KNN-LT-LS films are deposited in optimized conditions, e.g. deposition temperature and pressure,

e.g. $750^{o}C$, 400 mTorr and 1.2 J/cm^{2}, so as to obtain highly crystalline and epitaxial thin films with out-of-plane orientation. The resistivity of the films have been attributed to both A-site deficiencies as well as oxygen vacancies and the relationship between either of these two with the ferroelectric polarization of the films has been speculated.

7.2 Effect of dopants on phase and microstructure

Figure 7.1 shows the XRD patterns of (a) undoped, (b) Ba-doped, (c) Mn-doped, and (d) Ti-doped KNN-LT-LS thin films deposited at $750^{o}C$ and 400mTorr oxygen pressure. As shown no secondary phase has been formed in the doped films, as well as no noticeable difference in the unit cell size, comparing the peak positions in the doped film to the undoped one. This clearly shows that the dopants have been incorporated into the KNN-LT-LS lattice, substituting A and/or B-site elements.

Figure 7.2 shows the SEM micrographs taken from the surface of undoped, Mn, Ba, and Ti-doped films. The surfaces of all films show a smooth matrix with a small population of surface crystals. No grain boundaries or cracks have been observed with a dense cross section across the thickness of the films. However in Ba-doped film more surface crystals have been observed which are along the crystallographic directions of the substrate. Nevertheless, the observed crystallites are not likely to be associated with a secondary phase, as evidenced by the XRD patterns. Since in the case of Ba-doped KNN-LT-LS bulk ceramic, the sintering temperature slightly increases, crystallites may vanish with providing a higher mobility of the arrived species at the substrate through increasing the deposition temperature.[1]
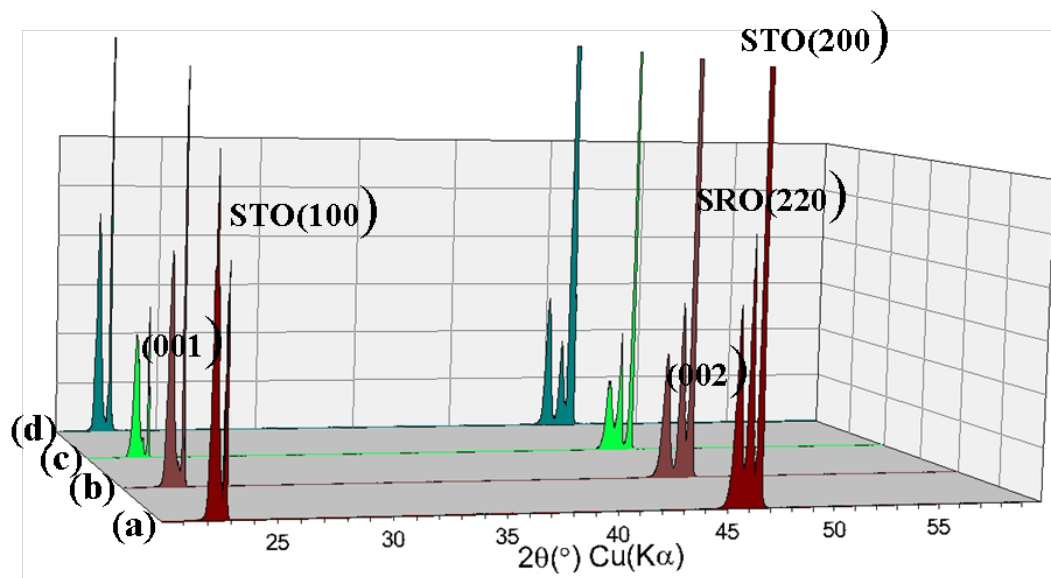
Figure 7.1 Comparison of room temperature X-ray diffraction θ-2θ scan of 500nm a)undoped, b)Ba-doped, c)Mn-doped and d)Ti-doped KNN-LT-LS thin films grown at 750°C and 400 mTorr, showing no secondary phases in the films
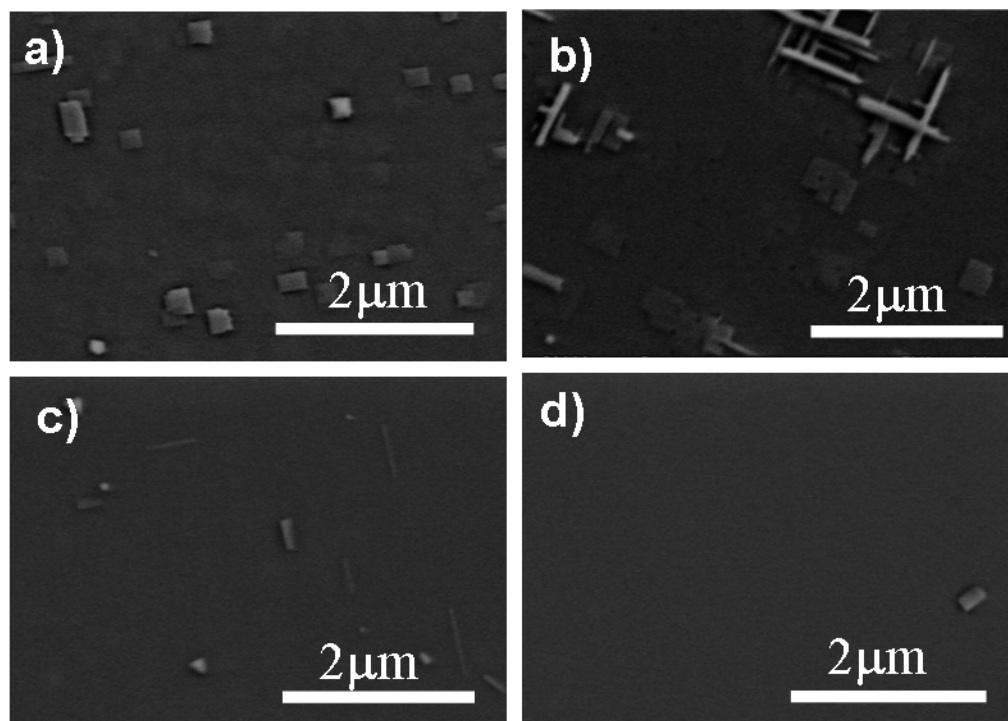
Figure 7.2 Scanning Electron Microscopy (SEM) micrographs of a)undoped, b)Ba-doped, c)Mn-doped, and d)Ti-doped KNN-LT-LS thin films

7.3 Effects of dopants on dielectric and ferroelectric properties

Dielectric constant and loss tangent of the films as a function of frequency are plotted in Figure 7.3. As shown, the dielectric constant is ~ 760 in undoped film at 1 kHz, while it is ~800 for Mn and Ti-doped films and ~300 for Ba-doped films. Also dielectric constants of all films show a relaxation type behavior with a monotonic decrease in the measured range of 1 kHz to 1 MHz and reach ~500-550 for undoped, Ti and Mn-doped films, while it is ~200 for Ba-doped film. Loss tangent, on the other hand, increases with frequency from ~0.08 for undoped and Ti-doped and ~0.07 for Mn and Ba-doped films at 1 kHz to 0.26, 0.27, 0.17 and 0.15 for undoped and Ti-doped films at 1 MHz respectively. In addition, loss tangent increases monotonically in the measured range which is in agreement with the relaxation behavior of dielectric constant.
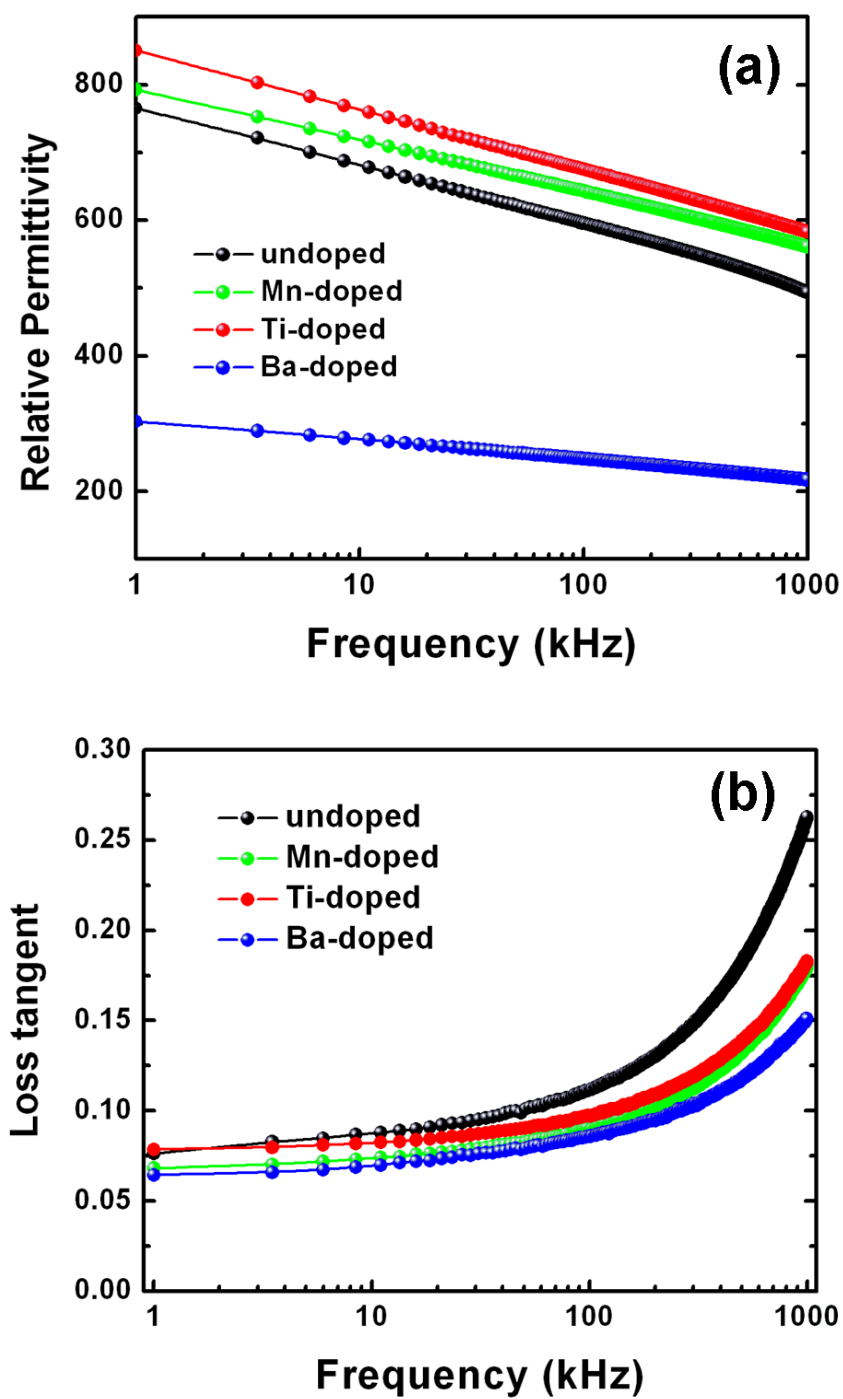
Figure 7.3 Frequency dependence of room temperature (a) dielectric constant and (b) loss tangent of undoped and doped KNN-LT-LS thin films in the range of 1-1000kHz

Figure 7.4 shows the polarization-electric field hysteresis loops of undoped and doped KNN-LT-LS thin films. The saturated polarization (P_{sat} hereafter) values are 19, 23, 14 and 8 $\mu C/cm^2$ while remanent polarizations (P_r hereafter) are 10, 15, 6 and 3 $\mu C/cm^2$ for undoped, Mn, Ti and Ba-doped films respectively. This value of remanent polarization in Mn-doped thin films is ~ 70% of P_r in bulk KNN-LT-LS ceramic (22 $\mu C/cm^2$) and the highest value reported for KNN-LT-LS thin film in the literature. Comparing the P/E loops of undoped with Ba-doped thin films, it is revealed that Ba has not improved the polarization and indeed has degraded the saturation as well. Conversely, P/E loop for Mn-doped film is well saturated with a high P_r and P_s. Addition of Ti^{4+}, however, resulted in a lower polarization and diminished saturation. The coercive field for undoped film is ~ 15 kV/cm and stays the same for Ba and Ti-doped as the undoped film, while for Mn-doped film, it increases to 22 kV/cm. This shows that Mn-doping has a "hardening" effect on KNN-LT-LS, while at the same time it improves the polarization or dipole alignments, which is a "softening" behavior.
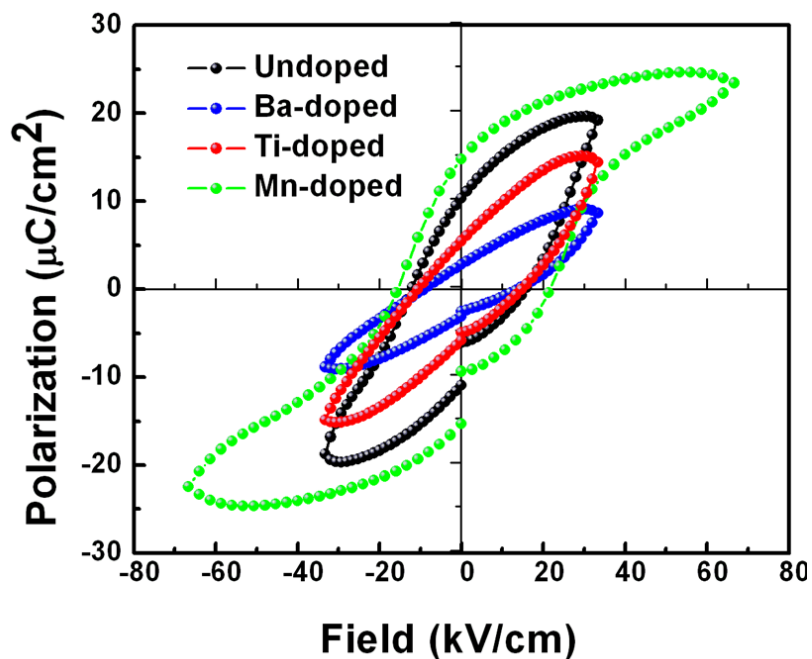
Figure 7.4 Comparison of room temperature hysteresis loops undoped and doped KNN-LT-LS thin films, measured at 100Hz
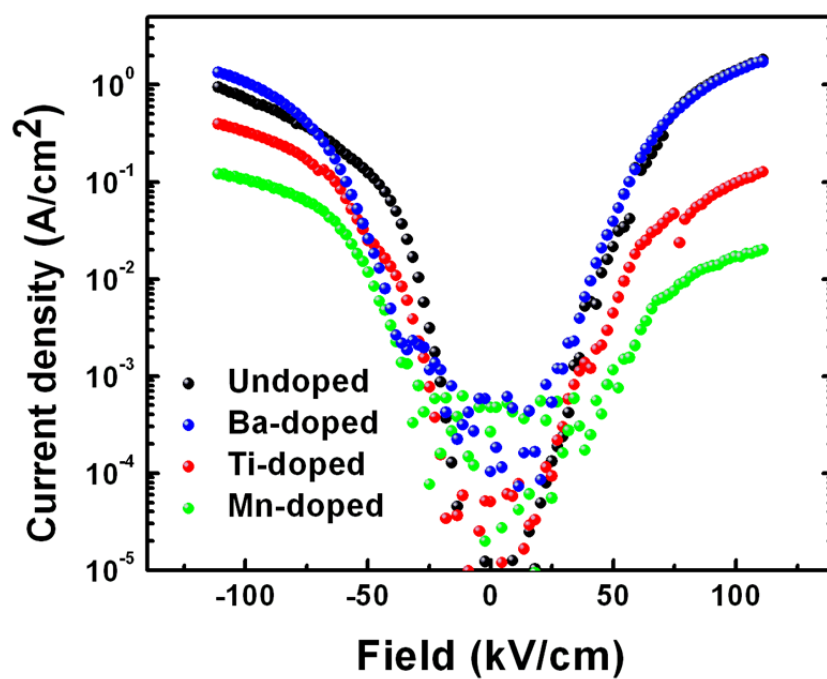
Figure 7.5 I/V curves (current density vs. electric field) of undoped and doped KNN-LT-LS thin films, measured at room temperature

The details of transport mechanism in KNN-LT-LS thin films and ceramic are still unknown, although it is speculated that A-site cations' volatility and deficiencies are mostly responsible for the observed leakage current in this system. In order to assert the leakage current, I/V characteristic of the KNN-LT-LS thin films have been measured and illustrated in Figure 7.5. The I/V curves show that the leakage current density has been decreased in Mn doped films by more than two orders of magnitude, while Ba-doped film has shown very slight increase in the leakage current. Ti-doped film, also exhibits an order of magnitude suppression in leakage current in higher fields region compared to undoped film. The leakage current at a field of 70 kV/cm is $\sim 2 \times 10^{-1}$ A/cm^2 in undoped film, while the same are $\sim 5 \times 10^{-3}$, 4×10^{-2}, and 3×10^{-1} A/cm^2 for Mn-doped, Ti-doped and Ba-doped films. In addition, the onset of breakdown voltage has been raised in Mn-doped films, e.g. films tends to have an increase in leakage current at 25 kV/cm when undoped, while the same is 50 kV/cm when doped with Mn. These results show that although Ba^{2+} had increased the resistivity in bulk KNN-LT-LS ceramic, it is not as effective on the thin films.

It is previously reported that in bulk KNN-LT-LS, since the ionic radius of Ba^{2+}, 1.61 Å is very close to those of the A-site cations, namely K$^+$, Na$^+$, and Li$^+$ (1.64, 1.39, and 0.92 Å respectively), Ba can effectively substitute the A-site and generate an A-site vacancy according to the following reaction:

$$Ba_K \rightarrow Ba_K{}' + \bar{e} \qquad (1)$$
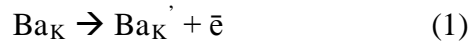
In addition, K$^+$ vacancies that form during the sintering process, act as electron traps for the excess electrons that Ba^{2+} introduces into the composition and hence this charge carrier extermination counteracts the native p-type conductivity of bulk KNN-LT-LS,

leading to a higher resistivity. Also, it has been shown that 1 mol% Ba-doping was optimal level to reduce conductivity, beyond which secondary phase were formed leading to an increase in conductivity. However, in Ba doped thin films, slight increase in the leakage current are likely due to increased A-site defects, generated during laser ablation and it is possible that 1 mol% doping might not have been sufficient to reduce leakage current effectively. Therefore, excess free electrons and/or uncompensated A-site defects are most likely the reason for the observed increase in leakage current.

B-site acceptor substitution typically results in a "hard" ferroelectric with a decrease in dielectric loss, and an increase in the coercive field. It is also known that acceptor dopants diminish the number of A-position vacancies normally present and cause the existence of oxygen vacancies in the lattice.[20] Vacancies in the position of oxygen in perovskite structure tend to shrink the unit cell size. This shrinkage is thought to contribute to the increased coercive field. In CuO-added KNN-LT-LS ceramic, Cu had a dual effect, since it showed a "hardening" effect on the piezoelectric charge coefficient, as well as decrease in the coercive field, which is a "softening" effect. Therefore, it was speculated that Cu could have actually occupied both sites. Taking into account the fact that in perovskite ceramics with relatively compact structures, there is a small chance for dopants to occupy interstitial sites, in a similar fashion, Mn can occupy either A or B-sites, based on the following reactions:

$$MnO_2 \rightarrow Mn_A{}^{ooo} + 2O_O + 3V_A{}^{'} \qquad (2)$$

$$MnO_2 \rightarrow Mn_B{}^{'} + 2O_O + V_O{}^{o} \qquad (3)$$
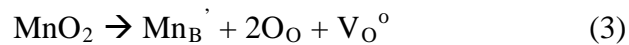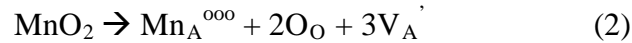
These created oxygen vacancies in reaction (3) are considered responsible for the observed increase in coercive field in hard ferroelectrics, which is also the case in Mn-

doped KNN-LT-LS thin film. However, the results indicated that polarization and resistivity have been enhanced by Mn doping implying that Mn might act as "softnenig" dopant, as well. In comparison to PZT system, for instance, La^{3+} and Nd^{5+} as donor dopants, increase the piezoelectric coefficient and loss tangent and reduce the coercive field. On the other hand, substitution of the A-site cation by Mn^{4+} with ionic radius of 0.53Å does not seem a strong supposition. It is thus suggested that Mn^{4+} converts to Mn^{2+} and create oxygen vacancy thereby, based on the following reaction:

$$Mn^{4+} \rightarrow Mn^{2+} + V_O{}^{oo} \qquad (4)$$
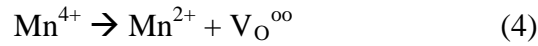
The generated Mn^{2+} with ionic radius of 0.9Å is possible to occupy the A-site vacancies, being close in radius to some the A-site cations' radii such as Na^+, and Li^+, 1.39 and 0.92Å respectively. Nevertheless, it is difficult to assign one valence state to a multi-valent Mn and given that the properties are partially those of A-site dopant and partially B-site, therefore we conclude that Mn has most likely occupied both sites.

Also Ti^{4+} is mostly expected to substitute the B-site cations as an acceptor dopant in KNN-LT-LS, namely Nb^{5+}, Ta^{5+}, Sb^{5+}, since its ionic radius, 0.605Å, falls in the range of those of the B-site's, 0.64, 0.64, 0.6 Å respectively. On the other hand, Ti^{4+} has not increased the coercive field, which is a typical effect of an acceptor dopant. It is found experimentally that increase in hole concentration favors increase of oxygen vacancies according to:

$$2h + O^{2-} \rightarrow O \uparrow + V_O \qquad (4)$$
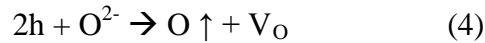
This limits hole concentration.[20] This provides an explanation for the observed lower leakage current in Ti-doped KNN-LT-LS thin films as compared to the undoped films.

7.4. Summary

In conclusion, various dopants such as Ba, Mn, and Ti have been tried in KNN-LT-LS thin films in order to suppress the leakage current and improve the ferroelectric polarization in KNN-LT-LS thin films fabricated by pulsed laser deposition. It was found that Mn effectively decreased the leakage current as well as enhancing the remanent and saturated polarization over 100%. Conversely, Ba doping did not reduce the leakage current, and therefore failed to help saturate the polarization. Ti, acting an acceptor for the B-site, reduced the leakage current by an order of magnitude, while polarization values showed no significant increase. Mn-doped thin films deposited at 750°C and 400mTorr of background oxygen pressure have shown 15 and 23 μC/cm^2 remanent and saturated polarization respectively. This has been attributed to Mn occupying both A and B-site to reduce the leakage current and improve the polarization as well as a "hardening" effect on coercive field. Improvement in the polarization as well as leakage current in Mn-doped KNN-LT-LS films, make them a promising candidate for lead-free thin film and their applications.

References

[1] N. Marandian Hagh, Ph.D thesis, Rutgers University, 2006.

[2] C. Zaldo, D. S. Grill, R. W. Eason, J. Mendolia, and P.J. Chandler, *Appl. Phys. Lett.* **65**, 502 (1994).

[3] T. Saito, T. Wada, H. Adachi and I. Kanno, *Jpn. J. Appl. Phys.* **43**, 6627 (2004).

[4] C.-R. Cho, A. Grishin , *Appl. Phys. Lett.* **75**, 268 (1999).

[5] H. Fujita, S. Goto, M. Sakashita, H. Ikeda, A. Sakai, S. Zaima, Y. Yasuda, *Jpn. J. Appl. Phys.* **39**, 7035 (2000)

[6] J. Lee, A. Safari, and R. L. Pfeffer, *Appl. Phys. Lett.* **61,** 1643 (1992).

[7] K. S. Grabowski, J. S. Horwitz, D. B. Chrisey, *Ferroelectrics* **116**, 19 (1991)

[8] W. B. Wu, K. H. Wong, C. L. Mak, C. L. Choy, and Y. H. Zhang, *J. Appl. Phys.* **88,** 2068 (2000).

[9] J. F. Tressler, S. Alkoy, and R. E. Newnham, *J. Electroceram* **2**, 257 (1998).

[10] Zhang, Q. and R. W. Whatmore, *J. Appl. Phys.* **94**, 5228 (2003)

[11] J. Robertson, C. W. Chen, W. Warren, and C. D. Glueben, *Appl. Phys. Lett.* **69**, 1704 (1996).

[12] K. Watanabe, A. Hartmann, R. Lamb, R. Craig, M. Thurgate, and J. Scott*, Jpn. J. Appl. Phys.* Part 2 **39**, L309 (2000).

[13] M. Grossmann, O. Lohse, D. Bolten, U. Boettger, T. Schneller, and R. Waser, *J. Appl. Phys.* **92**, 2680 (2002).

[14] N. M. Hagh, B. Jadidian, E. Ashbahian, and A. Safari, *IEEE Trans.Uultrason. Ferro. Freq. Cont.* **55**, 214 (2008)

[15] N. M. Hagh, K. Kerman, B. Jadidian, A. Safari, *J. Euro. Ceram. Soc. in print*

[16] K. Matsumoto, Y. Hiruma, H. Nagata, and T. Takenaka, *Ceramics International* **34**, 787 (2008)

[17] K. Matsumoto, Y. Hiruma, H. Nagata, and T. Takenaka, *Jpn. J. Appl. Phys.* **45** 4479 (2006)

[18] H. R. Xia, C. J. Wang, H. Yu, H. C. Chen, and M. Wang, *Jpn. J. Appl. Phys.* **36**, 2179 (1997)

[19] Li, H. Kakemoto, S. Wada, T. Tsurumi, *J. Ceram. Soc. Jpn.* **115**, 250 (2007)

[20] B. Jaffe, *Piezoelectric Ceramics* (New York: Academic Press 1971).

8 Electromechanical behavior and piezoelectric properties of KNN-LT-LS thin films

8.1 Introduction

From piezoelectric device application perspective, it is essential to study the domain structure and piezoelectricity of thin films and understand the complex interplay between them to further improve the overall electromechanical properties. However, this has been hindered mostly due to the absence of single-phase high quality KNN-based thin films. In previous chapters, it was demonstrated that doped KNN-LT-LS films exhibit improved polarization saturation with low leakage currents. Lee et al have lately reported a d_{33} of ~ 45 pm/V for morphotropic phase boundary (MPB) composition of $(K_{0.48}Na_{0.52})NbO_3$ thin films, while making no reference to their domain structure. [1] Nakashima et al also showed an effective d_{33} of ~ 46 pm/V for chemical solution deposited 600 nm KNN thin films on $Pt/SiO_2/Si$ substrates. [2] Additionally, Kanno et al and Shibata et al demonstrated a transverse piezoelectric coefficient, $e_{31,f}$ values of ~ -3.6 C/cm^2 and -5.5 C/cm^2 for polycrystalline KNN thin films on $Pt/SiO_2/Si$ substrates and respectively. [3,4]

In this chapter, the domain structure of 500 nm epitaxial KNN-LT-LS thin films are investigated utilizing piezoresponse force microscopy (PFM) with reduced leakage current and enhanced ferroelectric properties. Using PFM, the longitudinal piezoelectric coefficients, d_{33} of these films are also measured. Effective transverse piezoelectric coefficient, $e_{31,f}$, of the films are then measured with the application of wafer-flexure method.

8.2 Domain structure observation

The domain structure and switching phenomena in KNN-LT-LS films were studied through inspecting the piezoresponse of the films and demonstrated in Figure 8.1. For PFM measurements, the ac electric field is applied with 1.5V (V_{rms}) at a frequency of 17 kHz. Figure 8.1(a) shows the topography of a typical area on the film. Surface roughness, excluding the surface particulates, was measured using the topography image and found to be 3-4Å, showing atomically flat surface of the film. Nevertheless, the topography image also shows existence of few steps or terraces on the surface of the film. Figure 8.1(b) displays the piezoresponse image of the film which contains both the amplitude (A) and phase (cos θ) response of the films on the probed area. The piezoresponse (PR) image of the film primarily consists of a matrix largely covered with positive values, most likely corresponding to 180° domains with polarization direction extended from top surface to the bottom electrode, and dark orthogonal features with negative PR values. The matrix, however, is composed of a range of positive values with small areas with PR values closer to zero. It is possible that the existence of these small areas correspond to small 90° domains in the matrix. Additionally, the dark orthogonal features, appeared along the step edges on the surface of the samples, show negative PR values. The negative PR response is generally associated with 180° domains with opposite polarity. But since these features show strong correlation with the surface topography, the piezoresponse of these areas might not be accurately interpreted. In order to elucidate the nature of these piezoresponse patterns, and observe 180° domain switching and its effect on possible existing 90° domains, a DC bias of -7 V was applied to the tip, while scanning an area of 4 μm x 4 μm. Two smaller squares of 2 μm x 2 μm and 1 μm x 1 μm

were further "written" by applying +7 V and -7 V, respectively, on the sample's surface as illustrated in Figure 8.1(c). As observed from this figure, the two smaller squares have mostly switched according to the applied electric field direction, creating fairly uniform contrast over the scanned area. However, there still exist small regions with close to zero PR values, remaining almost unchanged after application of electric field. Since these small areas seem to extend along crystallographic direction of the substrate, i.e. [100] and [010], it is suggested that these areas be most likely 90° domains, formed as a result of small tetragonality in the structure. In the larger square, on the other hand, the areas with unaffected polarization direction, appear along the steps on the surfaces. Due to the surface discontinuity on those areas, the nature of the response cannot be precisely determined and remains unclear. The origin of this topographical relief is also related to the spontaneous strain in the ferroelectric and tilting of 90° domain away from normal, as discussed in detail by Foster et al.**[5]**
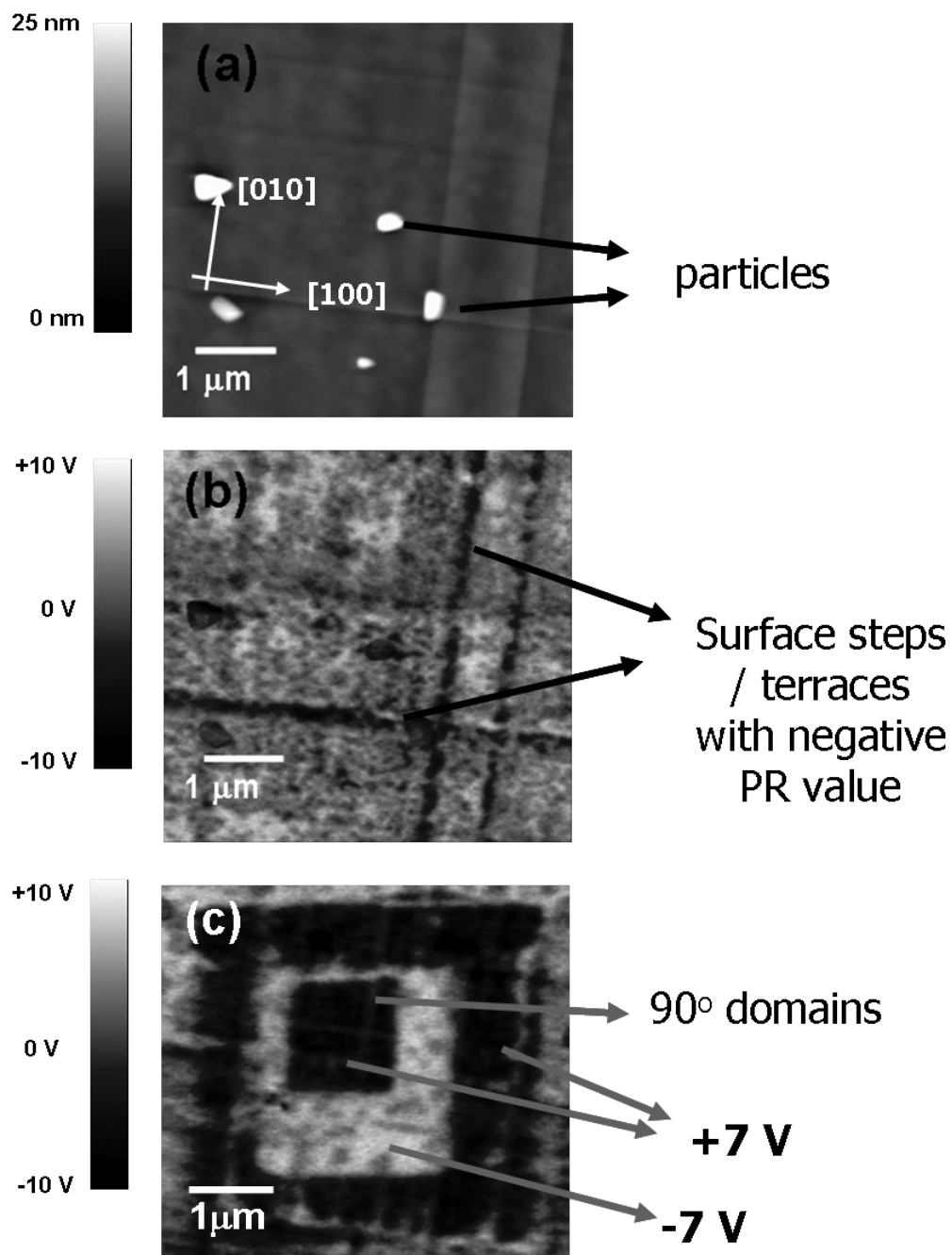
Figure 8.1 a) Topography and b) Piezoresponse (PR) image of as grown and c) poled area on KNN-LT-LS film

Looking at Figure 8.1(c), KNN-LT-LS thin films appear to have less population of 90° domains, as compared to the piezoresponse of highly tetragonal PZT thin films of similar thickness, reported in the literature.[1,6] Generally, 90° domains form in ferroelectric films deposited at high temperatures, which undergo ferroelectric phase transformation upon cooling, as a strain-relief mechanism.[7] The population density of these domains however is closely related to the strain associated with phase transformation (i.e. tetragonality of the ferroelectric structure), lattice misfit with substrate, etc.[5] According to previous studies, the origin of the high piezoactivity of KNN-LT-LS system was found to be due to the presence of a polymorphic phase transition between tetragonal and orthorhombic phases near room temperature (RT).[8,9] As a result of the presence of this transition, large piezoelectric coefficient of 300 pC/N was reported for polycrystalline ceramics at RT. The occurrence of this said phase transition results in the coexistence of tetragonal and orthorhombic phases at RT. Herber et al reported a domain structure composed of 180° and 90° as well as 120° and 60° domains, for morphotropic phase boundary composition $(K_{0.5},Na_{0.5})NbO_3$ single crystals, where both tetragonal and orthorhombic phases were detected. However, in the piezoresponse images of 500 nm thin films, there is no clear evidence of such orthorhombic phase and hence 60° and 120° domain walls. Therefore, KNN-LT-LS thin films with a c/a of %0.9 could possess a tetragonal structure. This is further confirmed by temperature-dependence of dielectric capacitance measurements, as indicated in previous chapter, where no apparent phase transition was observed around room temperature.

8.3 Measurement of longitudinal piezoelectric coefficient

The longitudinal piezoelectric coefficient (d_{33}) for pure and Mn-doped KNN-LT-LS thin films was calculated from the measured displacement and calibrated using the x-cut quartz crystal as a standard sample and plotted against the applied field in Figure 8.2. The deflection of the AFM cantilever has been calibrated at the same level of absolute deflection of the cantilever. All measurements, including quartz crystal and the thin films were made in the same circumstances, e.g. same maximum electric field and frequency. Taking the average value of maximum d_{33} for positive and negative sides of the d_{33} loop, undoped (pure) films show a higher d_{33} of ~ 53 pm/V, as compared to ~ 45 pm/V in Mn-doped films under the bias field of 150 kV/cm. This could be explained considering the hardening effect of manganese in KNNLT-LS films. Although manganese reduced the leakage current and consequently improved the polarization saturation, it had a hardening effect on the piezoelectric properties of the films by decreasing the electromechanical properties. The dual effect of manganese on the properties of KNN-LT-LS film has already been discussed in previous chapters. On the other hand, the d_{33} loops in pure KNN-LT-LS films exhibit a vertical shift toward negative electric field. This observed imprint could be attributed to the pinning of non-switchable domains near the electrodes' interfaces [10] or the effect of different materials used for top and bottom electrodes and is a subject of future study. In addition, the value of d_{33} in pure KNN-LT-LS films is much lower than the bulk value of ~300 pC/N. It is well known that the piezoelectric response in thin films is considerably lower than the bulk samples due to the clamping effect of the substrate.[11,12] However, the d_{33} of the KNN-LT-LS thin films is very much comparable to those of their lead-based counterparts [9-14] and among the highest

values for a lead-free thin film. As summarized in Table 8.1, for PZT-based thin films, reported d_{33} values are above 90 pm/V, while the same has been reported as 45 pm/V for $(K_{0.5},Na_{0.5})NbO_3$ thin films [18]. Lastly as findings of this study show a high piezoelectric actuation in KNN-LT-LS films, electromechanical properties of these films can be further promoted through judicious control of deposition process, avoiding the compositional non-uniformities and oxygen vacancies.
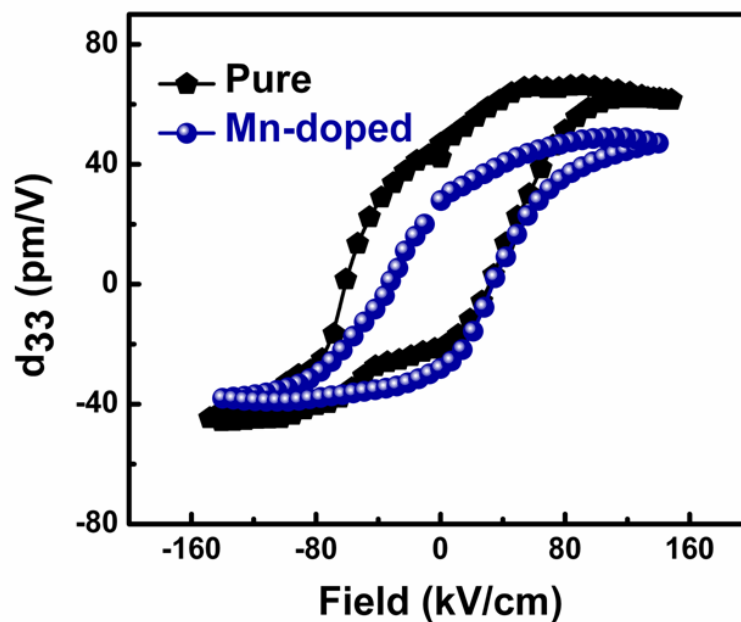
Figure 8.2 Longitudinal piezoelectric coefficient (d_{33}) of pure and Mn-doped KNN-LT-LS film

Table 8.1 Reported values of d_{33} and E_c for various lead-free and lead-based piezoelectric thin films

Composition	d33	Ec	reference
PZT 45/55	100	60	[15]
PZT 52/48	90	70	[15]
PbTiO3	60	65	[22]
CaBi4Ti4O15	60	64	[19]
(Bi,Nd)Ti3O12	38	60	[21]
(Bi0.5Li0.05Na0.35K0.1)TiO3	64	102	[20]
K0.5Na0.5NbO3	45	90	[1]
KNN-LT-LS	55	60	This study

8.4 Measurement of transverse piezoelectric coefficient

The transverse piezoelectric coefficient, $e_{31,f}$ and dielectric constant of the films as a function of poling field are shown in Figure 8.3. Prior to charge measurement, samples were poled for 5 minutes at room temperature. The generated charge (Q) on the film as a result of sinusoidal pressure excitation ($f = 4Hz$) along with the strain imposed on the piezoelectric films was used to estimate the $e_{31,f}$ values as follows:

$$e_{31,f} = -\frac{\text{Charge}}{2 \times \text{Area} \times \text{Strain}} \qquad (1)$$

The factor 2 in the denominator is based on the biaxial strain assumption imposed on the sample, as detailed in chapter 4. To minimize the error due to the sample shape, the output voltage was measured in two orthogonal positions using the strain gauge and the mean of the two readings was taken to calculate the strain on the wafer. As shown, the $e_{31,f}$ values gradually increased to -4.5 C/m^2 for poling field of 20 kV/cm, which is close to the coercive field. This increase of the e_{31} value has also been observed by Shibata et al in epitaxial KNN films on Pt/MgO substrates. [4] However, such increase is absent in highly oriented polycrystalline KNN films on Pt/SiO$_2$/Si substrates and therefore the aforementioned increase is attributed to the crystalline structure of the films. The mechanical properties of KNN-LT-LS have not yet been reported, however, negligible difference is expected for the Young's modulus of KNN-LT-LS with that of KNN. Using the Young's modulus of KNN for KNN-LT-LS thin films, d_{31} could be calculated according to:

$$e_{31,f} = \frac{d_{31,f}}{s_{11}^E} \qquad (2)$$

where s_{11} is the elastic compliance (8.2×10^{-12} m^2/N for bulk KNN). Therefore, d_{31} was found to be approximately 37 pC/N. The value of $e_{31,f}$, on the other hand, showed a slight decrease, upon further increase of the poling field above the coercive field. This decrease in the value of $e_{31,f}$ could be associated with the measurement technique, i.e. the measured stored charge is reduced due to the increased leakage current in the thin film at higher poling field. This has also been reflected in the decrease in the dielectric constant of the films upon increasing the poling field. As shown in Figure 8.3, dielectric constant shows an initial increase with poling field, which is most likely attributed to deaging as reported by Xu et al. Some 180° domain walls may be depinned through formation of a metastable domain structure or redistribution of defect dipoles and thus more 180° domain contribution is observed in the dielectric response (polarizability). On the other hand, the observed decrease in the dielectric constant above the coercive field may be associated with switching of some a-domain into c-domains, as reported by Kohli et al.[17] Until now, only piezoelectric coefficient has been considered as figure of merit, however, depending on the application, more complex figures of merit should be considered, such as signal to noise ratio, as indicated by $|e_{31,f}|/\varepsilon_r$ in Table 8.2, where some of the reported values of $e_{31,f}$ for various lead-free and lead-based thin films, including this study are summarized. {001}-oriented PZT thin films on silicon shows the highest $e_{31,f}$ value of -12, outperforming epitaxial PZT on MgO substrates. However, the measured $e_{31,f}$ of KNN-LT-LS thin films in this study is among the highest reported values for lead-free films.
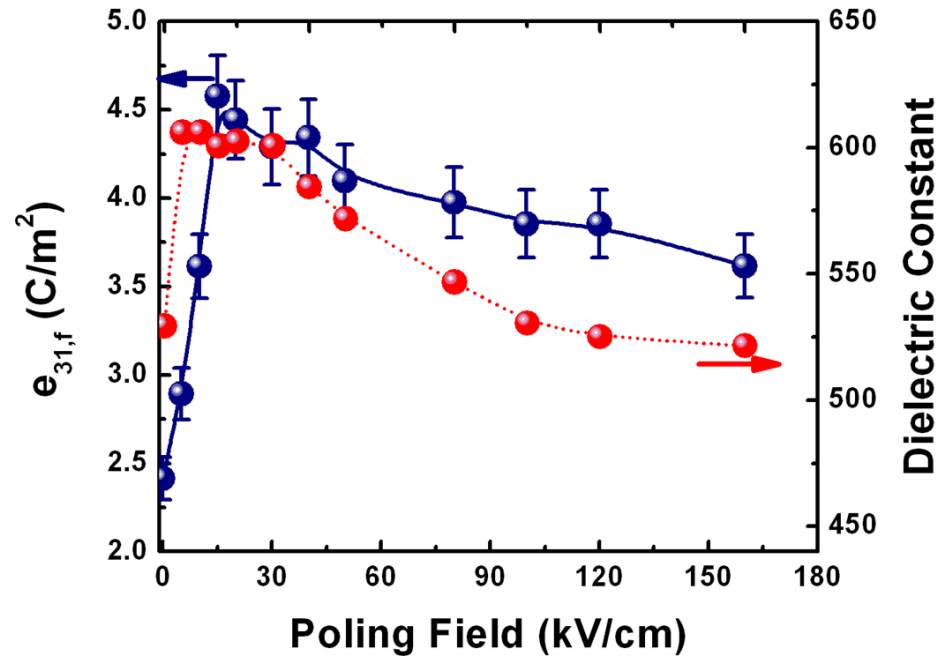
Figure 8.3 (a) $e_{31,f}$ and dielectric constant values for 500nm KNN-LT-LS thin films

Table 8.2 Summary and comparison of $e_{31,f}$ values of thin film in this study and literature

Material system	e_r	$e_{31,f}$	$e_{31,f}/e_r$	References
KNN0.16	320	-2.4	-0.0075	[3]
Epitaxial KNN0.5 on Pt/MgO	550	-3.6	-0.0065	[4]
{001} oriented KNN0.5 on Si	550	-5.5	-0.0100	[4]
Epitaxial KNN-LT-LS on STO	600	-4.5	-0.0075	This study
{001} Epitaxial PZT on MgO	200	-11	-0.0550	[19]
Random PZT(52/48) on Si	1000	-7	-0.0070	[14]
{001} oriented PZT on Si	1300	-12	-0.0092	[14]
AIN	10	-1	-0.1000	[17]

8.5 Summary

Domain structure in epitaxial KNN-LT-LS lead-free piezoelectric thin films on SrTiO$_3$ substrates has been studied using piezoresponse force microscopy (PFM). Also, the effective longitudinal piezoelectric coefficient, d$_{33}$ of these films, was measured using the same technique. The results confirmed the ferroelectricity in the films and that the films possess a tetragonal crystal structure with predominantly c-axis oriented domains. The effective piezoelectric charge coefficient, d$_{33}$, of the film were measured to be ~ 60 and 50 pm/V for 500 nm undoped and Mn-doped films, respectively. Also, using wafer-flexure technique, e$_{31,f}$ was found to be ~-4.5 C/cm^2 for KNN-LT-LS thin films. The presented results demonstrating high transverse and longitudinal piezoelectric coefficient verifies that there is undoubtedly remarkable potential for KNN-based thin films for piezoelectric devices.

References

[1] H. J. Lee, I. W. Kim, J. S. Kim, C. W. Ahn, and B. H. Park, *Appl. Phys. Lett.* **94**, 092902 (2009).

[2] Y. Nakashima, W. Sakamoto, H. Maiwa, T. Shimura, and T. Yogo, *Jpn. J. Appl. Phys.* **46**, No. 14, L311 (2007).

[3] I. Kanno, T. Mino, S. Kuwajima, T. Suzuki, H. Kotera, and K. Wasa, *IEEE Trans. Ultrason. Ferro. Freq. Contr.* **54**, No. 12, 2562 (2007).

[4] K. Shibata, F. Oka, A. Ohishi, T. Mishima, and I. Kanno, *Appl. Phys. Exp.* **1** 011501 (2008).

[5] C. M. Foster, Z. Li, M. Buckett, D. Miller, P. M. Baldo, L. E. Rehn, G. R. Bai, D. Guo, H. You, and K. L. Merkle, *J. Appl. Phys.* **78** 2607 (1995).

[6] V. Nagarajan, I. G. Jenkins, S. P. Alpay, H. Li, S. Aggarwal, L. Salamanca-Riba, A. L. Roytburd, and R. Ramesh, *J. Appl. Phys.* **86**, 595 (1999).

[7] A. L. Roytburd, Phys. *Status Solidi A* **37**, 329 (1976).

[8] E. K. Akdogan, K. Kerman, M. Abazari, A. Safari, *Appl. Phys. Lett.* **92**, 112908 (2008).

[9] S. Zhang, R. Xia, T. R. Shrout, G. Zang, and J. Wang, *Solid State Commun.* **141**, 275 (2007).

[10] A. L. Kholkin, E. L. Colla, A. K. Tagantsev, D. V. Taylor, and N. Setter, *Appl. Phys. Lett.* **96**, 2577 (1996).

[11] S. Hong, *Nanoscale phenomena in ferroelectric thin films*, Kluwer Academic Publishers, New York,2004.

[12] N. Setter, et al, *J. Appl. Phys*. **100**, 051606 (2006).

[13] P. Muralt, *IEEE Trans. Ultrason. Ferroelectr. Freq. Control* **47**, 903 (2000).

[14] Zhi-Xiang Zhu, C. Ruangchalermwong and Jing-Feng Li, *J. Appl. Phys.* **104**, 054107 (2008).

[15] T. Yu, K. W. Kwok, and H. L. W. Chan, *Thin Solid Films* **515**, 3563 (2007).

[16] M. –A. Subois, P. Muralt, *Sensors and Actuators A* **77** 106 (1999).

[17] M. Kohli, P. Muralt, N. Setter, *Appl. Phys. Lett.* **72**, 3217 (1998).

[18] I. Kanno, S. Fuji, T. Kamada, R. Takayama, *Appl. Phys. Lett.* **70**, 1378 (1997).

[19] A. Z. Simoes, M. A. Ramirez, A. Riez, J. A. Varela, E. Longo, R. Ramesh, *Appl. Phys. Lett.* **88,** 072916 (2006).

[20] D. Y. Wang, D. M. Lin, K. S. Wong, K. W. Kwok, J. Y. Dai, H. L. W. Chan, *Appl. Phys. Lett.* **92**, 222909 (2009).

[21] H. Maiwa, N. Iizawa, D. Togawa, T. Hayashi, W. Sakamoto, M. Yamada, S. Hirano, *Appl. Phys. Lett.* **82**, 1760 (2003).

[22] T. Morita, Y. Cho, *Appl. Phys. Lett.* **88**, 112908 (2006).

9 Temperature dependence of the electrical properties of the KNN-LT-LS thin films

9.1 Introduction

In this chapter, an attempt has been made to investigate the capacitance and leakage current behavior of KNN-LT-LS thin films as a function of temperature. One of the most important characteristics of ferroelectric thin films is the leakage current behavior since it provides information regarding the transport mechanism in the films and affects the polarization and charge storage. Leakage current study reveals the nature of the charge carriers in the films and hence may be help to understand and modify the processing conditions of the films to improve resistivity. The current-voltage measurements in this study were carried out in metal-insulator-metal configuration and presented as current density (J) vs. voltage (V) plots.

9.2 Leakage current behavior

The current densities for base and Mn-doped KNN-LT-LS films are plotted against voltage and shown in Figure 9.1 (a) and (b), respectively. In base KNN-LT-LS thin films, leakage current shows more of an unstable behavior at low voltage region (<1 V), where the leakage value and precision of the measurements are both very low, due to the current limitation of the equipment. At higher voltages (>1 V), the current shows an expected exponential increase with voltage. Also, it is seen that the leakage current is dependent on temperature as well, i.e. higher leakages at higher temperatures. In Mn-doped thin films, current at low voltages, below 1V, is more stable but shows higher values than base thin

films. However, at higher voltages, Mn-doped film shows an increase in leakage current with voltage as well as temperature, although the value of leakage current at a voltage of 6V (120 kV/cm) is smaller by two orders of magnitude as compared to base thin films.

In general, the leakage current in ferroelectric thin films originates from four major mechanisms, namely being, space charge-limited current (SCLC), Schottky emission, Poole-Frenkel emission and Fowler-Nordheim tunneling. [1-6] Ohmic current usually dominates at low field region and Fowler-Nordheim tunneling occurs at higher fields with no temperature dependence. However, the presented results show that the leakage current is particularly correlated with temperature, and therefore the possibility of Fowler-Nordheim tunneling is ruled out.

Schottky barrier forms at the interface of a metal and a ferroelectric film with a low concentration of charge carriers. The leakage current in this case is described by the following equation: [1-3]

$$J_{Sch} = A * T^2 \exp\left[\frac{-q\left(\phi_B - \sqrt{\frac{qE}{4\pi\varepsilon_i\varepsilon_o}}\right)}{k_B T} \right] \tag{1}$$

where A is a constant, ϕ_B is the barrier height at the interface, q is the unit charge, E is the applied electric field, ε_i is the dynamic dielectric constant in the infrared region, ε_0 is the permittivity of the free space, k_B is the Boltzmann's constant and T is the temperature.
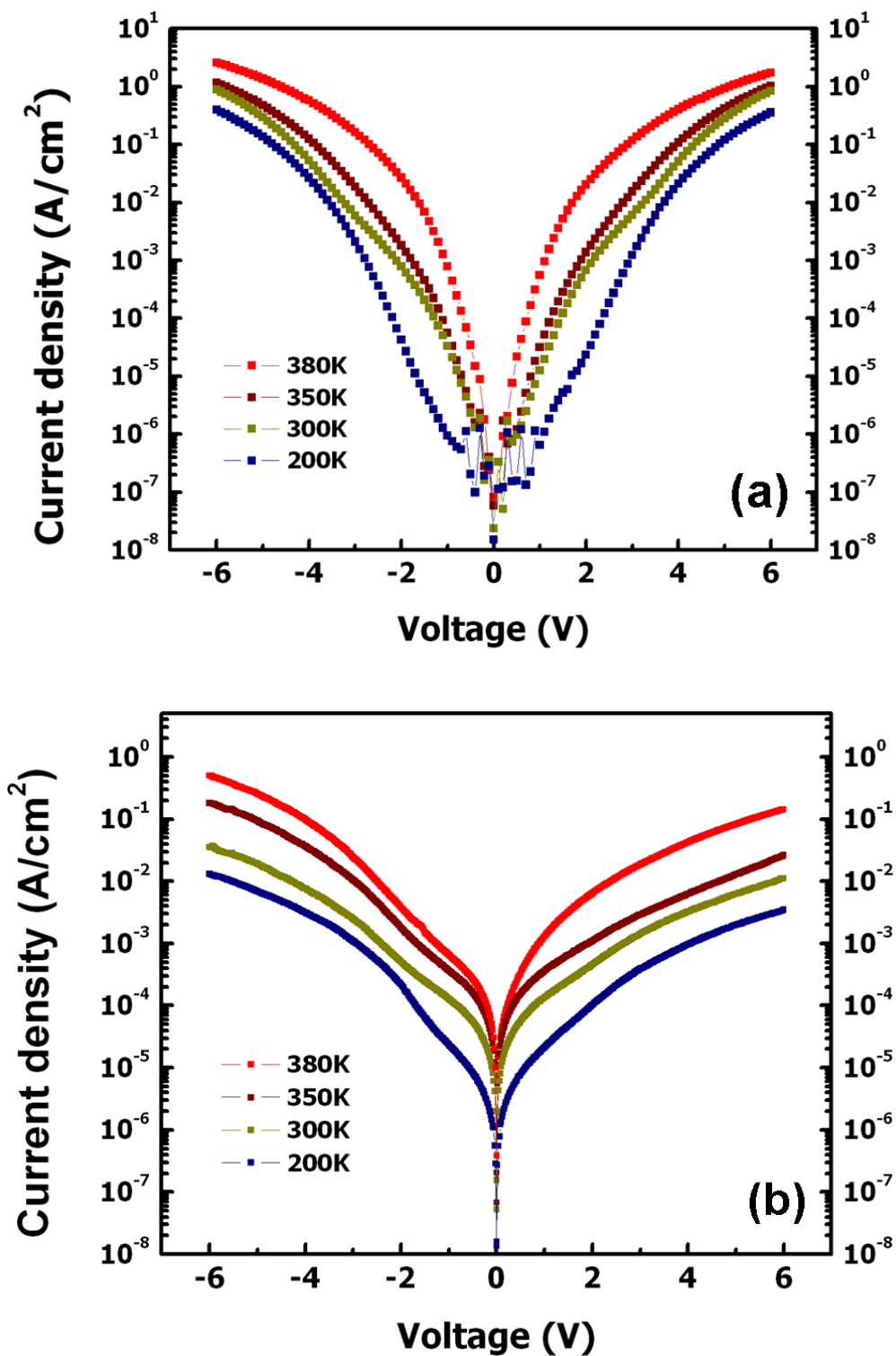
Figure 9.1 Current density as a function of applied voltage for KNN-LT-LS thin films, a) base and b) Mn-doped thin films

On the other hand, Poole-Frenkel emission is the dominant charge transport mechanism when the carriers are thermally emitted from trapped centers under a strong electric field: [1-3]

$$J_{PF} = B * E \exp\left[\dfrac{-q\left(\phi_t - \sqrt{\dfrac{qE}{\pi\varepsilon_i\varepsilon_o}}\right)}{k_BT}\right] \qquad (2)$$

where B is a constant and ϕ_t is the trapped level.

If the concentration of charge carriers is large on the surface such that it causes a band bending for the holes/electrons, then the interface may become an ohmic contact. If there are a large number of carriers within the film, then the leakage current at higher fields is limited by SCLC current with unique trap levels according to the following:[1-3]

$$J_{SCLC} = C\mu_p\varepsilon_i\dfrac{E^2}{d}\exp\left[\dfrac{-qW_t}{k_BT}\right] \qquad (3)$$

where C is a constant, d is the thickness, μ_p is the hole mobility and W_t is the trapping level.

In order to investigate the leakage mechanism in base KNN-LT-LS films, the current density is plotted against voltage in logarithmic scale and shown in Figures 9.2. The current-voltage data were also plotted as ln(J/E) (or ln (Ω), Ω: conductivity) vs. $\sqrt{E}$ for Poole-Frenkel emission, shown in Figure 9.3, and as ln(J) vs. $\sqrt{E}$ for Schottky emission, as shown in Figure 9.4 to differentiate between the two mechanisms. For base films, as shown in Figure 9.2, the slope of the log-log curves is ranging from 4.5 to 8, and is quite higher than 1 at any voltage region and therefore, it can be inferred that ohmic conduction is not responsible for the leakage current in such films. For the SCLC current

to be the dominant transport mechanism, the slope of such current-voltage plot (or current density-voltage) must be 2, according to the equation 3 above. Hence this mechanism is also not the governing transport mechanism. Slopes of the linear fit plots for different transport mechanisms are found and summarized in Table 10.1. To differentiate between Poole-Frenkel and Schottky emission, one way is to find the slope of the curves in Figure 9.3 and 9.4 based on Schottky and Poole-Frenkel emission [7-9] which would be:

$$\alpha = \frac{-q^{3/2}}{k_B T \sqrt{4\pi\varepsilon_0 \varepsilon_i}} \qquad \text{for Schottky emission}$$

$$\alpha = \frac{-q^{3/2}}{k_B T \sqrt{\pi\varepsilon_0 \varepsilon_i}} \qquad \text{for Poole-Frenkel emission}$$

Using the reported values on dielectric constant of $KNbO_3$ at microwave frequencies ($\lambda \sim 4000\text{Å}$) as reference, [10] it can be concluded that in base KNN-LT-LS thin films, Poole-Frenkel is the dominant leakage mechanism, as the dielectric constant values derived from the PF slope is close to the real values, which are reported as n~2.4 at microwave frequencies.

Figure 9.2 Analysis of leakage current of base KNN-LT-LS thin films for SCLC/ohmic mechanism. The slopes of linear fit plots are shown

Figure 9.3 Analysis of leakage current of base KNN-LT-LS thin films for Poole-Frenkel mechanism. The slopes of linear fit plots are shown

Figure 9.4 Analysis of leakage current of base KNN-LT-LS thin films for Schottky mechanism. The slopes of linear fit plots are shown
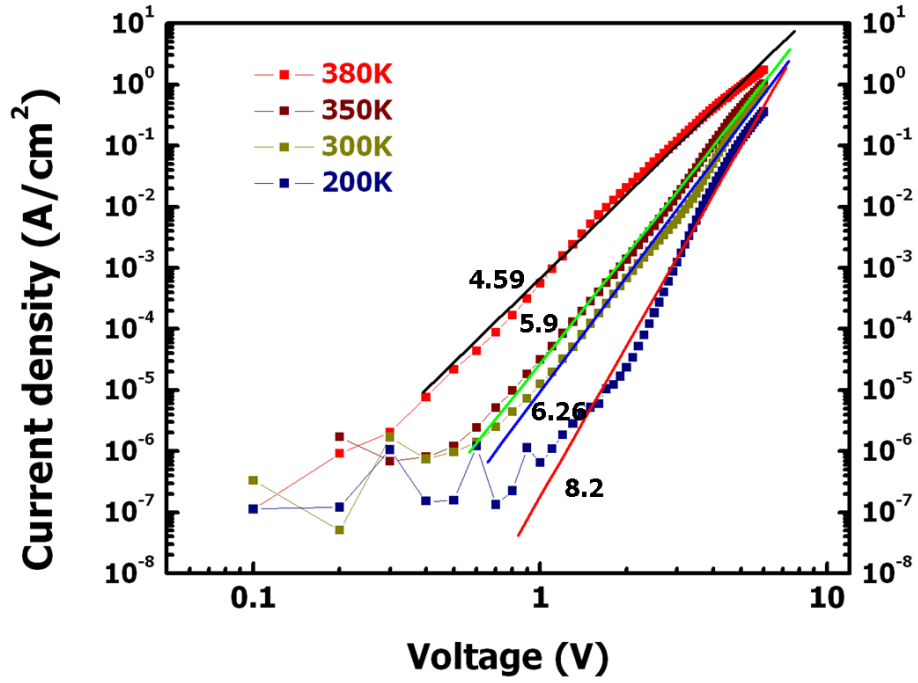

Figure 9.5 Analysis of leakage current of Mn-doped KNN-LT-LS thin films for SCLC/ohmic mechanism. The slopes of linear fit plots are shown
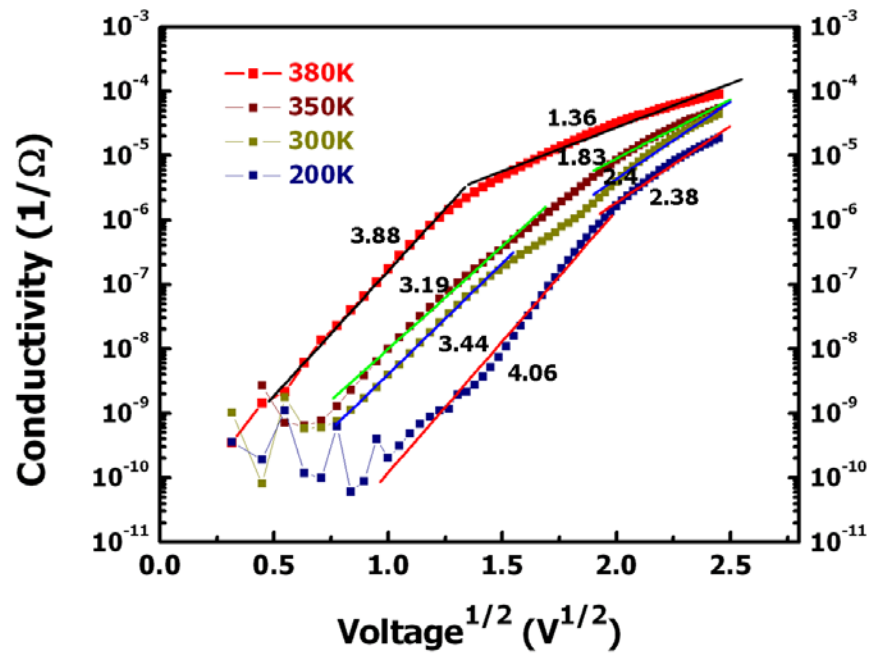
Figure 9.6 Analysis of leakage current of Mn-doped KNN-LT-LS thin films for Poole-Frenkel mechanism. The slopes of linear fit plots are shown.
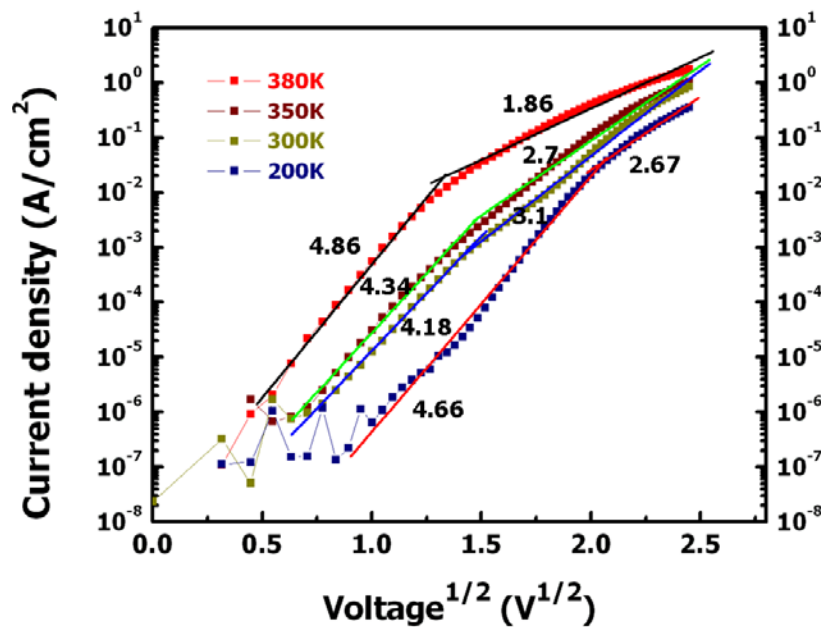

Figure 9.7 Analysis of leakage current of Mn-doped KNN-LT-LS thin films for Schottky mechanism. The slopes of linear fit plots are shown.
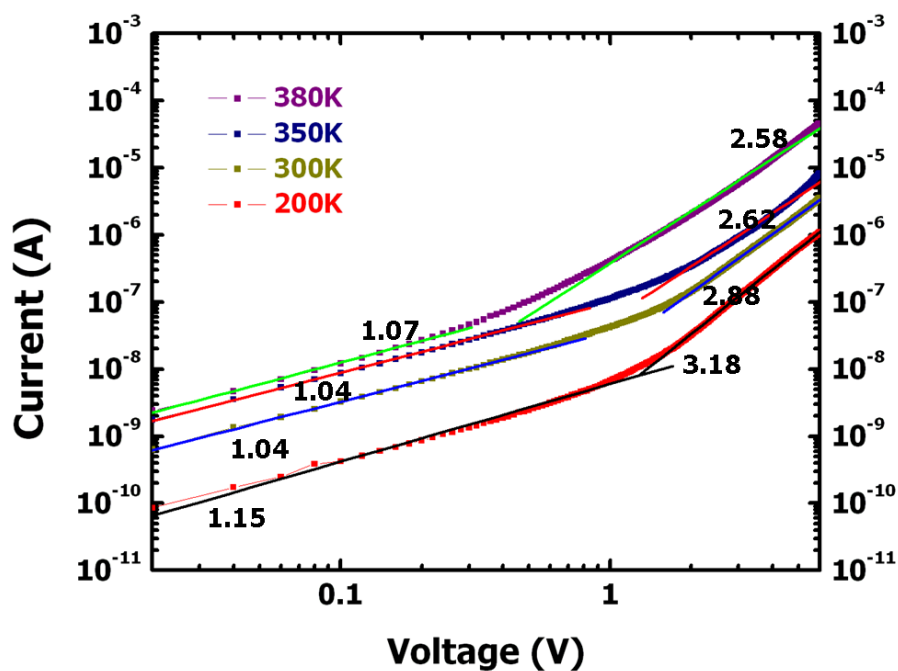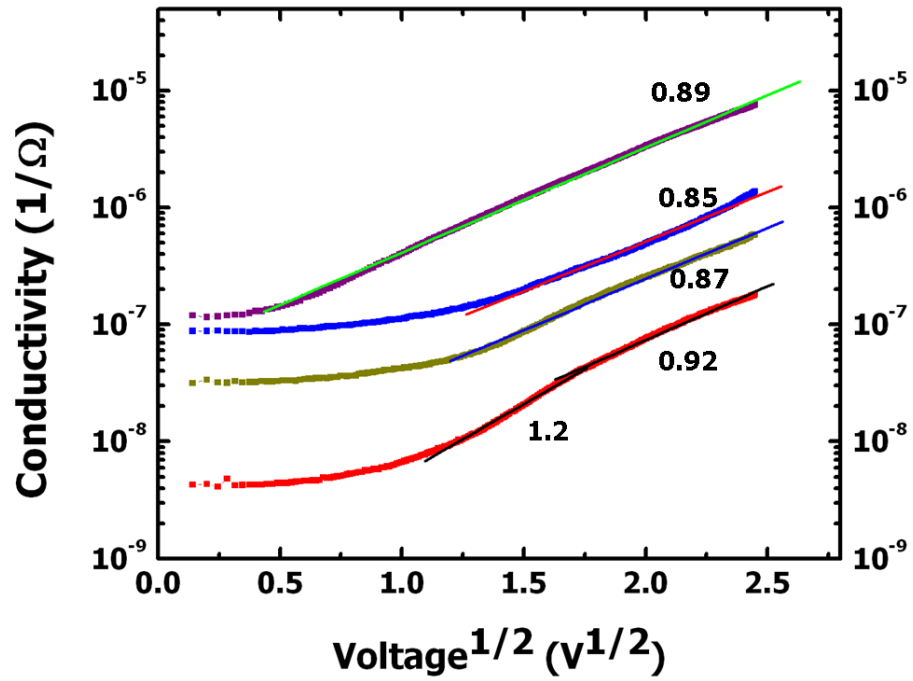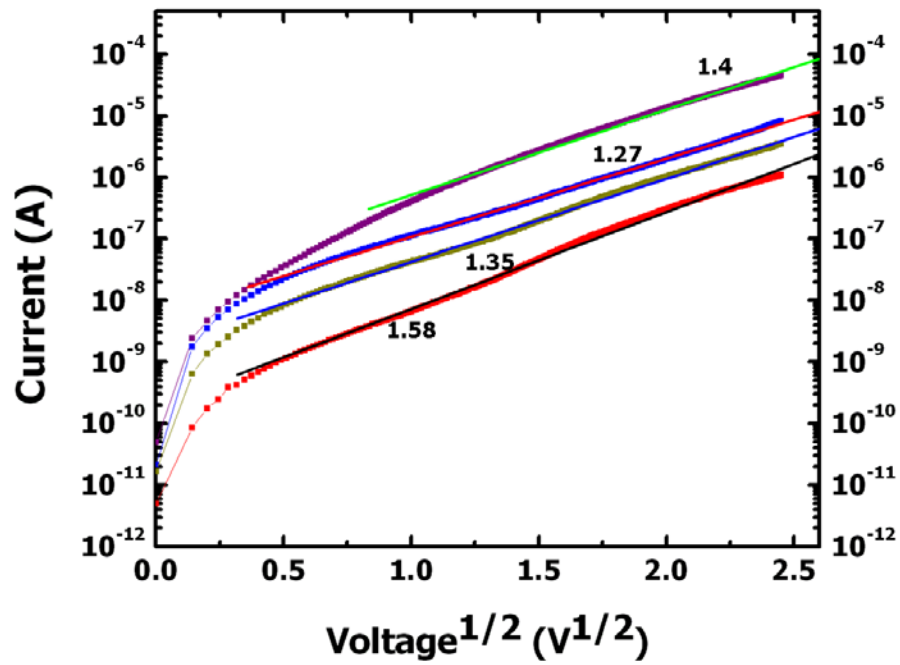
Similar analysis has been applied to Mn-doped thin films and results are shown in Figures 9.5 through 9.7. For Mn-doped films, from Figure 9.5, the slope of the log-log curves ($J \propto E^n$) at lower voltages is approximately 1 while it is ~ 3.2 for higher voltage. Also, these values stay the same for all measured temperatures, and the difference is in the onset of the slope change which decreases with increasing the temperature. At lower temperatures (200K), the slope changes abruptly from 1.15 almost to 3.3 at around 1 V (20kV/cm), while it appears to be ~ 0.5V (10kV/cm) at higher temperature (380K). This shows that the ohmic conduction is responsible for the leakage at lower voltages (<1 V, 20 kV/cm). However, the results show that SCLC current is not the governing mechanism in higher voltages. Leakage current in Mn-doped thin films shows a change in transport mechanism at higher voltages. From the table and using dielectric data from the literature, Schottky emission is most likely the governing mechanism in such thin films, since a closer dielectric constant to the reported value of ~2.4 at λ ~ 4000Å was achieved in fitting the I/V curve to Schottky equation. **[10]**

Table 9.1 Slope and derived dielectric constant for pure and Mn-doped KNN-LT-LS

Temperature	Pure			Mn-doped		
	SCLC	Schottky	P-F	SCLC	Schottky	P-F
	n	ε_i	ε_i	n	ε_i	ε_i
200	8.2	1.70712	5.4257	1.15	4.93358	45.6986
300	6.26	0.74613	1.78885	1.04	2.66458	22.7121
350	5.9	0.94285	1.73251	1.04	1.73251	17.4809
380	4.59	1.44822	3.09703	1.07	1.07299	13.5267

9.3 Phase transition in KNN-LT-LS thin Films

Temperature dependence of the capacitance is shown in Figure 9.8 for films with 450 and 1500 nm thicknesses. The capacitance of the films was measured from 200 μm electrodes with very fine gold wires (50μm diameter) bonded to the electrode using silver paint. The dielectric constant could not be precisely calculated from capacitance due to the uncertainty in the bonded area. However, the trend of capacitance with temperature is exactly the same as permittivity with temperature, thus allowing for taking maximum in capacitance as the same in permittivity.

In 450nm thin film, no maximum in capacitance corresponding to the ferroelectric phase transition has been observed up to 370 $^{\circ}$C, while in 1.5μm films, capacitance exhibits a diffuse transition at around 265°C. The existence of the ferroelectric phase transition in thicker films most likely indicates the strain and thickness dependence of dielectric constant and that the thinner films have not fully strain-relieved. Also, dielectric constant showed an exponential increase with temperature and there is a possibility that the phase transition would have occurred at a much higher temperature. As shown in previous section, increasing temperature significantly increases the leakage current, eventually resulting in dielectric break-down. Therefore, the measurement temperature was not exceeded 370 $^{\circ}$C to keep the dielectric loss and leakage current low enough for accurate capacitance measurements. It should be noted that presence of large amount of residual strain in 450 nm films which has greatly influenced the temperature of phase transition in these films, is rather unexpected, since for most oxide films, it is believed that the strain is mostly relaxed above a certain critical thickness, which is typically between 100 and 200 nm. **[17-19]** The effect of thickness on permittivity and

shift of the phase transition temperature requires further comprehensive study with a series of films of various thicknesses and possibly on different substrates to account for effect of tensile and compressive stresses, which was beyond the scope of this study.

In general, the phase transitions that normally occur in bulk ferroelectrics are reported to shift, broaden or disappear significantly in thin films. The shift, diffuseness or disappearance of phase transition is believed to be mainly caused by the residual strain in the films, as the transition peaks is reported to become sharper upon increasing the thickness. The increase of the transition temperature has been previously attributed to the presence of stress in the epitaxial thin films. **[11-15]** However the broadening and flattening of the peak is typical of diffuse transitions as observed in some polycrystalline BST and $BaTiO_3$ thin films, and fine grained $BaTiO_3$ ceramics. **[15]** This type of behavior is often attributed to structural inhomogeneity resulting from reduced grain size. The observations in this study may be explained by the presence of strain gradients in the epitaxial film as a result of the partial coherence of the film with the substrate. A network of dislocations is formed to partially relax the thin film. The average strain is two dimensional and nonzero, thereby causing an increase in the transition temperature. Concurrently, the inhomogeneity of the local strain results in the presence of both cubic and tetragonal microregions at a given temperature. This broadens the peak in the dielectric constant as a function of temperature. The local variation of the strain and structure leads to local changes in the permittivity. The behavior is reminiscent of the dielectric response of relaxor ferroelectrics, in which case compositional disorder is fundamental. However, for KNN-LT-LS system, compositional disorder is not present. In bulk KNN-LT-LS, the cubic-tetragonal phase transition is reported to occur between 260-

270 ^{o}C according to Hagh et al. **[16]** Also a polymorphic phase transition is observed at around 30 ^{o}C, between ferroelectric tetragonal and ferroelectric orthorhombic phases. **[16]**
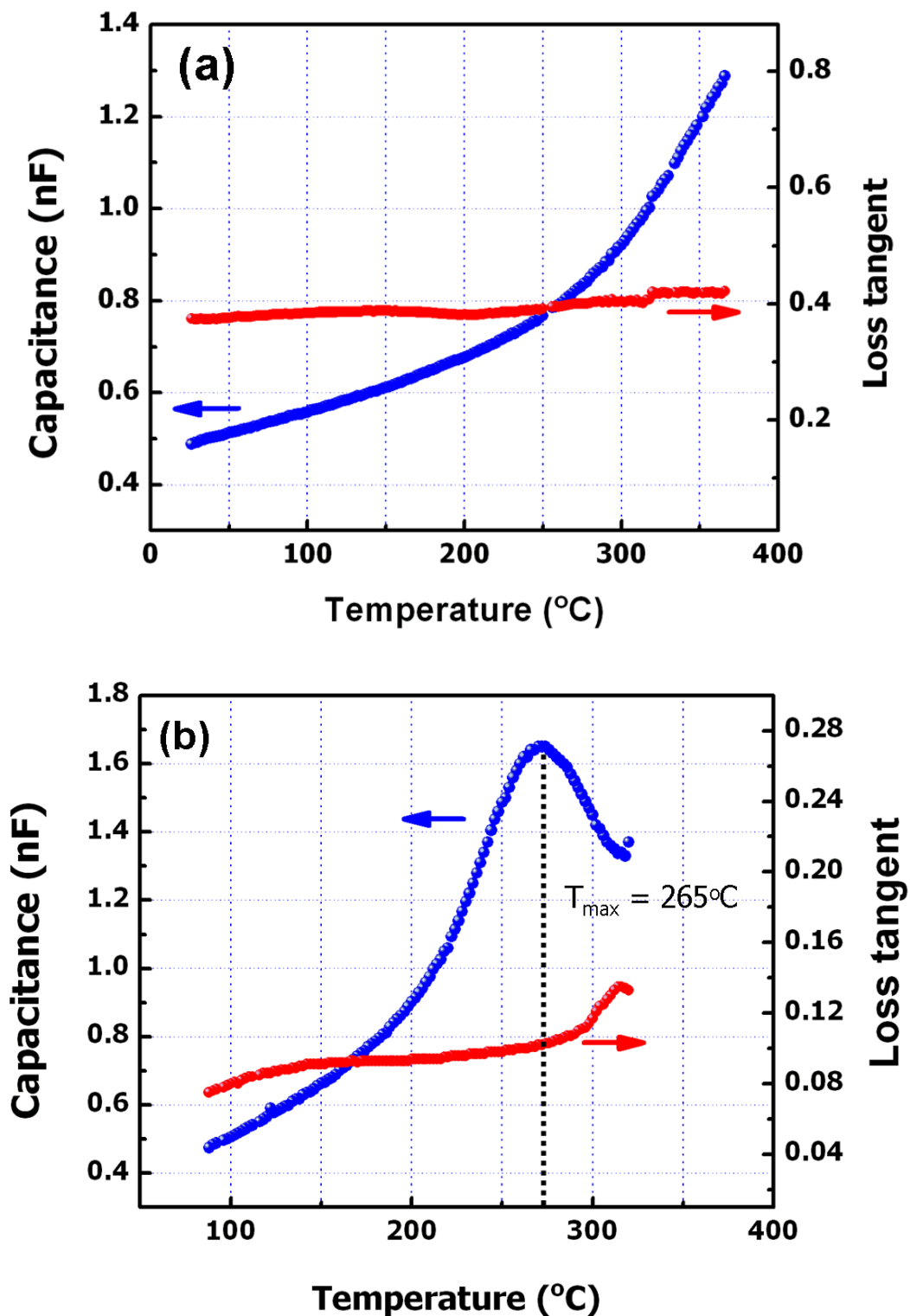
Figure 9.8 Temperature dependence of capacitance in a) 450nm and b)1.5 μm thick KNN-LT-LS thin films

9.4 Summary

In this chapter, leakage current behavior of KNN-LT-LS thin films with respect to the applied voltage was studied as a function of temperature. Additionally, temperature dependence of capacitance and phase transitional behavior of the films were investigated. It was revealed that the different transport mechanisms dominate in base and Mn-doped thin films. In base KNN-LT-LS thin films, Poole-Frenkel emission was found to be responsible for leakage, while Schottky was the dominant mechanism in Mn-doped thin films at higher electric fields.

Furthermore, measurement of the capacitance as a function of temperature in KNN-LT-LS thin films indicated that at submicron films, ferroelectric phase transition was suppressed while thicker films exhibited similar transition temperatures with a rather diffuse behavior as to that of bulk ceramic. This is primarily explained based on the presence of non-relieved strain and more compositional and structural inhomogeneities in the submicron thin films.

References

[1] M. Ohring, *The Materials Science of Thin Films*, Academic, New York, 1992.

[2] J. J. O'Dwyer, *The Theory of Electrical conduction and Break Down in solid Dielectrics*, Clarendon, Oxford, 1973

[3] J. F. Scott, *Ferroelectric Memories*, Springer-Verlag, Berlin Heidelberg (2000).

[4] K. H. Ahn, S. Baik, S. S. Kim, *J. Appl. Phys.* **92**, 2651 (2002).

[5] B. Nagaraj, S. Aggarwal, T. K. Song, R. Ramesh, *Phys. Rev. B* **59**, 16022 (1999).

[6] S. S. N. Bharadwaja, S. B. Krupanidhi, *Mater. Sci. Eng., B, Solid-state Mater. Adv. Technol.* **78**,1 (2000).

[7] H. N. Al-Shareef,, D. Dimos, *J. Am. Ceram. Soc.* **80**, 3127 (1997).

[8] Y. Shimada, Y. Inone, T. Nasu, K. Arita, Y. Nagano., A. Matsuda, Y. Uemoto, E. Fujii, M. Azuma, Y. Oishi, S. Hayashi, T. Otsuki, *Jpn. J. Appl. Phys.* **35**, 140 (1996).

[9] E. M. Alkoy, T. Shiosaki, *Thin Solid Films* **516**, 4002 (2008).

[10] Y. Uematsu, *Jpn. J. Appl. Phys.* **19**, No. 9, 1369 (1974).

[11] C. B. Parker, J. –P. Maria, A. I. Kingon, *Appl. Phys. Lett.*, **81**, 340 (2002).

[12] L. J. Sinnamon, R. M. Bowman, J. M. Gregg, *Appl. Phys. Lett.*, **81**,889 (2002).

[13] Z. Surowiak, D. Czekaj, A. A. Bakirov, E. V. Sviridov, V. P. Dudkevich, *Integrated Ferroelectrics*, **8,** 267, (1995).

[14] B. H. Hoerman, G. M. Ford, L. D. Kaufmann, B. W. Wessels, *Appl. Phys. Lett.* **73**, No.16, 2248 (1998).

[15] J. A. Bellotti, PhD thesis, Rutgers University, New Brunswick, NJ (2003).

[16] N. M. Hagh, PhD thesis, Rutgers University, New Brunswick, NJ (2006).

[17]W. K. Simon, E. K. Akdoğan, and A. Safari, *J. Appl. Phys.* **97**, 103530 (2005).

[18] J. W. Matthews and A. E. Blakeslee, *J. Cryst. Growth* **27**, 118 (1974).

[19] B. S. Kwak, A. Erbil, J. D. Budai, M. F. Chisholm, L. A. Boatner, and B.J. Wilkens,

Phys. Rev. B **49**, 14865 (1994).

10 Dielectric and Piezoelectric Properties of Lead-free BNT-based Thin Films

10.1   Introduction

Ferroelectric materials based on $(Bi,Na)TiO_3$, first reported by Smolenski et al. in 1961, is now considered as a potential alternative to conventional lead-based ferroelectrics offering moderate electromechanical properties.[1,2] On the other hand, solid solutions based on BNT system may be considered superior to KNN-based solid solutions with respect to the temperature stability of piezoelectric properties as well as ease of processing. As indicated in detail in chapter 2, pioneering work by Takenaka et al demonstrated high piezoelectric activity in the $(0.88)(Bi_{1/2}Na_{1/2})TiO_3$-$(0.08)(Bi_{1/2}K_{1/2})TiO_3$-$(0.04)BaTiO_3$ (BNT-BKT-BT) ternary system in the vicinity of the morphotropic phase boundary (MPB) with a high d_{33} of 181 pC/N and electromechanical coupling factor of 0.56.[3] With the revived interest in lead-free piezoelectric materials and new demand for such functional devices, development of BNT-based thin films with superior piezoelectric properties is essential to be pursued for future applications.

In this chapter, preliminary studied on growth, dielectric, ferroelectric and piezoelectric properties of MPB BNT-BKT-BT thin films epitaxially grown on $SrRuO_3$ coated $SrTiO_3$ substrate are demonstrated. The aim of this chapter is to investigate the baseline properties for BNT-BKT-BT single-phase films and to compare their piezoelectric performance with KNN-LT-LS thin films on similar substrates. BNT-BKT-BT thin films were deposited on $SrRuO_3$ (SRO) coated (001) $SrTiO_3$ (STO) substrates using dense stoichiometric $(0.88)(Bi_{1/2}Na_{1/2})TiO_3$-$(0.08)(Bi_{1/2}K_{1/2})TiO_3$-$(0.04)BaTiO_3$ targets.   The composition of interest is positioned at the MPB between ferroelectric

rhombohedral and tetragonal phases. The SRO film as the bottom electrode is only partially strain-relieved **[4,5]** and thus has a pseudocubic structure on STO substrate. The background oxygen pressure was kept at 300 mTorr during deposition for all the films and the deposition temperature is varied between 650-800°C to obtain highly crystalline single-phase thin films.

10.2   Structure and surface morphology

X-ray diffraction θ-2θ patterns of the BNT-BKT-BT films deposited at different temperatures ranging between 650 ^{o}C and 800 ^{o}C, are displayed in Figure 10.1(a). All films exhibited highly oriented (00l) perovskite phase with no second phase formation. The indices marked on the figure are based on pseudocubic and tetragonal structure for SRO and BNT-BKT-BT thin films, respectively. Formation of such a single preferred orientation is attributed to the proximity of the lattice constants of BNT-BKT-BT with STO substrate, e.g. a=3.9Å and c=3.94Å for film and a=3.905Å for STO substrate. A close look at (002) peaks of the films reveals that at low deposition temperature (650 ^{o}C), the films have less crystallinity as evidenced by the low intensity and broadness of the peak. It is observed that the peak sharpens and its intensity increases as the deposition temperature is raised. This is expected due to the slow diffusion kinetics of the arriving species at the substrate at lower temperatures during the growth process. Furthermore, the epitaxial growth in these films was confirmed using X-ray ϕ-scans performed on the <011> pole of the films deposited at 750 ^{o}C, as illustrated in Figure 10.1(c). Appearance of 4 peaks with 90° separation indicates a cube-on-cube epitaxial relationship between the

films and the STO substrate. Intensity of the ϕ scans of <011> pole of the films deposited at low temperatures was not high enough for a conclusive observation.

Figures 10.2 and 10.3 show the evolution of nanostructure of the BNT-BKT-BT thin films at different deposition temperatures. Surface morphology of the films is shown in Figure 10.2, while the cross section is displayed in Figure 10.3. From the FESEM micrographs, it is found that at low temperatures, the films have a columnar structure and the surface of the film is covered with [001] texture orientation. With increasing deposition temperature, grain size increases, surface of the film becomes smoother and the columnar morphology of the nanostructure gradually vanishes. At 700 and 750 ^{o}C, the films clearly show a platelet type growth and finally at 800 ^{o}C exhibit a uniform dense cross section as well as a smooth surface and sharp interface between the substrate and the film. Some porosity is observed on the surface in all films, which is greatly reduced in films deposited at 800 ^{o}C . In comparison to PZT thin films, epitaxial growth of BNT-BKT-BT films on $SrTiO_3$ substrates occur at a higher temperature, i.e. 575 ^{o}C-600 ^{o}C for PZT vs. 750 ^{o}C-800 ^{o}C for BNT-BKT-BT thin films.
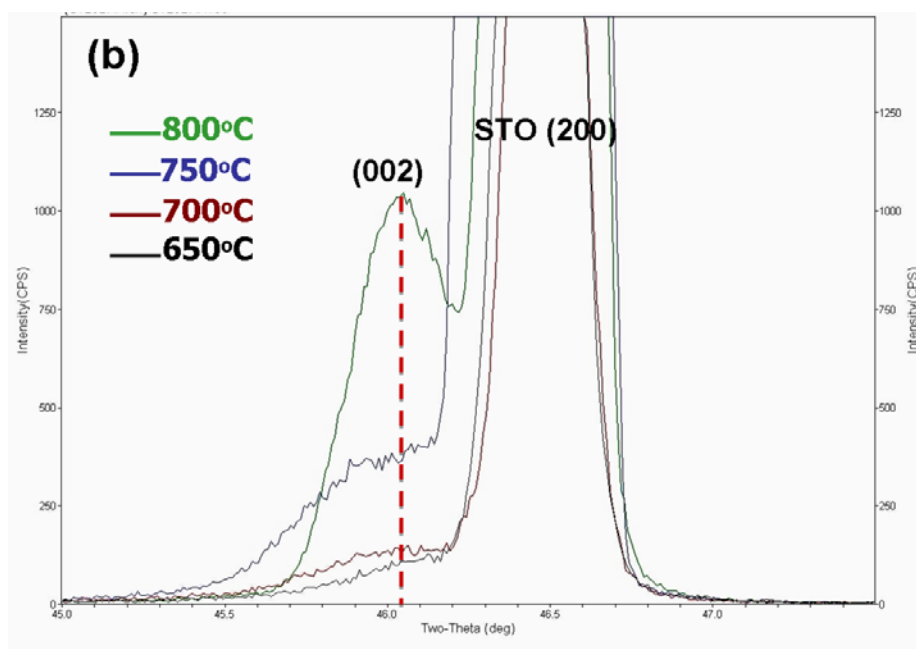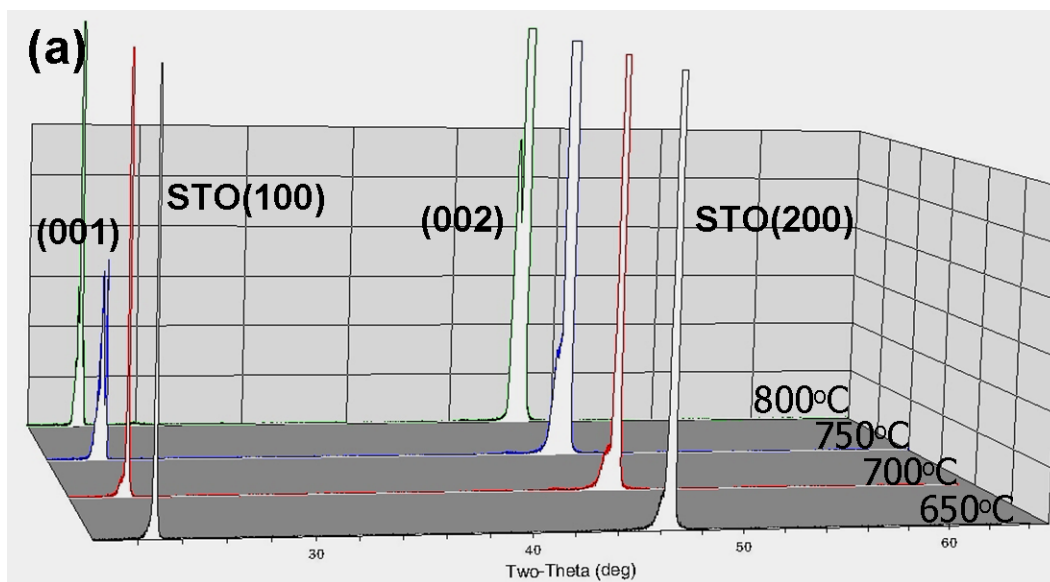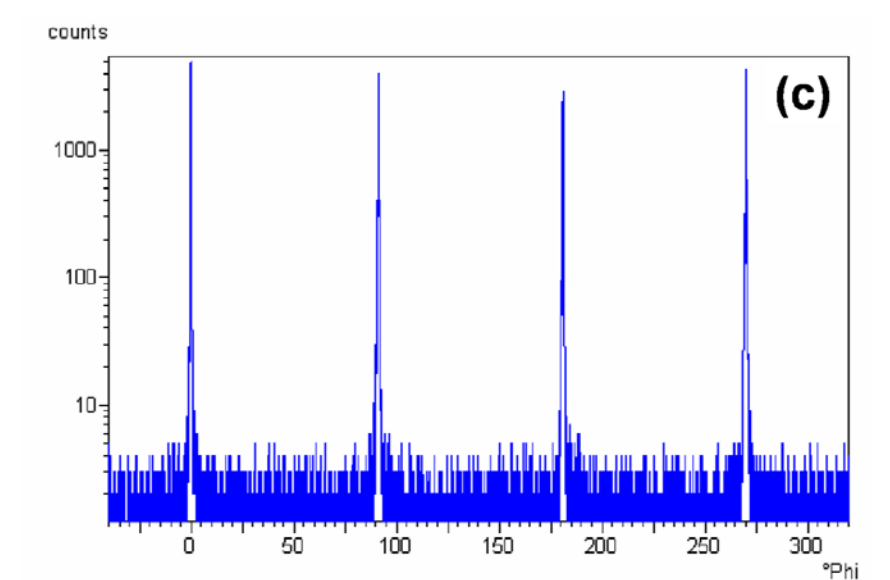
Figure 10.1 a) XRD θ-2θ patterns for BNT-BKT-BT thin films deposited at 600-750°C, b) (002) peak evolution and c) ϕ scan of <011>pole
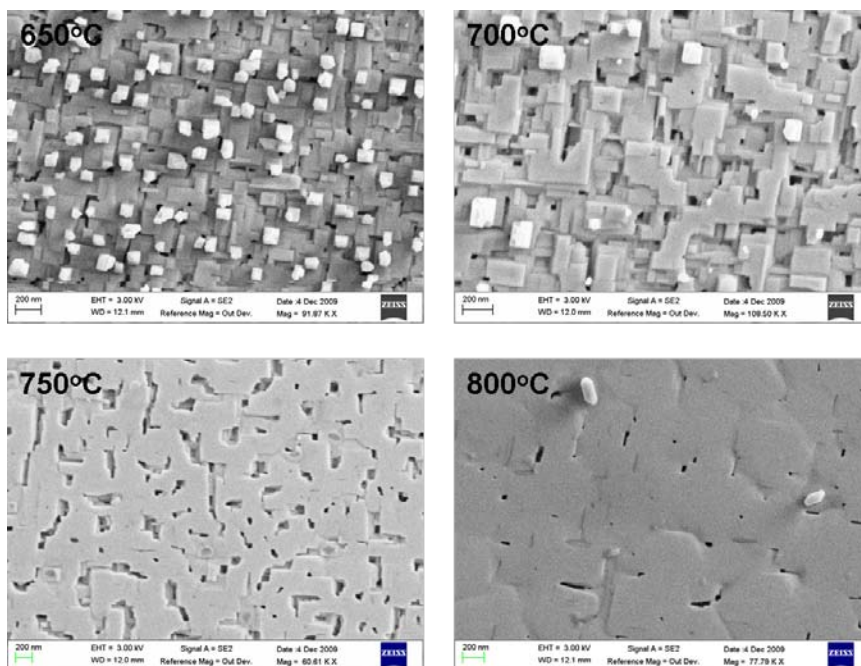
Figure 10.2 Surface morphology of BNT -BKT-BT thin films on SrTiO$_3$ substrate deposited at 600-750°C
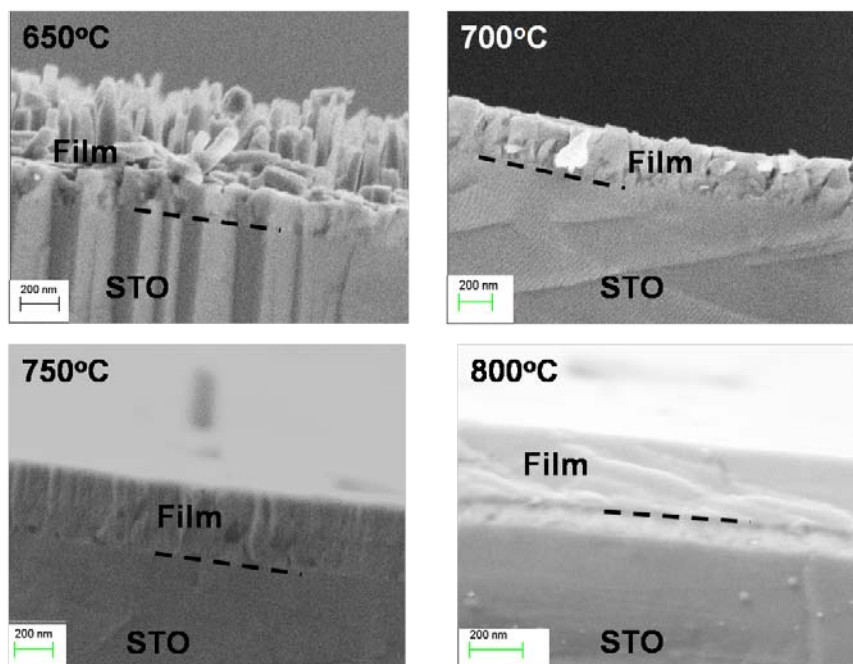

Figure 10.3 Cross section SEM images from BNT -BKT-BT thin films on SrTiO$_3$ substrate deposited at 600-750°C

10.3   Dielectric and ferroelectric properties of BNT-BKT-BT thin films

The dielectric and piezoelectric properties of BNT-BKT-BT films were evaluated in a metal-insulator-metal (MIM) configuration at room temperature. Figure 10.4(a) shows the frequency dependence of dielectric permittivity and loss in BNT-BKT-BT thin films. The dielectric permittivity decreased from 720 to 530 between 100 Hz and 100 kHz with a 30 mV_{rms} oscillation level. The associated dielectric losses were around 10-20% in this frequency range. A finite space charge contribution to the polarization is observed at low frequencies. The small increase in loss tangent above 100 kHz is associated with sample fixturing. Takenaka et al reported a value of 1000 for dielectric constant of BNT-BKT-BT MPB composition at 1 kHz. [6] The dielectric constant of 350 nm thin films at 1 kHz studied in this work is close to 75% of that of bulk ceramic. Figure 10.4 (b) demonstrates the small-signal (100 kHz) permittivity and loss dependence on dc bias field in the films. The C/V plots appear symmetric with a hysteresis behavior typical of ferroelectric capacitors. Dielectric constant exhibits a significant change with applied electric field. This indicates that ferroelectric domain structure, in addition to electronic and ionic polarizations, contributes significantly to the polarizability of the films. The maximum dielectric constant occurs at a field of 40 kV/cm in both directions. In addition, dielectric loss seems to be symmetric at lower electric fields while it tends to increase asymmetrically above 250 kV/cm at the positive field direction. This could partially be due to the asymmetric configuration of electrodes in the MIM structure.
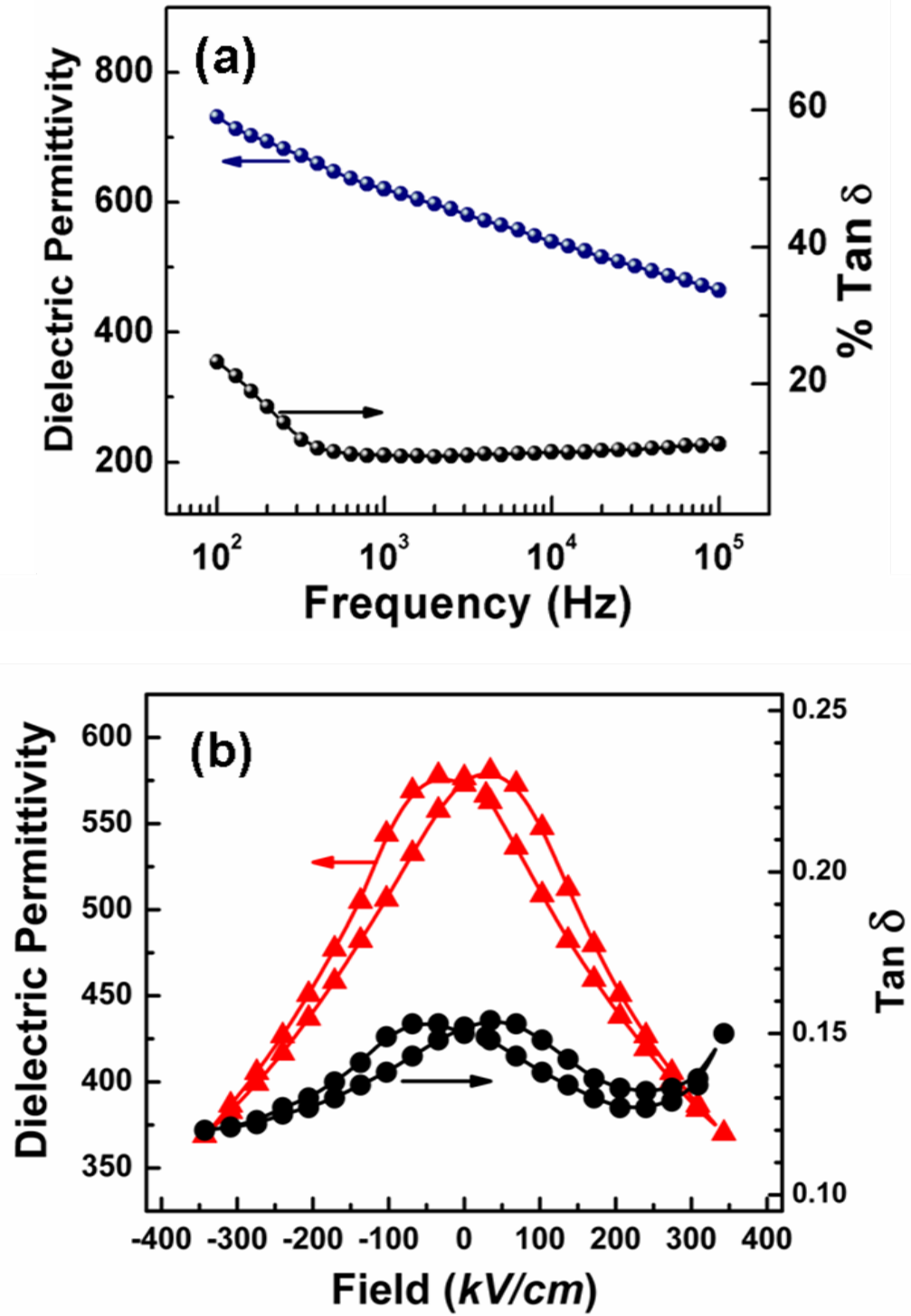
Figure 10.4 a) Frequency dispersion of dielectric constant and loss tangent, and b) Field dependence of the dielectric constant of 350nm BNT-BKT-BT thin films.

Polarization-electric field hysteresis loops (*P/E*) were measured with a triangle wave pulse (pulse width 1ms) as demonstrated in Figure 10.5. The loops were found to be well-saturated with a remanent polarization, P_r of 30 μC/cm^2. This polarization compares well with that of bulk *BNT-BKT-BT*, which was nearly 35 μC/cm^2 as reported by Takenaka et al. **[6]** The average coercive field, E_c in the films was approximately 95kV/cm with a small shift along the negative field direction. Built-in electric field due to defects and existence of a mechanical stress during epitaxial thin film growth conditions could create such small internal bias (-7 kV/cm) in the samples. The measured coercive fields in these films are rather larger compared to the average bulk values (50 kV/cm). This could be a consequence of a higher defect concentration, local internal fields, non-180° domain wall clamping, or film stresses. **[7,8]** These results are significantly superior to those previously reported on BNT-based or KNN-based thin films in the literature. **[9-12]**
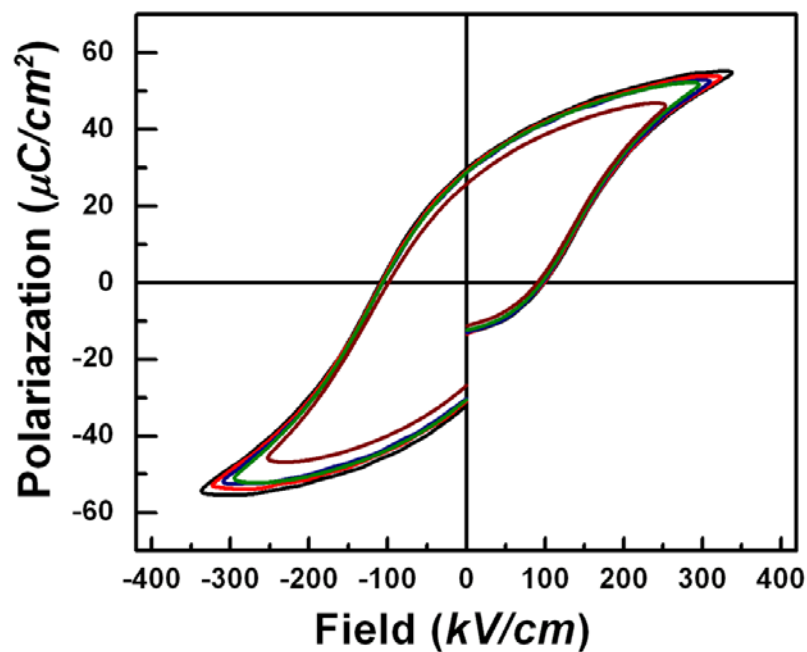
Figure 10.5 Polarization hysteresis loop of BNT-BKT-BT thin films.
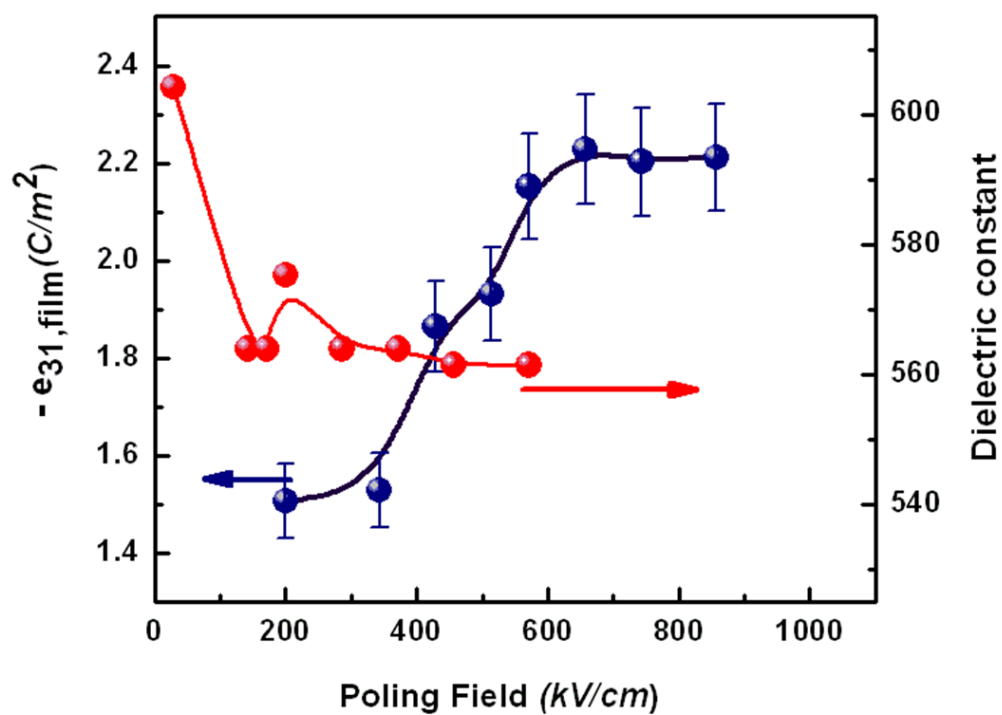

Figure 10.6 Effective transverse piezoelectric coefficient, $-e_{31,f}$, of BNT-BKT-BT thin films as a function of poling field.

10.4   Measurement of the transverse piezoelectric coefficient of BNT-BKT-

BT thin films

The transverse piezoelectric coefficient, $e_{31,f}$ and dielectric constant of BNT-BKT-BT thin films at 1 kHz as a function of poling field is shown in Figure 10.6. Prior to charge measurement, samples were poled for 5 minutes at room temperature. As shown, the $e_{31,f}$ values gradually increased and saturated around -2.25 C/cm^2 for poling field of 600 kV/cm. In PZT thin films, it was reported that a high field poling was required for submicron thin films for optimal piezoelectric response. [8,13,14] It was shown that transverse piezoelectric coefficient, d_{31}, was considerably influenced by the actuation voltage and was generally improved at higher poling field. Also, the threshold poling field above which an optimal piezoelectric response was achieved, was found to be thickness dependent. This was associated with less non-180° domains mobility in thinner films. On the other hand, dielectric constant of the films showed no significant change at field above 200 kV/cm, as shown in Figure 10.6. This indicates that increase in the $e_{31,f}$ value at fields much higher than the coercive field may not have been originated from non-180° domain switching, as a corresponding decrease in dielectric constant would have occurred otherwise. Therefore, more studies on the ferroelectric switching and behavior of BNT-BKT-BT thin films are required before a conclusion could be made. Nevertheless, these measurements showed that 350nm thin films could stand very high fields of 800 kV/cm without breaking down.

10.5   Summary

In this chapter, preliminary studied on growth and electrical properties of MPB lead-free 0.88BNT-0.08BKT-0.04BT composition were demonstrated by pulsed laser deposition. 350 nm thin films exhibited a dielectric constant and loss tangent of ~ 600 and 10% respectively, at 1 kHz. High remanent polarization of 30 μC/cm^2 was measured for 350nm thin films with a large coercive field of 95 kV/cm. Effective piezoelectric coefficient, $e_{31,f}$ of the films were measured and found to be approximately -2.25 C/cm^2. Presented results suggest that BNT-based lead-free thin films have a great potential for future environment-friendly piezoelectric devices.

References

[1] Y.-M. Chiang, G.W. Farrey, A.N. Soukhojak, *Appl. Phys. Lett.* **73**, 3683 (1998).

[2] G.A. Smolenski, V.A. Isupov, A.I. Agranovskaya, N.N. Krainik, *Sov. Phys. Solid State* **2**, 2651(1961).

[3] T. Takenaka, H. Nagata, Y. Hiruma, *Jpn. J. Appl. Phys. 47, 3787* (2008).

[4] W. K. Simon, E. K. Akdoǧan, and A. Safari, *J. Appl. Phys.* **97**, 103530 (2005).

[5] J. W. Matthews and A. E. Blakeslee, *J. Cryst. Growth* **27**, 118 (1974).

[6] T. Takenaka, H. Nagata, Y. Hiruma, *IEEE trans. Ultrason. Ferro. Freq. Contr.* **56**, 1595 (2009).

[7] F. Xu, F. Chu, and S. Trolier-McKinstry, *J. Appl. Phys.* **86**, 588 (1999).

[8] S. Trolier-McKinstry, J. F. Shepard, Jr., T. Su, G. Zavala, and J. Fendler, *Ferroelectrics* **206**, 381 (1997).

[9] X.-G. Tang, J.Wang, X.-X.Wang, H.L.-W. Chan, *Chem. Mater.* **16**, 5293 (2004).

[10] H.-W. Cheng, X.-J. Zhang, S.-T. Zhang, Y. Feng, Y.-F. Chen, Z.-G. Liu, G.-X. Cheng, *Appl. Phys. Lett.* **85**, 2319 (2004).

[11] M. Abazari, E. K. Akdogan, A. Safari, *J. Appl. Phys.* **105**, 094101 (2008).

[12] J.-R. Duclre, C. Cibert, A. Boulle, V. Dorcet, P. Marchet, C. Champeaux, A. Catherinot, S. Dputier, M. Guilloux-Viry, *Thin Sol. Films* **517**, 592 (2008).

[13] N. Lederman, P. Muralt, J. Baborowski, S. Gentil, K. Mukati, M. Cantoni, A. Seifert, N. Setter, *Sensors and Actuators A* **105**, 162 (2003).

[14] M. Deshpande, L. Saggere, *Sensors and Actuators A* **135**, 690 (2007).

11 Conclusions

It was essential to study and understand the critical processing conditions that leads to the formation of single phase epitaxial thin film of these two major lead-free compositions, $(K_{0.44}Na_{0.52}Li_{0.04})(Nb_{0.84}Ta_{0.1}Sb_{0.06})O_3$ (KNN-LT-LS) and $0.88(Bi_{0.5}Na_{0.5})TiO_3-0.08(Bi_{0.5}K_{0.5})TiO_3-0.04BaTiO_3$ (BNT-BKT-BT) and to improve the quality and electrical properties of such films. The work described in this thesis involved a detailed study regarding the growth of such thin films of the said lead-free compositions, KNN-LT-LS and BNT-BKT-BT, by pulsed laser deposition and investigation of their dielectric and piezoelectric properties for applications in MEMS devices. The results of the study presented in this thesis can be briefly summarized as follows:

1. Highly epitaxial, <001> oriented and stoichiometric KNN-LT-LS thin films were deposited at 750 ^{o}C and 400 mTorr of oxygen partial pressure on $SrTiO_3$ substrates, while the laser energy density and repetition rate were kept at 1.2 J/cm^2 and 2 Hz. The nanostructure of the films exhibited to be highly dependent on the substrate temperature. It was revealed that the films were grown epitaxially at higher temperature, while at lower temperatures, films showed a columnar microstructure with a preferred orientation along c-axis. The composition of films deposited at higher oxygen pressures, was closer to stoichiometry with a higher A-site/B-site cation ratio. The dielectric constant as well as polarization were also enhanced in the films deposited at higher oxygen pressure. Thin films deposited at 750 ^{o}C and 400mTorr oxygen partial pressure exhibited a dielectric constant of ~750 at 1 kHz and remanent polarization of 7.5 μC/cm^2.

2. Addition of 1 mol% Mn to the KNN-LT-LS ceramic PLD target resulted in over two orders of magnitude suppression of leakage current in the thin films and an enhancement in saturation of polarization thereby. Mn-doped KNN-LT-LS thin films showed a 100% improvement in the remanent polarization of 16 $\mu C/cm^2$ as compared to pure KNN-LT-LS thin films. This showed that 75% of bulk polarization was retained in 500 nm thin films.

3. Domain structure of epitaxial lead-free KNN-LT-LS thin films showed a tetragonal structure with predominantly c-axis oriented domains and a small population of 90° domains. The effective longitudinal as well as transverse piezoelectric coefficients (d_{33} and $e_{31,f}$) of the KNN-LT-LS thin films with d_{33} of ~ 60 and 50 pm/V for 500 nm pure and Mn-doped films, respectively. Also, a $e_{31,f}$ of ~-4.5 C/cm^2 was found for base KNN-LT-LS thin films, which is among the highest values reported for lead-free piezoelectric thin films.

4. It was revealed that different transport mechanisms dominate in base and Mn-doped thin films. In base KNN-LT-LS thin films, Poole-Frenkel emission was responsible for leakage current, while Schottky was the dominant mechanism in Mn-doped thin films at higher electric fields. This was done through investigation of leakage current as a function of applied voltage at various temperatures.

5. Temperature dependence of capacitance and phase transition of the films indicated that at submicron films ferroelectric phase transition was suppressed while thicker films exhibited similar transition temperatures as to that of bulk ceramic. This was primarily explained based on the presence of non-relieved strain and more structural inhomogeneities in the submicron thin films.

6. An attempt was made to demonstrate preliminary results on growth and important electrical properties of thin films of Morphotropic Phase Boundary lead-free 0.88BNT-0.08BKT-0.04BT composition by pulsed laser deposition. The optimum conditions for the deposition of highly epitaxial and stoichiometric BNT-BKT-BT thin films were found to be 800 ^{o}C and 300 mTorr oxygen pressure. 350 nm thin films exhibited a dielectric constant and loss tangent of ~ 600 and 10% respectively, at 1 kHz. A remarkably high remanent polarization of 30 $\mu C/cm^2$ was measured for such films with a large coercive field of 95 kV/cm. Effective piezoelectric coefficient, e_{31f} of the films were measured and found to be approximately -2.25 C/cm^2.

On the basis of the obtained results in this thesis, it can be concluded that lead-free piezoelectric thin films based on KNN-LT-LS and BNT-BKT-BT compositions with comparable performance to some of their lead-based counterparts, such as hard PZT, have a potential for future environment-friendly piezoelectric devices and the study presented herein provides a foundation for further research to improve the reliability of production and stability of electrical properties in such thin films.

12 Suggestions for future work

Research on lead-free piezoelectric thin films has been the center of attention only recently and many years of work are required before it will be possible to realize high quality thin films for commercial devices. More studies need to be carried out to obtain a better understanding of the complex interplay between the processing conditions and the ferroelectric and piezoelectric performance of such thin films. In this chapter, few suggestions are made to carry out further research on lead-free KNN-based and BNT-based piezoelectric thin film, as a continuation of the presented work in this thesis:

1. A systematic study on addition of excess K and Na source in the PLD target in order to suppress the evaporation of these species during deposition. Addition of excess K and Na, especially may lead to a more stoichiometric thin films with a lower leakage current and improved polarization saturation. Similar study has been performed on PZT thin films, where addition of excess 20% PbO source to the PLD target effectively improved the chemical composition and electrical properties of the films.

2. Integration with silicon as an attempt to explore the challenges facing the deposition of these compositions on commercial $Pt/SiO_2/Si$ wafers. The study of optimum deposition condition has to be performed in a systematic fashion and may require additional steps such as annealing to obtain high quality thin films.

3. Use of a buffer layer, such as $NaNbO_3$, to enhance the crystalline quality and remanent polarization. Such buffer layers provide the possibility of highly oriented and epitaxial thin films on platinized substrates. This could be a major step forward in realization of lead-free MEMS devices.

4. Investigation of deposition on miscut substrates. Deposition of multiferroic materials, such as $BiFeO_3$ on miscut $SrTiO_3$ substrates has shown a significant enhancement of polarization and suppression of leakage current by domain and strain engineering.

5. A study of thickness-dependent material properties of thin films and its effect on ferroelectric-paraelectric phase transition behavior to determine if there is a critical temperature below which the transition is suppressed and how that influences the stability of piezoelectric properties.

6. Exploring the chemical composition as a function of thickness may also lead to some valuable information regarding how the growth process is affected in such thin films and how strain in thinner films influence the composition.

7. Examination and improvement of stability of polarization with respect to temperature to provide a suitable operating temperature range for various device applications. This could be carried out using dopants to shift the present transition temperatures.

8. Investigation of fatigue characteristics in these lead-free thin film as a key issue in their real-life applications

9. Optimization of annealing time, temperature and duration to enhance the crystallinity, stoichiometry and strain relief in the films

CURRICULUM VITAE

Maryam Abazari-Torghabeh

EDUCATION

2005-2010   **Ph.D.;** Materials Science and Engineering, **Rutgers-The State University of New Jersey, Piscataway, NJ**

2005-2007   **M.Sc.;** Materials Science and Engineering, **Rutgers-The State University of New Jersey, Piscataway, NJ**

2004-2005   **M.Sc.** Electrical Engineering, **Amirkabir University of Technology, Tehran, Iran** (passed course requirement)

200-2004   **B.Sc.** Electrical Engineering, **Sharif University of Technology, Tehran, Iran**

RESEARCH EXPERIENCE

- Development of $(K,Na)NbO_3$-$LiTaO_3$-$LiSbO_3$ ferroelectric thin films on Pt-coated Si and $SrTiO_3$ substrate by Pulsed Laser Deposition.

- Characterization of thin films of $(K,Na)NbO_3$-$LiTaO_3$-$LiSbO_3$ thin films by High resolution X-ray diffraction , field emission scanning electron microscopy (FESEM)

- Characterization of $(K,Na)NbO_3$-$LiTaO_3$-$LiSbO_3$ thin films by Rutherford Backscattering Spectroscopy

- Characterization of $(K,Na)NbO_3$-$LiTaO_3$-$LiSbO_3$ thin films by piezoelectric force microscopy (PFM)

- Explored the effect of deposition parameters in the crystalline quality and electrical properties of the $(K,Na)NbO_3$-$LiTaO_3$-$LiSbO_3$ thin films by Pulsed Laser Deposition

- Characterization of $(K,Na)NbO_3$-$LiTaO_3$-$LiSbO_3$ thin films by Scanning Electron Microscopy

- Supervised the development and characterization of magnetostrictive/ferroelectric $LaSrMnO_3$/$BatiO_3$/$SrRuO_3$/$SrTiO_3$ heterostructure by PLD

- Development of $Bi(Na,K)TiO_3$-$BaTiO_3$ ferroelectric thin films on $SrTiO_3$ substrates

- Development of BNKT-BT piezoelectric bi-layer composite

- Development of several LabView programs for automatic high and low temperature dielectric measurements

PUBLICATIONS

1. **M. Abazari**, A. Safari, "Dielectric and ferroelectric properties of lead-free BNT-based thin films" accepted to APL (2010)

2. A. Safari, **M. Abazari**, "Lead-free piezoelectric ceramics and thin films", IEEE trans. on Ultrasonics Ferroelectrics and Frequency Control , in press (2010)

3. **M. Abazari**, A. Safari, "Nanoscale characterization and local piezoelectric properties of lead-free KNN-LT-LS thin films", J. Phys. D: Appl. Phys. **43**, 025405 (2010).

4. **M. Abazari**, A. Safari,"Effect of doping on ferroelectric properties and leakage current behavior of KNN-LT-LS thin films on SrTiO3 substrates", J. Appl. Phys. **105** 094101 (2009)

5. A. Safari, **M. Abazari**, K. Kerman, E. K. Akdogan, "KNN-LT-LS ceramics and thin films", IEEE trans. on Ultrasonics Ferroelectrics and Frequency Control , Volume 56, Issue 8, pp 1586-1594 (2009)

6. **M. Abazari** , E. Akdogan, A. Safari, "Effects of background oxygen pressure on dielectric and ferroelectric properties of epitaxial $(K_{0.44}, Na_{0.52}, Li_{0.04})(Nb_{0.84}, Ta_{0.10}, Sb_{0.06})O_3$ thin films on $SrTiO_3$", Appl. Phys. Lett. **93**, 192910 (2008)

7. **M. Abazari** , E. Akdogan, A. Safari, "Effect of manganese doping on remnant polarization and leakage current in $(K_{0.44}, Na_{0.52}, Li_{0.04})(Nb_{0.84}, Ta_{0.10}, Sb_{0.06})O3$ epitaxial thin films on $SrTiO_3$", Appl. Phys. Lett. **92**, 212903 (2008)

8. **M. Abazari** , E. Akdogan, A. Safari, "Dielectric and ferroelectric properties of strain-relieved epitaxial lead-free KNN-LT-LS ferroelectric thin films on $SrTiO_3$ substrates", J. Appl. Phys. **103**, 104106 (2008)

9. E. Akdogan , K. Kerman , **M. Abazari**, A. Safari, "Origin of high piezoelectric activity in ferroelectric $(K_{0.44}Na_{0.52}Li_{0.04})(Nb_{0.84}Ta_{0.1}Sb_{0.06})O_3$ ceramics", Appl. Phys. Lett. **92**, 112908 (2008)